

Pattern Formation in Self-Organised Nanoparticle Assemblies

Christopher Paul Martin, MSci (hons)

Thesis submitted to the University of Nottingham
for the degree of Doctor of Philosophy

July 2007

Contents

Abstract	iv
List of publications	v
Acknowledgements	vi
1 Introduction	1
1.1 Background	1
1.2 Thesis outline	14
2 Non-Equilibrium Pattern Formation	16
2.1 Common morphologies	17
2.1.1 Cellular networks	17
2.1.2 Spots, stripes, and labyrinths	21
2.2 Dewetting of thin films	25
2.2.1 The interface potential	26
2.2.2 Dewetting modes	28
2.2.3 Distinguishing between dewetting modes	30
2.3 Patterns in nanoparticle arrays	31
2.3.1 A brief history of nanoparticle superlattices	32
2.3.2 Far from equilibrium pattern formation	36
2.4 Conclusions	42
3 Simulations and Experiments	43
3.1 Monte Carlo simulation	44
3.1.1 Background	44
3.1.2 The Monte Carlo method	45
3.1.3 The Ising model	47
3.1.4 The Metropolis algorithm	48
3.2 Nanoparticle simulations	50
3.2.1 The Rabani et al. model	50
3.2.2 Anisotropy modification	53

3.2.3	The four-phase checkerboard	55
3.2.4	Example morphologies	56
3.2.5	The simulation code	57
3.3	Atomic force microscopy	59
3.3.1	Basic principles	59
3.3.2	Lithographic AFM oxidation	63
3.4	Real-time observation of evaporation	64
3.5	Contact angle measurements	65
3.6	Summary	66
4	Nanoparticle Networks: Self-organised or Disorganised?	67
4.1	Pattern analysis and comparison	68
4.1.1	The fast Fourier transform	68
4.1.2	The Voronoi tessellation	69
4.1.3	Minkowski Morphometry	72
4.2	Analysis of experiments and simulations	76
4.2.1	Dewetted organometallic clusters	76
4.2.2	Simulated structures	80
4.3	Discussion and conclusions	84
5	Organising Nanoparticles by Directed Dewetting	86
5.1	Real-time observation during spin-casting	87
5.2	Modifications to the simulations	89
5.2.1	Background	89
5.2.2	A dynamic chemical potential	91
5.2.3	Exploring the dynamic chemical potential	94
5.2.4	Heterogeneous surfaces	102
5.3	The fingering instability	109
5.4	Conclusions	113
6	Scaling and Evolution of Nanoparticle Structures	114
6.1	Coarsening	115
6.1.1	Mechanically-induced coarsening	116
6.1.2	Rabani et al. simulations	116
6.2	Genetic algorithms	125
6.3	Conclusions	129
7	Conclusions	130
7.1	Summary of findings	130
7.2	Further work	132
	Bibliography	134

List of figures

151

Abstract

An extremely wide variety of self-organised nanostructured patterns can be produced by spin-casting solutions of colloidal nanoparticles onto solid substrates. This is an experimental regime that is extremely far from thermodynamic equilibrium, due to the rapidity with which the solvent evaporates. It is the dynamics of flow and evaporation that lead to the formation of the complex structures that are observed by atomic force microscopy (AFM). The mechanisms involved in the formation of these patterns are not yet fully understood, largely because it is somewhat challenging to directly observe the evaporation dynamics during spin-casting.

Monte Carlo simulations based on a modified version of the model of Rabani et al. [1] have allowed the study of the processes that lead to the production of particular nanoparticle morphologies. Morphological image analysis (MIA) techniques are applied to compare simulated and experimental structures, revealing a high degree of correspondence. Furthermore, these tools provide an insight into the level of order in these systems, and improve understanding of how a pattern's specific morphology arises from its formation mechanisms.

Modifying the properties of a substrate on the scale of a few hundred nanometres by AFM lithography has a profound effect on the processes of nanoparticle pattern formation. The simulation model of Rabani et al. was successfully modified to account for the effect of surface modification. The simulations were further modified to reproduce cellular structures on two distinct length scales— a phenomenon that is commonly seen in experiments.

The dynamic behaviour of simulated nanoparticle structures is examined in the “scaling” regime in relation to recent experiments carried out by Blunt et al. [2] in an attempt to understand the coarsening mechanism. Finally, a genetic algorithm approach is applied to evolve the simulations to a target morphology. In this way, an experimental target image can be automatically analysed with MIA techniques and compared with an evolving population of simulations until a target “fitness” is reached.

List of publications

- F. Frehill, K. H. G. Schulte, C. P. Martin, L. Wang, S. Patel, J. A. Purton, J. G. Vos, and P. Moriarty, **Iron Wheels on Silicon: Wetting Behavior and Electronic Structure of Adsorbed Organostannoxane Clusters.** *Langmuir* 20:6421-6429, 2004.
- Christopher P. Martin, Matthew O. Blunt, and Philip Moriarty, **Nanoparticle Networks on Silicon: Self-Organized or Disorganized?** *Nano Letters* 4:2389-2392, 2004.
- M. O. Blunt, C. P. Martin, M. Ahola-Tuomi, E. Pauliac-Vaujour, P. Sharp, P. Nativo, M. Brust, and P. J. Moriarty, **Coerced mechanical coarsening of nanoparticle assemblies.** *Nature Nanotechnology* 2:167-170, 2007.
- R. A. J. Woolley, C. P. Martin, G. Miller, V. R. Dhanak, and P. J. Moriarty, **Adsorbed molecular shuttlecocks: An NIXSW study of Sn phthalocyanine on Ag(111) using Auger electron detection.** *Surface Science* 601:1231-1238, 2007.
- Matthew O. Blunt, Milovan Šuvakov, Fabio Pulizzi, Christopher P. Martin, Emmanuelle Pauliac-Vaujour, Andrew Stannard, Andrew W. Rushforth, Bosiljka Tadić, and Philip Moriarty, **Charge Transport in Cellular Nanoparticle Networks: Meandering through Nanoscale Mazes.** *Nano Letters* 7:855-860, 2007.
- Peter Siepmann, Christopher P. Martin, Ioan Vancea, Philip Moriarty, and Natalio Krasnogor, **A Genetic Algorithm Approach to Probing the Evolution of Self-Organised Nanostructured Systems.** *Nano Letters* 7:1985-1990, 2007.
- Christopher P. Martin, Matthew O. Blunt, Emmanuelle Pauliac-Vaujour, Ioan Vancea, Uwe Thiele, and Philip Moriarty, **Controlling Pattern Formation in Nanoparticle Assemblies via Directed Solvent Dewetting.** *Physical Review Letters* 99:116103, 2007.

Acknowledgements

There are many people that deserve my thanks, first but not least Phil, for your relentless and excessively far-sighted enthusiasm, without which I would have struggled to remain focused. Uwe, for our many theoretical discussions, which have contributed significantly to this work. Matt, for a level of patience and perseverance in the laboratory that is well beyond my own ability, and without which this thesis would be significantly lacking in experimental results. Manu, for the countless hours you have spent in the clean room or at the AFM for my benefit, and for your company on many long conference days. James, for the motivational coffee mornings (and the de-motivational whisky evenings). I also give special thanks to all members of the Nanoscience group, past and present, who have put up with my jibber-jabber, and my apparently infectious ability to procrastinate. Finally, thank you Laura for your loving support, and for putting up with my grumpy moods, my periodic lethargy, and my frequently unsociable working patterns.

“I didn’t get where I am today by waffling.”
Charles Jefferson (The Fall and Rise of Reginald Perrin)

Chapter 1

Introduction

1.1 Background

“The beginning of wisdom is the definition of terms.”

Socrates (ca. 470–399 BC)

Nanoscience and nanotechnology

Since the launch (much to the annoyance of America, by the Russians) of the first satellite, *Sputnik 1* in 1957, we have very successfully conquered the realm of Earth-orbital space: at the time of writing, there are more than 3,100 active satellites in orbit (along with nearly ten times that number of defunct pieces of man-made space detritus).[†] We have sent probes to the outer planets, landed roving vehicles on Mars, and people have walked on the Moon.

One thing that the fields of nanoscience and nanotechnology have in common with the “space race” is that some of the wilder predictions made by their

[†]More up-to-date numbers are maintained at <http://celestrak.com/satcat/boxscore.asp>.

more controversial futurists have yet to come about, if indeed they ever will. There is no human colony on the Moon, interstellar travel is still a distant dream, and we have not made contact with highly intelligent extraterrestrial beings that have irrevocably changed our understanding of the Universe and our place within it. Perhaps fortunately, we have also as yet failed to come close to making the technological advances necessary to produce an army of self-replicating “nanobots” that will ultimately break free from the control of their human masters and bring about our demise in a puddle of “grey goo”.

The vision put forward by K. Eric Drexler in his 1986 book *Engines of Creation* is one of a revolutionary technology that will rid the world of energy problems, disease, and even ageing and death (see Fig. 1.1) [3]. Although such vision has its place and should not be dismissed as pure fantasy— Arthur C. Clarke apparently predicted the existence of carbon nanotubes, in the form of a “pseudo-one dimensional diamond crystal” in *The Fountains of Paradise* more than a decade before their discovery [4]— the present reality of nanoscale science and technology is more evolutionary and incremental. Computer processors are now routinely fabricated with feature sizes down to a few tens of nanometres, and transistors have been built that switch with a single electron [5]. Remarkable as these developments are, they are the result of continued research and development, and refinement of existing technologies: we have yet to build anything approaching a synthetic “molecular assembler”.

Synthetic molecular assemblers and self-replicating nanobots can broadly be put under the heading of “radical nanotechnology”. This kind of technology, for the moment, remains in the realm of science fiction. The fascinating reality is that we are already surrounded by, and heavily depend on nan-

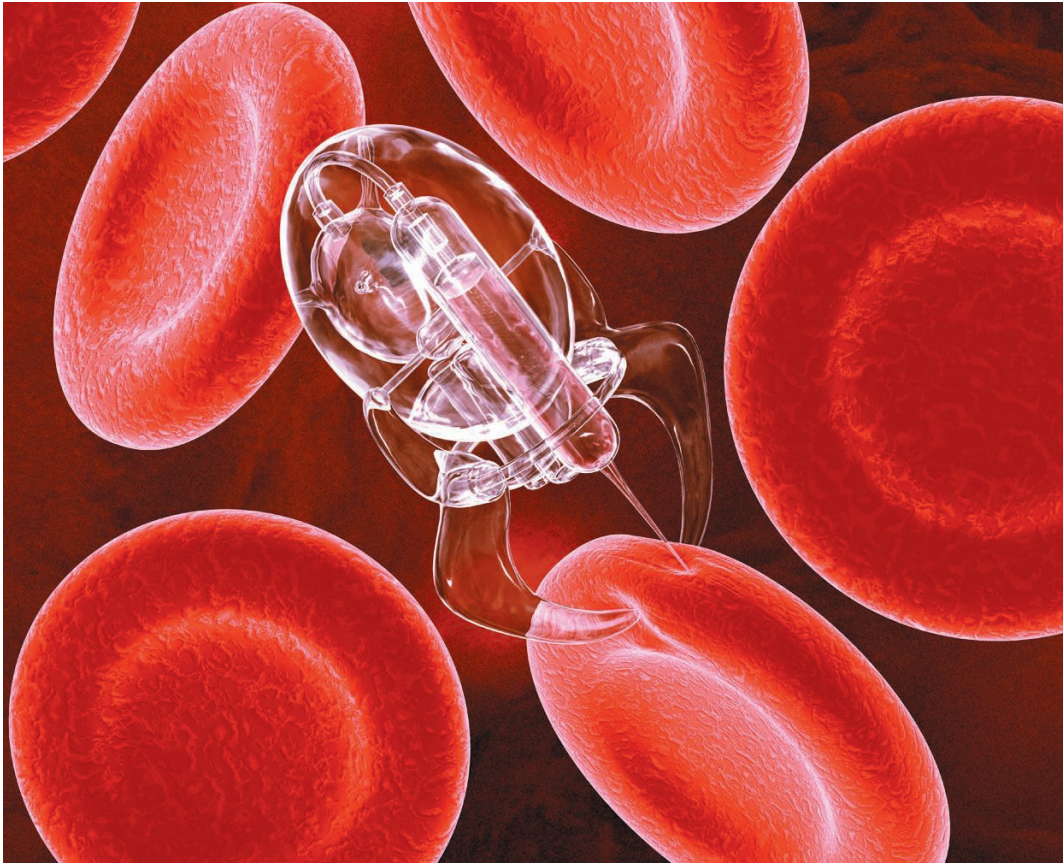


Figure 1.1: The (somewhat erroneous) public perception of nanotechnology and its potential. By Coneyl Jay, winner of the 2002 “Visions of Science Award” from *The Daily Telegraph*.

otechnology for our very existence. Millions of years of evolution have led to intricate mechanisms of molecular manufacture and a delicate balance of nanoscale processes in our own bodies. Indeed, the closest we have so far come to a true molecular assembler is by genetically modifying a bacterium to produce human insulin [6]. It seems likely that if we are to fully exploit physics at the nanoscale, we must take inspiration from the soft and wet mechanisms that nature has already created, rather than attempting to scale-down existing macroscopic engineering concepts [7].

At this juncture, it would be wise to define the terms we are using. The Royal Society and the Royal Academy of Engineering put forward different definitions for *nanoscience* and *nanotechnology* in their 2004 report into the ethical, safety, and social issues of nanoscale science [8]. According to their definitions, *nanoscience* is “the study of phenomena and manipulation of materials at atomic, molecular and macromolecular scales, where properties differ significantly from those at a larger scale”, whereas *nanotechnology* is “the design, characterisation, production and application of structures, devices and systems by controlling shape and size at nanometre scale”. While the latter emphasises design and practical applications, the former relates to study and understanding of the world at the nanoscale.

Put more simply, my interpretation of these definitions is as follows: nanoscience is the study of the properties of matter on the nanoscale, and nanotechnology is any technology which exploits the properties of matter on the nanoscale. Thus nanotechnology flows largely, but not exclusively, from nanoscience. If we accept these definitions— and there are those who would not— then the majority of this thesis relates to *nanoscience*, perhaps with the exception of Chapter Five. Even in Chapter Five, which discusses nanoscale *control*, if personal motivation is considered (and this is perhaps where the line blurs), then I still consider it to be nanoscience.

The birth of nanotechnology is often traced back to a lecture given in 1959 by Richard Feynman [11], but recently this assertion has been increasingly questioned. Although Feynman’s vision was undoubtedly both inspired and inspiring, it was largely ignored in terms of citations until the 1990s [12]. Arguably, *nanoscience* began with the first imaging of atoms in a lattice, with a

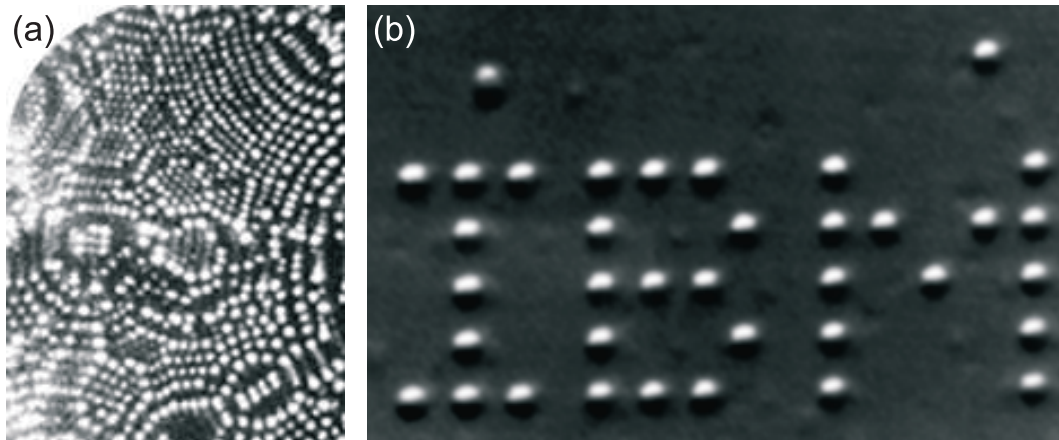


Figure 1.2: The beginnings of nanoscience and nanotechnology: (a) a field ion microscope image (FIM) of a rhenium surface, showing individual atoms [9], and (b) 35 xenon atoms precisely manipulated with a scanning tunnelling microscope (STM) tip to spell out “IBM” [10].

field ion microscope, by Erwin W. Müller in 1955 (Fig. 1.2a) [9]. The foundations of *nanotechnology* were firmly laid by Gerd Binnig and Heinrich Rohrer with the development of the scanning tunnelling microscope in 1981 [13, 14]. It was this innovation which paved the way for Don Eigler’s manipulation of xenon atoms with an STM tip to spell out “IBM” in 1989 (Fig. 1.2b) [10]. This picture, along with the unprecedented atomic control it represents, has become an iconic image of early nanoscale science.

Self-assembly and self-organisation

One of the possibilities that nanoscience presents is that of the creation of functional structures which automatically assemble themselves from their individual component parts. Current commercial nanotechnology (e.g. computer processor manufacture) almost invariably employs a “top-down” approach, where the starting material is macroscopic (e.g. a silicon wafer), and nanostructures

are then etched into the surface by various means. Numerous further process stages are then used to deposit different materials and attach contacts to make the final functional device. This is generally a complex and expensive process. An attractive alternative is to build a device from the bottom upwards, by carefully designing the component parts so that they will arrange themselves spontaneously into the required structure. The phrase “self-assembly” used in this context is somewhat more literal than when it is used to describe a certain type of inexpensive furniture.

For molecular self-assembly to work, the molecules involved have to be selected to “recognise” their correct location in the desired structure. Once again, nature has provided an excellent example of this in the form of deoxyribonucleic acid (DNA). The four bases of DNA (adenine, cytosine, guanine, and thymine) have *hydrogen bonding* groups positioned such that adenine will bond with thymine, and guanine will bond with cytosine (Fig. 1.3). The continued Brownian motion of the molecules in a single strand of DNA bases leads to their self-assembly into a low energy configuration with a complementary strand; numerous possible configurations are “tested” as molecules buffet one another, and those that are energetically favourable are most likely to remain stable. This leads to the formation of the familiar DNA double helix. The “recognition” ability of complementary DNA strands is being explored extensively for its potential in the self-assembly of nanodevices [15], and has already been harnessed to form functional devices such as a self-assembling nanotube transistor [16].

The basic principle of self-assembly is that all the information required to build the final structure is contained within the component parts, and encoded

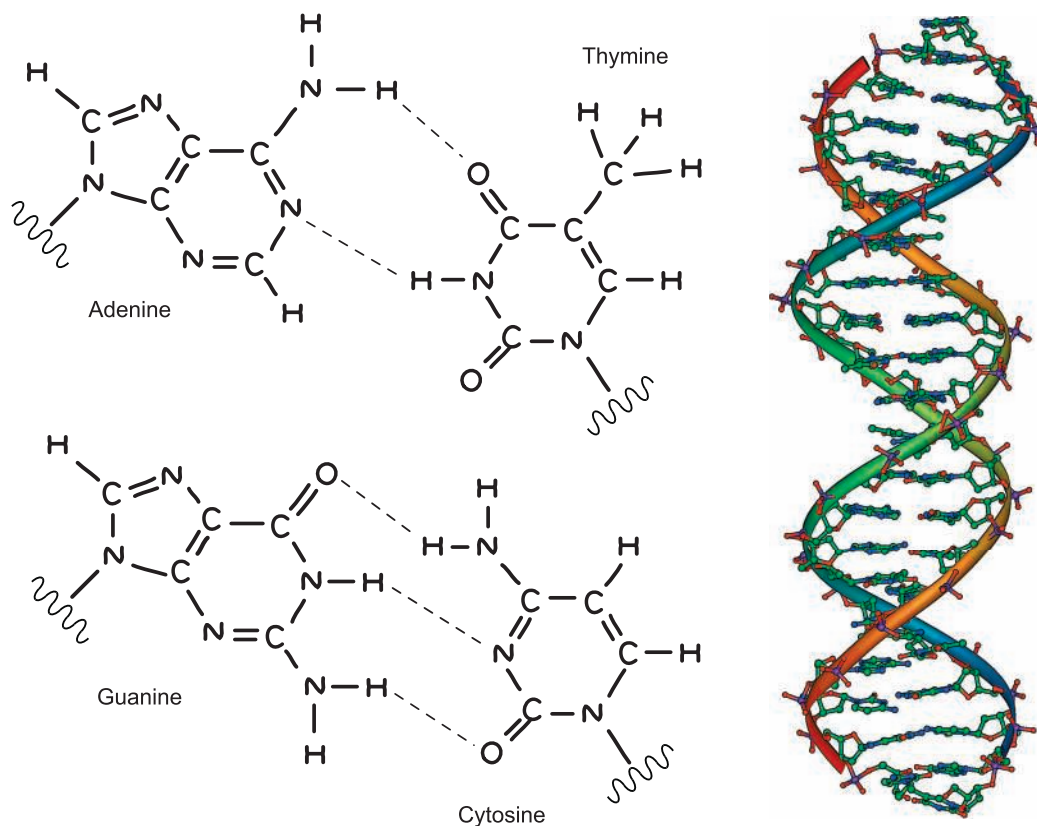


Figure 1.3: The two base pairs of DNA, showing dashed lines where the molecules “recognise” each other by hydrogen bonding (left), and a section of assembled DNA (right).

according to the laws of physics. All that is required to perform the actual assembly is some form of “shaking” to force the components to attempt different configurations until a stable low energy state is reached. In the case of molecular self-assembly, the Brownian motion of the molecules is usually all that is required. The advantages of this technique are numerous. Rather than using complex production lines in multi-stage processes, once the chemicals involved have been selected and synthesised it is often a case of simple “mixing” to obtain the desired results. This presents the possibility of massive parallelism in manufacturing, and a great reduction in process costs. However,

it should be noted that the production of more complex heterogeneous structures (such as those needed for a computer processor) will require ever more complex component design. This is a fact that may limit the development of elaborate self-assembled devices.

It is useful to distinguish self-assembly from self-*organisation* using the definition promoted by Richard Jones [17] (and others). To paraphrase: self-assembly can be said to occur in systems where the tendency to minimisation of free energy is the driving force behind the arrangement of the component parts into a more ordered configuration. This configuration can be maintained without the need for external intervention, such as the input of energy. Self-organisation on the other hand arises from a non-equilibrium process that is subject to an external driving force, such as heating. A classic example of this is shown in Fig. 1.4a. When a viscous liquid is heated from below, a vertical density gradient will be set up between the bottom and top surfaces (as most liquids have a positive thermal expansion coefficient). If the heating is sufficiently strong, this system will become unstable and fluid will rise from the bottom, setting up convection currents. These currents tend to spontaneously organise themselves into hexagonal patterns [18].

Numerous very visible examples of self-organisation exist in the natural world. The stripes and spots of many animal hides are understood to originate from self-organising autocatalytic reaction-diffusion systems in the womb [20]. An example is shown in Fig. 1.4b. A more detailed and elegant description of these, and many other self-organising systems can be found in Philip Ball's *The Self-made Tapestry* [21].

It should be noted that although both self-assembly and self-organisation

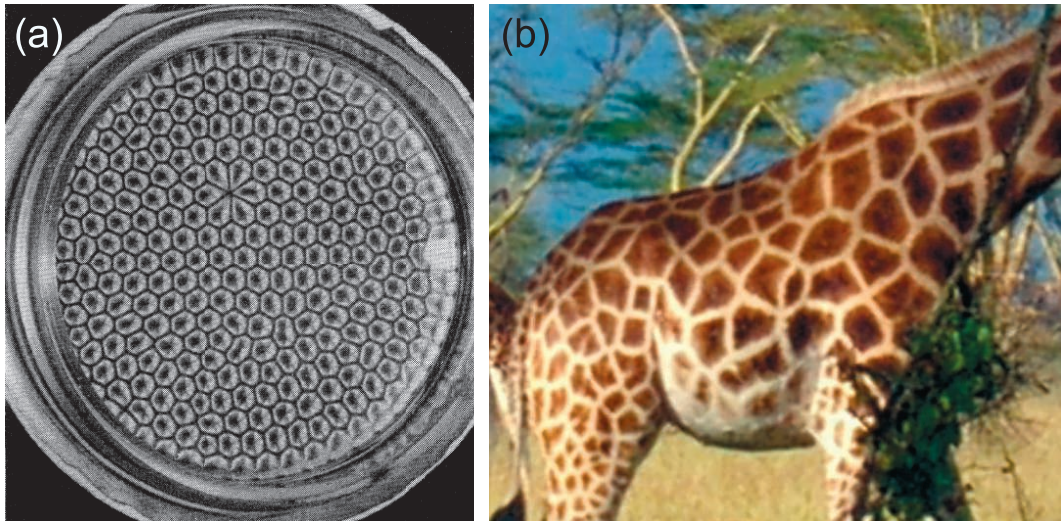


Figure 1.4: Two examples of self-organisation, showing (a) viscous oil in a Petri dish heated from below displaying Bénard convection (from Cross & Hohenberg [19]), and (b) the pattern on the hide of a Rothschild's giraffe in Kenya (courtesy of E. Pauliac-Vaujour).

appear to have a tendency to increase the degree of order of a system, this is not the complete picture. A common misinterpretation of the second law of thermodynamics is that the type of behaviour described here should not be possible. However, the building blocks of these systems are not increasing their degree of order in isolation. As self-assembling molecules hydrogen bond, energy is released into their surroundings in the form of heat, increasing the overall level of disorder in the Universe. Self-organising systems, by virtue of the definition above, involve a non-equilibrium transfer of energy, and thus an overall increase in entropy. Therefore we can say that the arrow of time, reassuringly, continues to point forwards, in spite of appearances.

Thin films

The physics of thin films on surfaces is an area that is of considerable importance in a diverse range of fields. Films of various kinds, such as paints, lubricating fluids, and optical anti-reflective coatings (to name but a few) rely on an understanding of the properties of layers of material a few microns, or even nanometres thick. In each of these cases, the ideal outcome is a uniform, unbroken, and stable layer. Although simple in concept, in practice this is not always an easy aim to achieve. A macroscopic depth of water in a glass will happily sit as a column under the influence of gravity. As the glass is emptied of its contents, however, it does not simply form a shorter column and then an ever thinner layer on the bottom. There comes a point when the influence of gravity is no longer the dominant factor in determining the shape of the liquid.

Interfaces between materials have an energy associated with their creation. Perhaps the most familiar manifestation of this is the surface tension of water (the energy associated with the interface between liquid water and air), which allows certain insects to “skate” on the surface of a pond without sinking. A raindrop in free-fall will try to minimise its surface area, and thus its free energy, by forming a sphere. In the case of a drop on a solid surface, there are three interfacial energies that need to be balanced: those between the solid and liquid, solid and gas, and liquid and gas (Fig. 1.5). The balance of these interface energies will determine the macroscopic *contact angle*, and whether the liquid *wets* the surface, or will “bead up” and *dewet*. Although dewetting is desirable in raindrops on a windscreen, it is very much unwelcome in the oil on the surface of a piston. Dewetting is a complex process, the dynamics of

which can be affected by many factors. This shall be explored in more detail in Chapter Two.

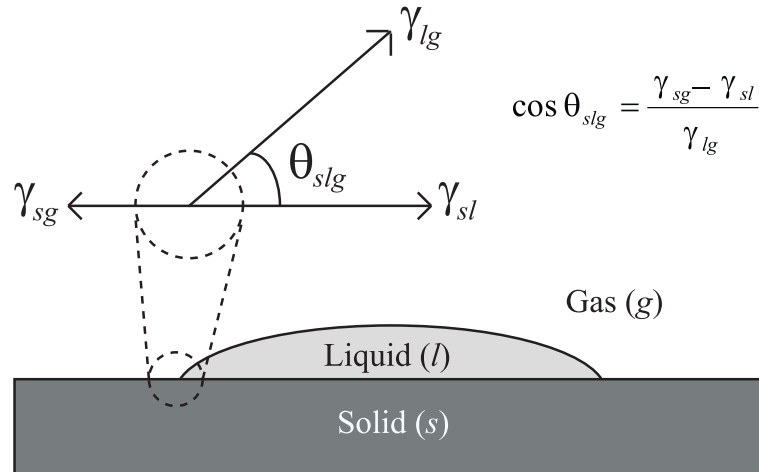


Figure 1.5: A liquid drop on a solid surface, showing how the contact angle, θ_{slg} , arises from the balance of the interfacial energies (or surface tensions) between the solid and liquid (γ_{sl}), solid and gas (γ_{sg}), and the liquid and gas (γ_{lg}).

Nanoparticles

Nanoparticles, as the name would suggest, are collections of matter with dimensions that are most appropriately measured in nanometres (typically $<100\text{nm}$). There is no real limit to the materials from which they can be made, nor the manner in which they are produced. The important fact is that once a material is broken down into such small units, its properties can change significantly. Notably, the very high surface-to-volume ratio of nanoparticles makes them potentially very much more reactive than their bulk counterparts. This in turn makes them good candidates for catalytic processes, in which available surface area is key to the rate of reaction [22]. Commercial uses of

nanoparticles have so far mostly been limited to bulk applications, such as the use of titanium dioxide nanoparticles to produce “transparent” sunscreen [23]. Their use as electronic devices in the form of “quantum dots” is still very much at the stage of ongoing research.

The size effects of nanoparticles have been exploited, albeit unwittingly, since the middle ages, when uniformly dispersed gold nanoparticles were used to give glass a rich ruby colour. This has since been attributed to the surface plasmon resonance of the gold particles. Interestingly, the colour of a dilute colloidal solution of nanoparticles can give quite an accurate indication of the size of the particles involved [24]. An overview of the structure and properties of metal nanoparticles in general is presented by Günter Schmid [25], and Daniel & Astruc have written an extremely comprehensive review of gold nanoparticles [26].

The majority of the nanoparticle discussions in this thesis relate to solutions of *thiol-passivated* gold nanoparticles. *Passivation* is the process by which otherwise highly reactive particles are made stable and prevented from aggregating into larger clusters. Nanoparticles can be stabilised in solution either by giving each an electronic charge allowing them to dissolve in a polar solvent (while still repelling one another), or by attaching passivating *ligands* which can be tailored to the specific particles and the solvent in which they will be dissolved. A thiol is a molecule which consists of a hydrocarbon “tail”, and a sulphur “head”. Thiol-passivated gold nanoparticles can be produced in solution by a process of self-assembly, as the thiol molecules find it energetically favourable to bond to the surface of gold (Fig. 1.6). The collection of alkane “tails” that is left to protrude from the particle allow it to dissolve in an

organic solvent without aggregating and precipitating. Such particle solutions are stable for many years, and can be allowed to evaporate and re-dissolve without detriment to their properties. The details of the specific method used for producing these particles are described by Brust et al. [27].

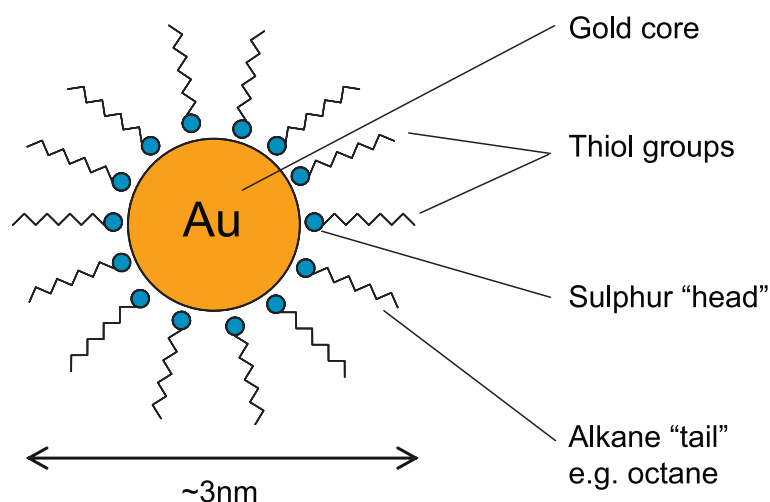


Figure 1.6: The schematic structure of a thiol-passivated gold nanoparticle.

When a few tens of microlitres of a solution containing these particles is deposited onto the surface of a piece of silicon wafer, which is then spun at several thousand revolutions-per-minute until all visible traces of solvent have disappeared, the diversity in the array of nanostructured patterns which are formed on the substrate is nothing short of astonishing. The work in this thesis represents a study of the nature of these patterns, and the manner in which they are formed. The complex mechanisms involved are explored by a combination of experiments and simulations, in order to attempt to ascertain exactly what happens in the last few hundred milliseconds of spin-casting, when a layer of liquid just a few nanometres thick remains.

1.2 Thesis outline

The previous section presented a broad background to the field of nanoscience, and described the context in which the rest of the work in this thesis is based. The coming chapters will further refine this context and describe the techniques that will be used in the later chapters to further our understanding of pattern formation in nanoparticle arrays.

Chapter Two: This chapter presents the different morphologies that are observed in non-equilibrium pattern formation, and gives some examples of systems in which they occur. There is a discussion of dewetting in thin films, and a review of the current understanding of pattern formation in nanoparticle systems.

Chapter Three: The experimental techniques used to create, image, and analyse pattern formation in nanoparticle structures are described in this chapter. The basis of the simulations used extensively in later chapters is presented here, along with a background description of Monte Carlo simulation in general.

Chapter Four: Techniques for analysis and comparison of two-dimensional structures are first described, and then applied. There is a discussion of the implications for the way in which these structures are formed.

Chapter Five: An experimental technique is described here that enables ex-

tremely localised control of the morphology of nanoparticle structures. Modifications to the simulations described in Chapter Three allow accurate reproduction of these effects, as demonstrated by comparisons using the tools described in Chapter Four.

Chapter Six: Mechanically-induced dynamic scaling behaviour of nanoparticle networks in experiments is investigated, and analysed with reference to simulations. There is a description of a genetic algorithm technique, which enables automatic exploration of the simulation parameter space to find the parameters required to reproduce a particular experimental structure.

Chapter Seven: Summary and discussion of the main results presented in this thesis, and suggestions for further work.

Chapter 2

Non-Equilibrium Pattern Formation

“Nature uses only the longest threads to weave her patterns, so each small piece of her fabric reveals the organization of the entire tapestry.”

Richard P. Feynman (1918–1988)

In the previous chapter, I touched on the idea that the formation of patterns by self-organisation is a common feature of natural systems. Indeed, it seems that, particularly in biological structures, the emergence of some type of pattern is the rule rather the exception. Certain types of pattern seem ubiquitous, and emerge not only in very different kinds of system, but also across many orders of magnitude of scale. This chapter presents some examples of the most common non-equilibrium morphologies, discusses how they emerge in the dewetting of thin films, and finally gives an overview of the patterns found in nanoparticle assemblies.

2.1 Common morphologies

2.1.1 Cellular networks

A very common pattern that appears in an extremely diverse range of systems is the *cellular network*. The exact form of a cellular network can vary quite widely, but the underlying definition remains the same: a structure that is separated into individual polygonal *cells* by clearly defined boundaries [28]. Two examples of cellular networks have already been seen in Fig. 1.4— one biological and one distinctly physical. Further examples are shown in Fig. 2.1, in both two and three dimensions.

Two-dimensional patterns

Convection cells in a fluid are a classic example of non-biological self-organisation, with the heat source providing a non-equilibrium driving force. Although self-organisation such as this requires a flow of energy, many structures exist that are the result of a self-organisation process that has been “frozen in”. In the case of Fig. 2.1a, this is almost literally true. As a thick lava flow cools from the upper surface downwards, thermal contraction of the solidifying basalt causes cracks to appear in the top of the flow. As the lava continues to cool, the rock continues to shrink, and the original cracks propagate downwards to form polygonal columns. The pattern, and thus the evidence for the history of the rock, persists long after it has reached thermal equilibrium with its surroundings.

The initial pattern of cracks in columnar basalt is not unlike that which appears in drying mud (Fig. 2.1b), and is in fact the result of a very similar

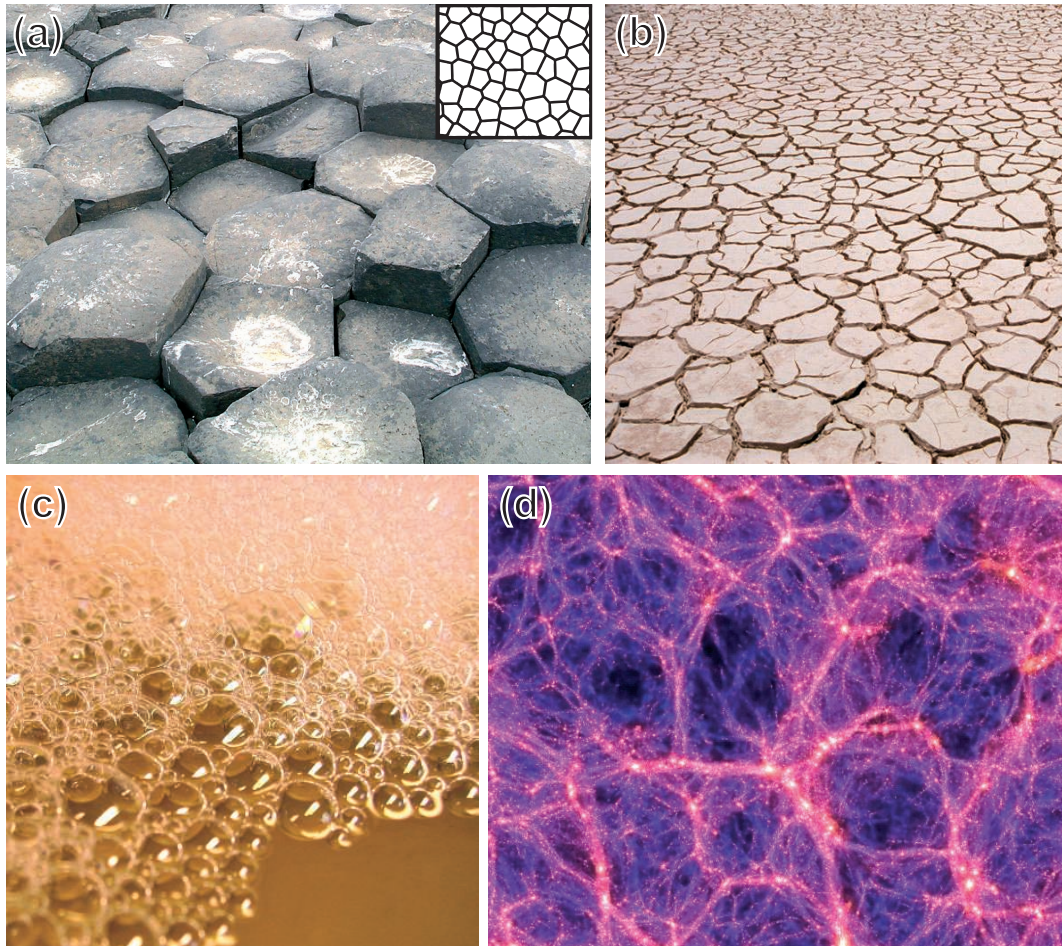


Figure 2.1: Natural examples of cellular structures, showing (a) part of the columnar basalt structure known as the “Giant’s Causeway” in Antrim, Northern Ireland, with an accurate sketch of another region of the same (inset, from [28]), (b) cellular patterns of cracking in dry mud, (c) soap foam— a familiar manifestation of a three-dimensional cellular structure, and (d) a section from the “Millennium Simulation”, a supercomputer model of the formation of large-scale structure in the Universe, which is remarkably foam-like, and has long filaments of matter separated by large voids [29].

underlying physical process. As mud dries, it will contract and pack into a solid layer until the lateral tensile stress can no longer be maintained. The size (and indeed the form) of the resulting pattern depends on the nature of the medium: factors such as tensile strength and coefficient of expansion will determine the scale (or *wavelength*) of the final pattern. The individual varying shapes of mud “islands” are the result of local fluctuations in parameters such as temperature, composition, density, humidity, and the presence of flaws or impurities such as small stones.

Although it is intuitively apparent that these structures are similar to one another, it is perhaps not as easy to define their similarity analytically. Honeycomb, for example, is mathematically an extremely well defined structure, consisting of identical tessellating hexagonal units. However, although the human brain is able to recognise that there is a pattern on the hide of a giraffe, it does not consist of identical repeating units. It is here that a description in terms of *topology*, rather than geometry, becomes essential. The *Voronoi tessellation* is a device that allows just such a description, and also enables classification and comparison of two-dimensional cellular structures [28]. This, along with other classification and comparison techniques for cellular networks shall be presented in detail in Chapter Four.

Three-dimensional patterns

A cellular network in three dimensions is commonly referred to as a “foam”, the most obvious example being a soap foam such as that shown in Fig. 2.1c. A soap foam is in fact an interesting example of both self-assembly and self-organisation. The formation of bubbles in water is only made possible by

the presence of surfactant molecules. These are similar in structure to the thiol molecules used to passivate gold nanoparticles: an ionic (water soluble) “head” is attached to a hydrocarbon (hydrophobic) “tail”. These molecules will self-assemble at the surface of water with their insoluble “tails” protruding, in an attempt to minimise their free energy. In so doing, they also stabilise thin films of water by lowering their surface tension. When soapy water is subjected to turbulence at its surface or an injection of gas, closed bubbles are able to form. Collections of these bubbles will self-organise into the efficient space-filling arrangements we know as foams.

Myriad other examples of three-dimensional foams exist, from polymer foams used as insulation or protective packaging, to the head on a pint of beer. Interestingly, although the mechanisms involved are entirely different, the large-scale distribution of galaxies in the Universe is apparently also much like a giant soap foam (Fig. 2.1d) [29, 30]. A detailed description of the nature and behaviour of foams in three dimensions is perhaps outside the scope of this work, as indicated by the fact that Weaire & Hutzler have dedicated an entire book to the subject [31].

Different physics, same maths, same solutions

The precise mechanism by which a cellular structure will self-organise is dependent on the physical nature of the particular system. This raises the question of the origin of cellular networks: a soap foam appears to be a microcosm of the Universe, but how can the structures be so similar when the physics involved in each case is so fundamentally different? The reasons can in fact be found in the the mathematics of *space filling*. In a system that undergoes a breaking

of symmetry— such as the transformation from the homogeneous and isotropic surface of damp mud to the cracked and inhomogeneous surface of dry mud— there is necessarily a partitioning of space into smaller units. Regardless of the specific physics involved, this division of space can very often be achieved most efficiently by the formation of a cellular network.

In the case of cracking mud, the cellular network provides a minimum total crack length to relieve the tensile strain; in the case of a soap foam, forming a three-dimensional cellular network will minimise the total surface area required to contain the trapped pockets of gas. Deviations from an ideal partitioning of space in such systems can result from inhomogeneity before network formation, or the existence of physicochemical processes specific to that system. However, in each case the underlying principle driving the system towards a cellular structure is the mathematics and geometry of filling space efficiently. A comprehensive and very readable review of the structure and dynamics of cellular systems is presented by Weaire & Rivier [28], which was later built upon and updated by Schleiker to include more recent developments [32].

2.1.2 Spots, stripes, and labyrinths

Many systems exhibit patterns that are best described as “spots” or “stripes”. In the absence of restricting boundary conditions, stripes often fold back on themselves to become complex meandering bicontinuous structures. These are appropriately known as “labyrinths” after the Cretan home of the Minotaur in Greek mythology [33] due to their topological similarity. Once again the most obvious examples of these pattern types are biological: the hides of an-

imals such as the leopard and the tiger. This section presents two examples of systems that can produce all three of these patterns, and describes the mechanisms involved in the production of each.

Reaction-diffusion systems

Evolution is fundamentally lazy, or more accurately *economical*, and the maintenance of complex structures and processes is only justified if there is a dramatic survival advantage [34]. Although the survival advantages of blending into dappled shade are obvious, the original mutation that caused the emergence of these patterns found a relatively simple way by which to create them. Evolution managed to stumble upon a *reaction-diffusion system* as a way to let physics form the patterns, and the only genes required are those to produce the right concentrations of chemicals in the epidermis during gestation.

In 1952 Alan Turing proposed a mechanism by which dynamically maintained yet stationary patterns could emerge from a chemical reaction [20]. An *auto-catalytic* reaction is one in which a reaction product is able to catalyse its own production. On their own, such reactions progress at an initially slow rate which will increase as more product is formed, until the rate begins to level off as the reagents are depleted. If such a reaction also produces a second, fast-diffusing chemical that inhibits the rate of reaction, spatial patterns in reagent concentration can be set up: the inhibitor will diffuse away from the catalyst, creating regions high in inhibitor around areas high in catalyst.

When combined with processes that remove both end products from the system, the resulting patterns in concentration can be stably maintained. Two simulated patterns resulting from slightly different diffusion parameters are

shown in figure 2.2. It is a reaction of this type that is the chemical basis of the *morphogenesis* of patterns in many animal hides. The transition from spots to labyrinthine patterns to more uniform stripes is often the result of the boundary conditions (i.e. the shape) of the animal in question [35].

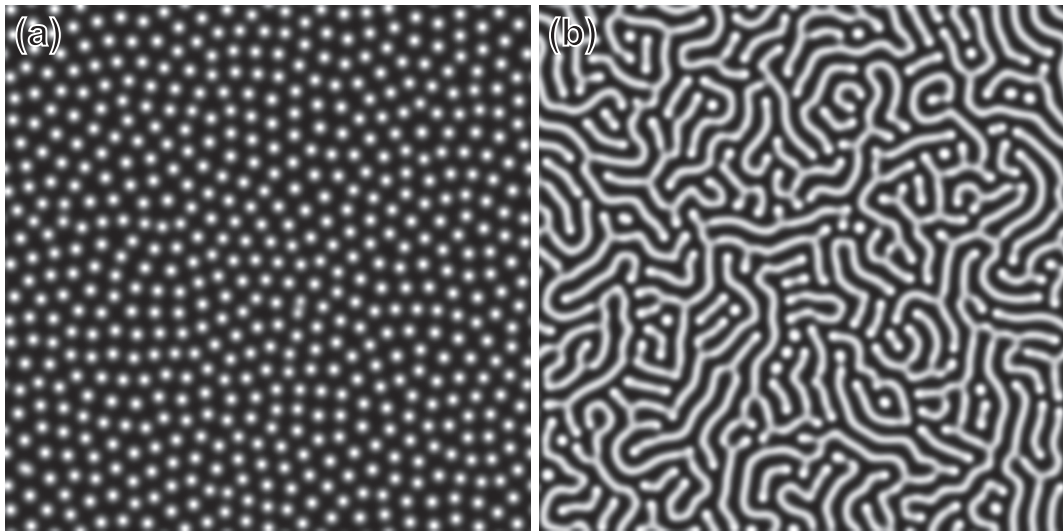


Figure 2.2: Two different morphologies (known as “Turing patterns”) in a simulated reaction-diffusion system, showing (a) spots, and (b) labyrinthine stripes.

Spinodal decomposition

Under certain conditions, a mixture of materials (e.g. two polymers) will spontaneously separate into two distinct phases of different composition by means of amplification of local infinitesimal fluctuations in density or composition. Such processes, are put under the general label of *spinodal decomposition*. Spinodal decomposition is a result of the shape of the curve of free energy as a function of composition, ϕ . If this curve is completely concave, then a mixture will be stable at any value of ϕ , as decomposition into two phases would raise the energy of the system. If however there is a region of the free energy curve

that is convex (as in Fig. 2.3a), then a mixture in this region (composition ϕ_1 , at free energy F_0) can reach a lower energy state by separating into two phases (ϕ_2 and ϕ_3 , combined free energy $F'_0 < F_0$). At the peak of such a local maximum in the free energy curve, the mixture is globally unstable with respect to small local fluctuations in composition, and will spontaneously decompose into two phases [36].

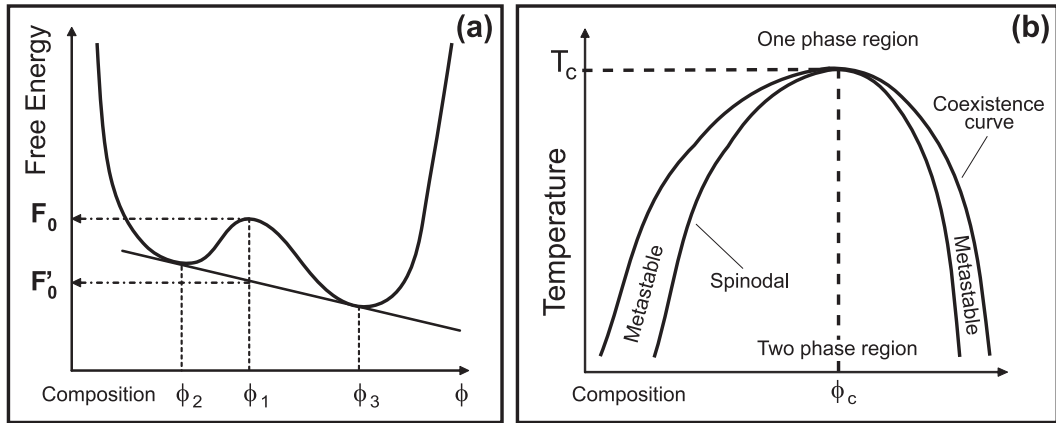


Figure 2.3: An explanation of spinodal decomposition, showing (a) how the shape of the free energy curve can lead to demixing, and (b) a schematic phase diagram for such a mixture of two polymers. The coexistence curve separates the region where the mixture exists as a stable single phase. Between the spinodal line and the coexistence curve, the free energy can be lowered by separating into two phases. Below the spinodal line, the mixture is unstable with respect to infinitesimal fluctuations in composition, and will spontaneously separate.

Fig. 2.3b shows a schematic phase diagram for such a system. The spinodal line represents the edge of the region where the mixture will spontaneously separate. Above this line, and below the coexistence curve, the mixture will separate provided it receives the activation energy necessary to remove it from metastability. Above the coexistence curve, the material exists as a stable mixture. One way to induce spinodal decomposition is to start with a mixture

at ϕ_c but above T_c , then quench down through the critical point where the two curves meet. Phase separation will occur at this critical point.

For a given system, there is a natural or *preferred* length scale at which spinodal decomposition occurs. This is because low spatial frequency fluctuations in composition are only able to grow slowly due to the large distances necessary for transport of material, and high spatial frequencies are suppressed due to a high free energy penalty for sharp composition gradients. Thus, a dominant wavelength will emerge and the type of pattern that results will depend on the specific nature of the system involved. The most common patterns that result from spinodal decomposition are very similar to those seen in reaction-diffusion systems.

2.2 Dewetting of thin films

As noted earlier, the dynamics of dewetting are somewhat complex. Although the macroscopic contact angle of a liquid on a surface can be explained by a simple balancing of macroscopic interfacial energies [37], the microscale and nanoscale behaviour of a fluid on a surface depends on the competition between long-range (van der Waals) and short-range (e.g. polar) interactions [38]. The nature and strength of these forces will determine the shape of the *interface potential*, and therefore the particular manner in which dewetting will occur.

The formation of patterns in spin-cast nanoparticle arrays is inextricably linked to the dynamics of dewetting at the nanoscale; the way in which the film of solvent flows, dewets, and evaporates during spin-casting is the major determining factor in the arrangement of particles on the eventually dry sub-

strate. This section will discuss the theory behind the dewetting of thin films, and examine different modes of dewetting and the physics behind them.

2.2.1 The interface potential

The interface potential $\phi(h)$ is a function which describes the free energy per unit area of two surfaces at a separation h . In the case of a thin film, the two surfaces are the solid-liquid and the liquid-air interfaces, and h is the thickness of the film. Fig. 2.4a shows three schematic forms of interface potential that correspond to films that are stable, unstable, or metastable [39].

The stable potential decreases monotonously away from the substrate, and has its minimum at infinity. A film with a potential of this form will not dewet at any thickness, as there is an energetic cost for the film to become thinner. The other two curves both have a minimum at a finite film thickness, h_{min} . In the case of the unstable potential, this means that the film is able to reduce its free energy by changing thickness, and this will initiate dewetting; a film with a thickness below h_{min} will attempt to increase its thickness, and a thicker film will try to thin towards h_{min} . The metastable case represents a film which may be stable under certain conditions but not others. Such a film will be unstable for small film thicknesses, but films above a critical thickness h_c will be stable until some kind of perturbation causes the nucleation of a hole, which will then be able to grow.

It is perhaps easier to understand the physics behind the dewetting of thin films in terms of the *disjoining pressure*, Π . This is defined as the first derivative of the interface potential with respect to film thickness, $\phi'(h)$, and

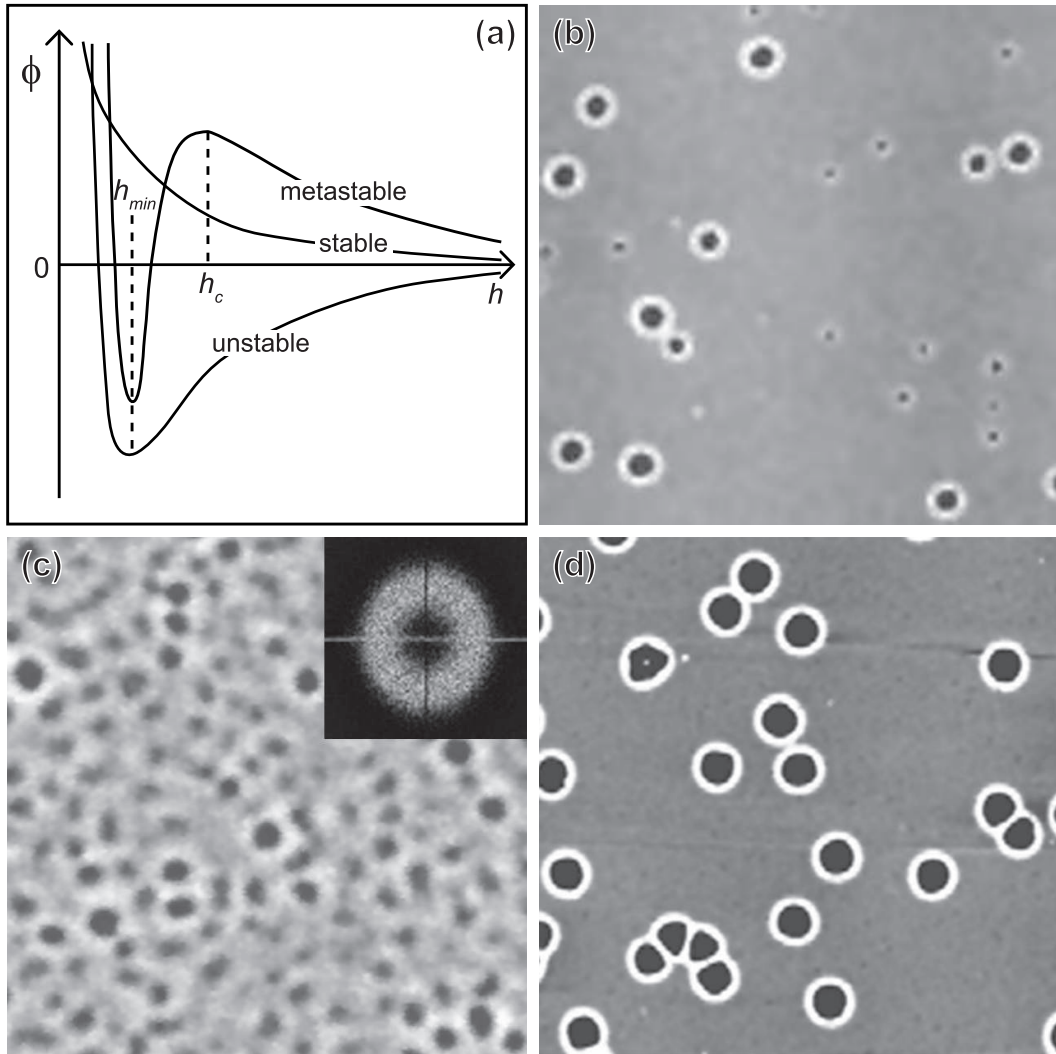


Figure 2.4: The physics of dewetting, showing (a) three schematic interface potentials, and optical micrographs of the three modes of dewetting: (b) homogeneous thermal nucleation in the metastable regime, (c) spinodal dewetting in an unstable or metastable film, and (d) heterogeneous nucleation, also in an unstable or metastable film (from [40]).

can be expressed as a linear combination of three structural components [38]:

$$\Pi = \Pi_w + \Pi_e + \Pi_s, \quad (2.1)$$

where Π_w arises from van der Waals (vdW) forces between the film and the substrate, Π_e accounts for short-range electronic or polar interactions, and Π_s is a structural component relating to the fact that molecules in a thin film may have a different structure from those in a bulk liquid.

The minima of the curves shown in Fig. 2.4 at thickness h_{min} could occur in a material such as a polar polymer because the molecules can lower their energy by aligning on a polar surface [41]. Such a minimum therefore often equates to a thickness of one monolayer. The surface alignment of a molecule with polar end groups can sometimes lead to the added complication of *autophobicity*, where a liquid is unable to spread on its own monolayer [42]. A review of wetting at polymer surfaces and interfaces, which includes an overview of the demixing of polymer blends discussed earlier, was recently compiled by Geoghegan & Krausch [43].

2.2.2 Dewetting modes

In general, dewetting proceeds first by the formation of holes, which then grow and coalesce, until finally the remaining threads of liquid break up by Rayleigh instabilities leaving individual droplets [44, 45]. An example of such a sequence is shown in Fig. 2.5. A film may dewet by means of any one of three major mechanisms: homogeneous (thermal) nucleation; heterogeneous (defect) nucleation; or spinodal dewetting (Fig. 2.4b-d).

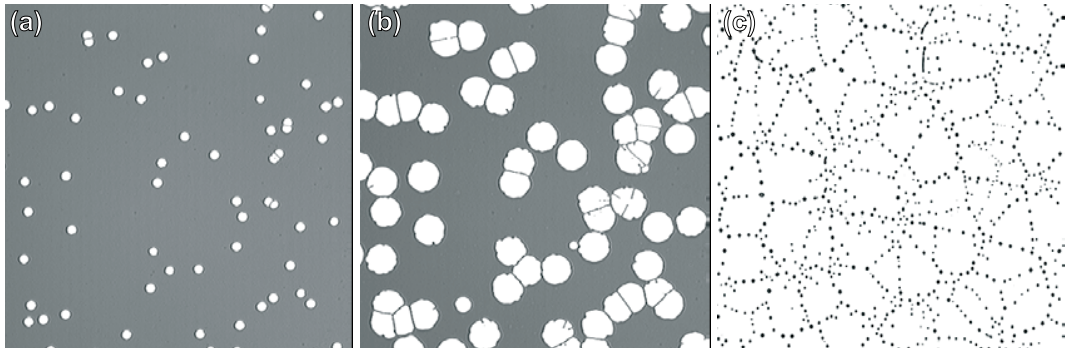


Figure 2.5: Optical micrographs showing three stages of defect-nucleated (heterogeneous) dewetting in an 80 nm thick polystyrene film on hydrophobic silicon (from [46]) showing (a) nucleation of holes, followed by (b) their growth and coalescence into a cellular structure, and (c) droplets formed by the break-up of the cell walls due to the Rayleigh instability.

Thermal nucleation

A film in a metastable state is able to begin the process of dewetting by overcoming the activation energy for nucleation of a hole by local thermal fluctuations. This is particularly likely if the film is not much thicker than h_c , as the activation energy for nucleating a hole will be relatively small. This kind of process is characterised by spatially and temporally homogeneous nucleation. As shown in Fig. 2.4b, the holes produced are not spatially correlated, and appear at varying points in time. They are therefore a range of different sizes.

Heterogeneous nucleation

In thicker metastable and unstable films, foreign particles in a system (such as dust) or irregularities in the substrate can nucleate holes in the film. Such defects are present at the time of film deposition, and are usually distributed in a random *heterogeneous* pattern. Because of this, heterogeneous nucleation is characterised by randomly distributed holes which all appear in a very short

time window, and are all therefore a very similar size (as neatly illustrated by Jacobs et al. [47]).

Spinodal dewetting

Spinodal dewetting, as the name would suggest, is analogous to spinodal decomposition in a binary fluid mixture. Similarly, it is the result of a non-monotonic free energy curve. Spinodal dewetting takes place in an unstable or metastable film where the second derivative of the interface potential with respect to film thickness is negative ($\phi''(h) < 0$) [48]. In other words, spinodal dewetting can occur in regions where the disjoining pressure decreases with increasing film thickness ($\Pi'(h) < 0$). In this regime, the film becomes extremely sensitive to minor fluctuations in height, and capillary waves are amplified. This amplification occurs most strongly at a well defined wavelength (for very similar reasons to those described in the case of spinodal decomposition), and the whole film ruptures with holes of a similar size at almost the same instant [49].

2.2.3 Distinguishing between dewetting modes

There have been numerous theoretical and experimental studies of thin film dewetting. Polymer systems are particularly useful in this field for the tunability of their interactions, and polystyrene (PS) on silicon has been especially frequently examined [40, 44–47, 50–53]. Investigations into numerous other polymer systems have been undertaken [41, 54–57] and also into materials as diverse as solutions of collagen [58–60] and thin films of metals [61]. Recently, Sharma & Verma devised a three-dimensional numerical model, which appears

to reproduce many of the microscale dewetting morphologies that are seen in systems that are macroscopically wetting [62].

There continues to be significant debate about the exact mechanisms involved in dewetting in a number of systems. For example, despite the large quantity of literature devoted to PS on silicon, there still seems to be no clear consensus [63]. This is possibly because different mechanisms can dominate under different conditions. Both spinodal dewetting and heterogeneous nucleation have been reasonably conclusively observed in PS on silicon. Both mechanisms have in fact been seen to occur in parallel in other systems [60,61]. Such combinations render analysis of the final structures somewhat difficult. Furthermore, in many cases the early and intermediate stages of dewetting are not directly observable (unlike Fig. 2.5), so the origin of a particular dewetted structure can be unclear.

The ability to distinguish between different dewetting mechanisms is highly desirable, as it can give an insight into the shape of the interface potential, and thus the physics underlying the process. A discussion of real and reciprocal space techniques for investigating dewetting in polymer system is presented by Müller-Buschbaum [64].

2.3 Patterns in nanoparticle arrays

There has been a significant amount of interest in recent years in the deposition of nanoparticles from solution. The majority of work to date has focused on assembling highly ordered arrays of nanoparticles. For a solution of particles that are all very close to being the same size (are *monodisperse*), there are a

number of techniques that allow each particle to find an equilibrium position in a highly ordered *superlattice*. Superlattice structures are so named as they are effectively a larger-scale analogy of atomic lattices, comprising hexagonally close-packed arrays (or in two dimensions, a face-centred-cubic (FCC) *super-crystal*) of nanoparticle “atoms”. In the last decade, these structures have been well studied.

Little is yet understood, however, about the disordered structures formed during spin-casting of nanoparticle solutions. This is a regime in which solvent is evaporating so fast that it is best described as being *far from equilibrium*. In this regime the particles do not self-assemble into highly ordered arrays, but rather self-organise into a wide range of complex patterns, which are “frozen in” by the rapid evaporation of the solvent. Many of the patterns produced in this way bear a strong resemblance to the structures discussed in the previous sections of this chapter. This section describes some of the morphologies obtained from nanoparticle solutions both by slow evaporation and by spin-casting, and considers the mechanisms that have been suggested for their formation.

2.3.1 A brief history of nanoparticle superlattices

The first reported creation of a nanoparticle superlattice (although it was not given this name until several years later) was by Giersig & Mulvaney in 1993 by a process of electrophoresis [65]. In their experiments, citrate-stabilised particles were removed from solution onto a transmission electron microscope (TEM) grid by using them as the charge-carrying agents in an electrolyte, by applying a small voltage. These structures were only ordered over relatively short distances, possibly as a result of their low monodispersity: the

monolayers produced by this method exhibit grain boundaries where different orientations of nanoparticle packing meet (Fig. 2.6a).

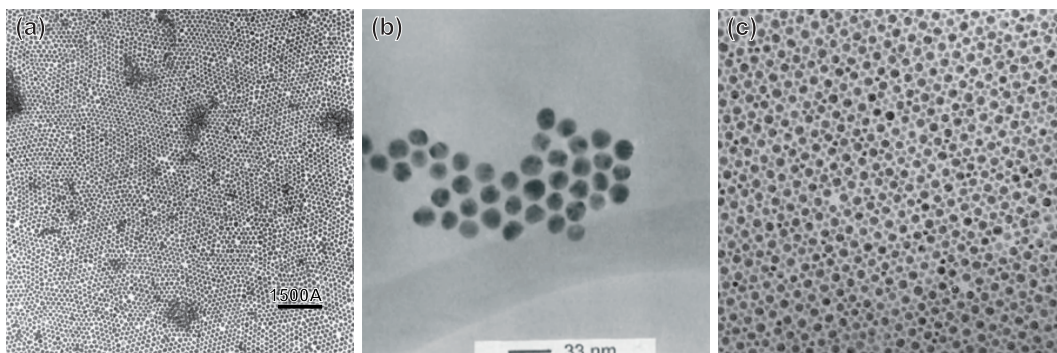


Figure 2.6: Transmission electron microscope (TEM) images of nanoparticle superlattices, showing (a) a monolayer of citrate-stabilised gold nanoparticles prepared on a carbon-coated copper grid (a “TEM grid”) by electrophoresis [65], (b) an aggregate of DNA-linked gold nanoparticles [66], and (c) an ordered bimodal array of 4.5 ± 0.8 and 7.8 ± 0.9 nm gold particles [67].

An interesting step taken by Mirkin et al. in 1996 was to functionalise nanoparticles using complementary strands of DNA to guide their self-organisation [66]. This led to the formation of relatively small, but highly ordered aggregates of nanoparticles (Fig. 2.6b). These aggregates give solutions a distinctive colour according to their size, as discussed in Chapter One. The suggestion made in the concluding remarks of this paper is that the technique could therefore be adapted for colourmetric sensing of particular DNA sequences.

In the same year, Andres et al. reported the formation of highly ordered structures of thiol-passivated gold particles simply by spin-casting [68]. The synthetic technique used in this work is somewhat more complex than that described by Brust et al. [27], but has greater flexibility in terms of the types of particles that can be produced, and results in solutions that are somewhat

more monodisperse. The high degree of order observed in their arrays likely occurred in relatively localised regions of the TEM grid.

Some interesting scanning tunnelling microscope (STM) images of nanoparticle superlattices were obtained in 1997 [69], and in the same year examples were found of superlattices packing into face-centred-cubic (FCC) arrangements in three dimensions [70]. Possibly the most striking images, however, were taken of two-dimensional structures, and by TEM: highly ordered *bimodal* arrays were created by Kiely et al. in 1998 [67] (Fig. 2.6c). The structures produced in this work were formed by slow evaporation of a single drop of solution containing two distinct sizes of particle on a TEM grid. In addition to the bimodal ensembles, regions consisting exclusively of the larger or smaller particles were observed.

Some advances in the control of drop-deposited superlattice structures were made in 1998 [71], but a leap in theoretical and experimental understanding occurred with the addition of excess thiol molecules to the solution in 2001 [72]. This was believed at the time to slow the evaporation rate, allowing each particle more time to find an equilibrium site in the superlattice. An X-ray scattering study [73] later indicated that superlattice formation occurs at the liquid-air interface in this case, rather than the substrate-liquid interface as was previously believed. Two years later, it was found that rather than retarding evaporation rate, excess thiol actually acts to nucleate the formation of superlattice assembly at the liquid-air interface. Armed with this understanding, Bigioni et al. were able in 2006 to produce truly long-range ordered lattices consisting of around 10^8 particles on a $3\text{mm}\times 4\text{mm}$ Si_3N_4 substrate (Fig. 2.7) [74].

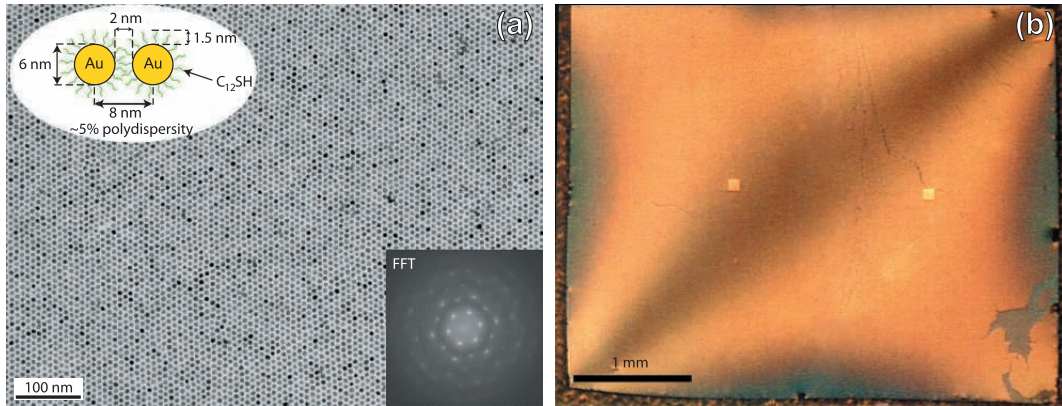


Figure 2.7: Gold nanocrystal monolayer from [74], showing (a) a TEM image of a region of the array with inset detail of array dimensions and a 2D Fourier transform of the same, and (b) an optical micrograph of a highly ordered particle monolayer on the surface of the solvent before drying. The extent of the monolayer can be visualised by the defect present in the lower right hand corner, and the cracking visible near the centre.

Numerous other superlattice systems have been examined in a variety of conditions [75–79], and several reviews have been written about their synthesis, characterisation, properties, and crystal structure [80–84]. These equilibrium structures are of still of significant interest for their unique electrical and physical properties, but their formation mechanisms are now reasonably well understood. The formation mechanisms involved in more disordered self-organised patterns, however, are much less well understood. Far-from thermodynamic equilibrium, structures can be formed on a range of length scales spanning several orders of magnitude—far beyond the particle size or the reach of inter-particle forces. The ability to control the size of the features in such systems—and hence their electrical and physical properties—would present significant potential in a range of technological applications. Understanding and controlling the mechanisms involved in the formation of these structures is the focus of the work in this thesis.

2.3.2 Far from equilibrium pattern formation

At the turn of the millennium, in parallel to the work on highly ordered arrays, work began on understanding the more disordered structures that are produced from nanoparticle solutions. Ge & Brus reported the range of structures that form when solutions of 4nm diameter cadmium selenide (CdSe) particles are spin-cast onto graphite substrates [85]. A summary of the main structures reported is shown in Fig. 2.8.

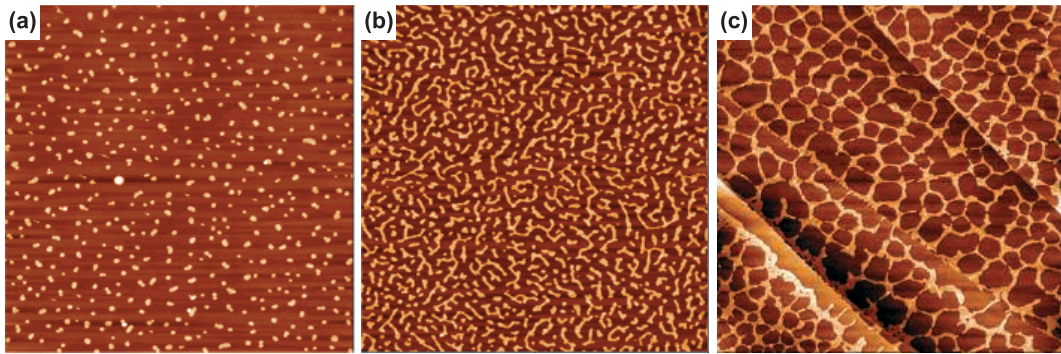


Figure 2.8: Atomic force microscope (AFM) images of CdSe particle structures on highly-oriented pyrolytic graphite (HOPG) with increasing surface coverage (from [85]), showing (a) a $5\mu\text{m}$ image of isolated clusters of particles formed during spin-casting from hexane solution, (b) a $5\mu\text{m}$ image of a broken labyrinthine structure formed during spin-casting from chloroform, and (c) a $10\mu\text{m}$ image of a cellular structure also formed during spin-casting from chloroform. Graphite terraces are visible in (c).

The suggestion made by Ge and Brus is that the structures occur by means of some kind of spinodal phase separation. This proposed mechanism is a result of screening of the vdW interactions between particles in solution. They suggest an unstable region in the phase diagram (similar to Fig. 2.3b) which is reached by a quench of the *reduced temperature* during solvent evaporation. The reduced temperature is a dimensionless quantity that takes into account the interactions between particles, meaning that an increase in concentration

as the solvent evaporates leads to an increase in particle-particle interactions, and is equivalent to a temperature quench on the phase diagram.

In the same year, Maillard et al. reported the formation of rings and polygonal “honeycomb” structures from a variety of different nanoparticle solutions drop-deposited onto TEM grids [86,87] (Fig. 2.9a and b). Fairly conclusively, at least some of these effects were shown to be the result of Bénard-Marangoni convection, similar to the effect shown in Fig. 1.4a. Evaporation during spin-casting leads to both a reduction in temperature and an increase in particle concentration at the upper surface of the film. Measurements made by Stowell & Korgel show how the surface tension of colloidal suspensions can be modified by the temperature and concentration [88]. Areas of convection are therefore set up by surface-tension gradients, and spontaneously self-organise into space-filling polygonal networks. The particles are carried on the convection rolls, and remain in place after the solvent has evaporated (Fig. 2.9c).

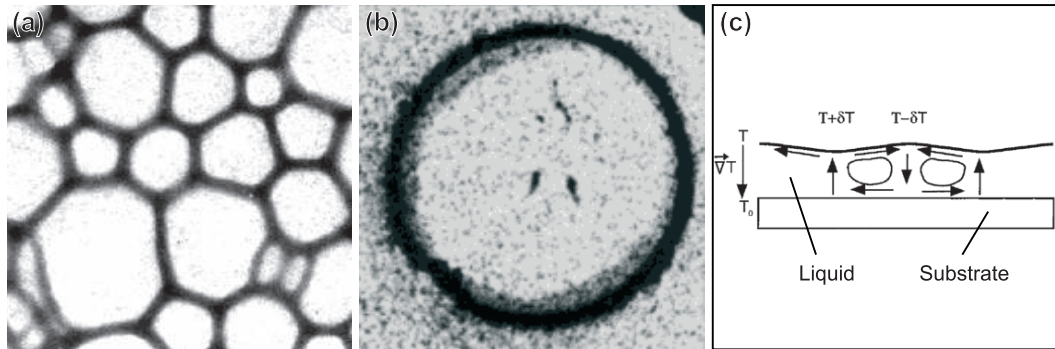


Figure 2.9: The formation of (a) polygonal networks and (b) rings from drop-deposited nanoparticle solutions by surface-tension driven convection (c).

The formation of nanostructured networks from spin-cast thiol-passivated gold nanoparticles was first reported in our research group in 2002 [89,90]. The range of patterns observed was similar to that seen by Ge & Brus, and

four recent examples of structures are shown in Fig. 2.10. In general, these different morphologies can be obtained using different concentrations of solution. In toluene, low nanoparticle concentrations were found to produce isolated aggregates (Fig. 2.10a), and more concentrated solutions tended to produce cellular structures (Fig. 2.10d). At intermediate concentrations, “wormlike” to labyrinthine structures were observed (Fig. 2.10b, c). Interestingly, it was found that cellular structures were not observed at all when hexane was used as the solvent.

The arguments put forward in this paper suggest that convection alone cannot explain the range of patterns observed. Rather, it is suggested that spinodal phase separation (as in [85]) or *viscoelastic* phase separation (a somewhat complex concept described by H. Tanaka [91]) could play a role in the formation of a number of the patterns. The apparent spatial correlations and relative order of the aggregates observed were used as evidence for this: a well-defined preferred wavelength is often considered the “signature” of a spinodal process. A theoretical model for pattern formation in colloidal nanoparticle systems based on spinodal phase separation was presented by Tang, Ge, & Brus in 2002, but this model was unable to account for the formation of cellular structures [92].

Perhaps the most compelling evidence that we do not yet fully understand the mechanisms involved in the formation of these patterns, is the structures that are seen in spin-casting from high concentration solutions. Above the concentrations that produce cellular networks such as that in Fig. 2.10d, cellular networks are observed that exhibit more than one distinct length scale. In this regime, it seems that several mechanisms acting at different length-scales

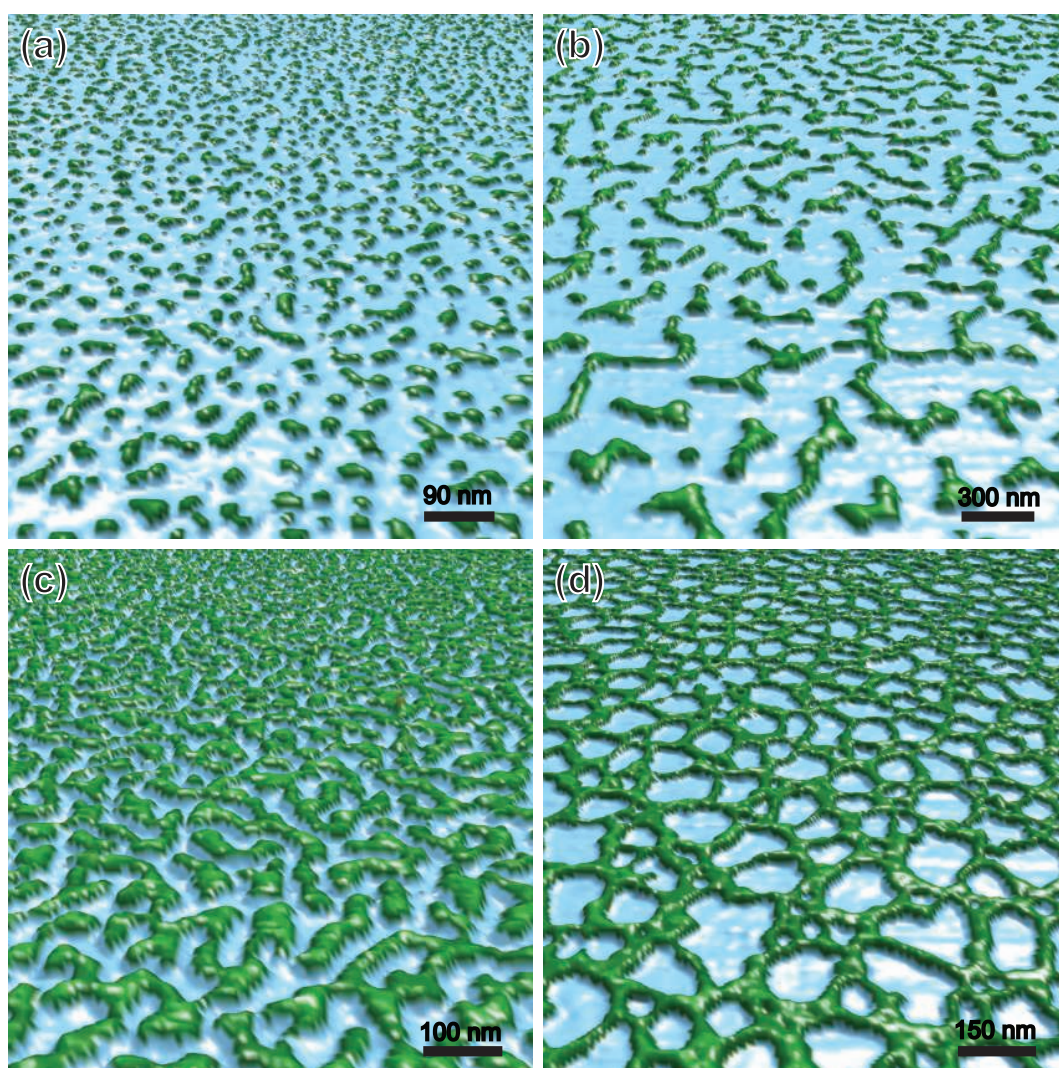


Figure 2.10: Three dimensional projections of the three main morphologies observed in far from equilibrium nanoparticle arrays, showing (a) isolated island clusters of particles, (b) a “worm like” morphology, with isolated twisting ribbons of particles, (c) a labyrinth of particles, and (d) a cellular network.

must be responsible for the formation of the patterns (Fig. 2.11).

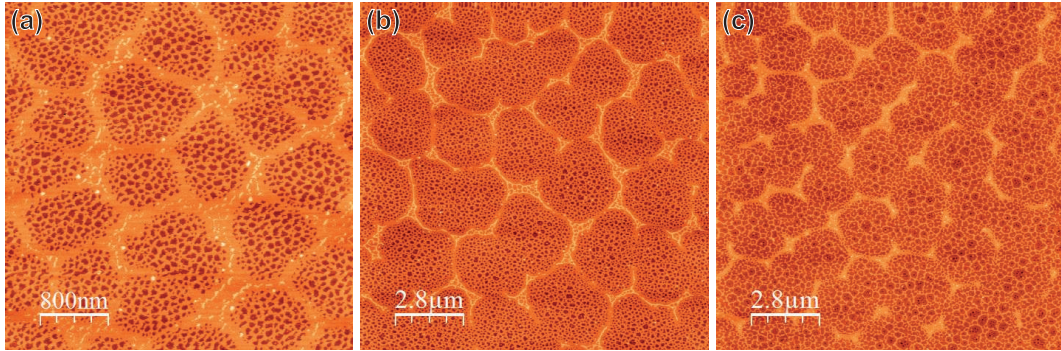


Figure 2.11: AFM images of nanoparticle assemblies displaying multiple length-scale cellular networks (taken by M. O. Blunt), showing (a) two distinct sizes of cellular structure at a thickness of one particle layer, (b) an image similar to (a) except with the formation of a third network structure atop the boundaries of the larger network, and (c) an image similar to (a) except with the formation of smaller holes inside some cells of the small network.

The three main candidates for the pattern formation in nanoparticle systems are: nucleated processes (both thermal and heterogeneous) such as nucleated dewetting or nucleated evaporation; convective processes such as Bénard-Marangoni convection; and spinodal processes (related to the shape of the free energy potential) including spinodal phase separation, spinodal dewetting, and viscoelastic phase separation. Two simultaneous mechanisms (heterogeneous pore nucleation and spinodal dewetting) have been shown to be responsible for the formation of two-level cellular networks in collagen [59]. No such conclusive work has yet been possible for colloidal nanoparticle systems, as the processes involved occur much more rapidly and are not easy to slow down or “freeze” without modifying the system dynamics.

Other notable patterns in gold nanoparticle arrays include aggregates that are highly branched and fractal-like (Fig. 2.12a), and “viscous fingering” holes (Fig. 2.12b). The former is very similar to the structures seen in diffusion-

limited aggregation [93], and the latter is reminiscent of the patterns produced by injecting air into a viscous fluid confined between glass plates [94]. The mechanisms mentioned above are unable to explain these phenomena directly, so they are most likely the result of other side processes effected by the particular nature of the system. Fingered structures have been reported in simulations by Yosef & Rabani [95], and an exploration of this region of the simulated parameter space will be presented in Chapter Five. Experimental investigation into this phenomenon is ongoing in our group, and recent videos obtained by contrast-enhanced microscopy have allowed real-time observation of the formation of viscous fingers in nanoparticle solutions [96].

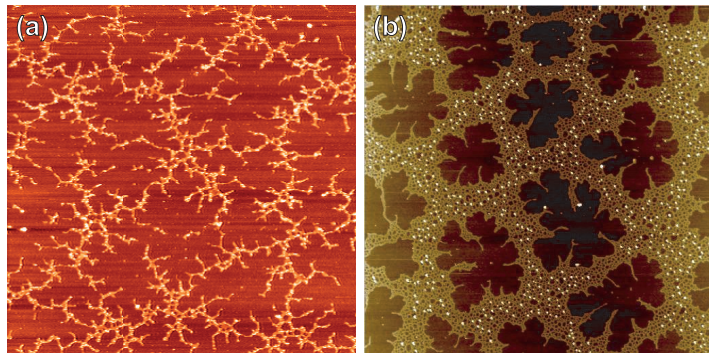


Figure 2.12: Two patterns that are sometimes observed in nanoparticle systems: (a) fractal aggregates, reminiscent of diffusion limited aggregation [93], and (b) “viscous fingering” holes [94].

In 2003, Rabani et al. published a paper describing a Monte Carlo simulation model [1], which seems able to reproduce a large number of the structures seen in the experiments of Ge & Brus [85], and is also highly applicable to experiments with thiol-passivated gold nanoparticles. This model is central to the work in this thesis, and will be described in detail in Chapter Three.

2.4 Conclusions

This chapter has examined a variety of patterns that seem to recur in a diverse range of systems in nature, and discussed some of the mechanisms involved in the formation of these patterns in different systems. A detailed discussion of dewetting in thin films was included due to its potential importance in the formation of patterns in nanoparticle arrays. A number of mechanisms have been proposed for the formation of nanoparticle patterns, but there is as yet no complete understanding of processes involved. Distinguishing between mechanisms is not a simple task, as direct observation of the pattern formation processes is extremely difficult. However, an understanding can be gleaned by examining in detail the morphology of the patterns seen by AFM.

The next chapter will describe in detail a variety of experimental and simulation-based methods for understanding nanoparticle pattern formation. Chapter Four will then focus on the important task of quantitatively examining the morphology of two-dimensional structures, in order to compare and classify the different patterns that are observed. By these means, significant progress has been made towards understanding exactly what happens during spin-casting of nanoparticle solutions.

Chapter 3

Simulations and Experiments

“There are two possible outcomes: if the result confirms the hypothesis, then you’ve made a measurement. If the result is contrary to the hypothesis, then you’ve made a discovery.”

Enrico Fermi (1901–1954)

This chapter will describe some of the techniques— both experimental and theoretical— that will be used in later chapters. The principles of Monte Carlo simulation are covered in some detail, and a simulation technique which reproduces many of the features of drying-mediated nanoparticle self-organisation is described. Also covered are the principles of atomic force microscopy as both an imaging method and a lithographic tool, the real-time observation of spin-casting, and the measurement of contact angles.

3.1 Monte Carlo simulation

3.1.1 Background

It is a regrettable fact that war is often the driving force behind technological development. With the Second World War came the push for ever more complex computations of the properties of both conventional explosives, and thermonuclear weapons. The first electronic computer (the “electronic numerical integrator and computer”, or the ENIAC) was designed to solve the vast number of relatively simple routine calculations needed to develop the atomic bomb. In spite of the hundreds of thousands of deaths resulting from this work, the power of the ENIAC was later turned to the less aggressive task of solving statistical problems in physics [97].

There are several ways in which to approach the modelling of physical problems. Using the example of massive bodies under the influence of gravity, the most accurate approach is to precisely consider the interactions of each individual body with all others in the system. The motion of each body can then be plotted by solving a set of differential equations. The drawback of this technique is its complexity. It is inherently an order N^2 process— that is to say, a system of N bodies will require N^2 particle-particle interactions to be taken into account. As a result, the computational power required for this method becomes very large even in the case of a few hundred objects. Hence this technique is best suited to systems involving only a relatively small number of interacting objects.

For very large ensembles of particles, in the 19th century James Clerk Maxwell developed the *kinetic theory of gases*, which formed the foundations

of statistical mechanics. Statistical mechanics is a tool by which the bulk properties of a substance (e.g. a gas) can be described by making a number of assumptions about the individual components of that substance. In the case of Maxwell's theory, the assumptions can be summarised as follows: a gas is composed of a large number of identical, well-separated molecules undergoing purely elastic collisions, and heat can be defined as the transfer of kinetic energy between molecules. With the application of probability theory, this set of assumptions provides an extremely useful way to relate the molecular properties of a substance to the average properties of a bulk material.

For problems of an intermediate size, however, continuum models provide too high a level of computational complexity, yet statistical mechanics is only able to describe the mean properties of a system, and not its qualitative dynamics. This gap in modelling methods is comfortably filled by Monte Carlo simulation: a technique appropriately named after the casino complex in the Monte Carlo quarter of Monaco. The name was suggested by Nicholas Metropolis because of the stochastic nature of the Monte Carlo method; every Monte Carlo algorithm has its roots in random numbers[†], much like a game played with a shuffled deck of cards.

3.1.2 The Monte Carlo method

The Monte Carlo method is perhaps best described using a highly appropriate example provided by Metropolis & Ulam: determining the probability of success in the card game solitaire [98]. To calculate the exact probability of

[†]More accurately, the numbers are generally *pseudo*-random, meaning they have been generated from a deterministic algorithm that produces sequences of numbers having similar characteristics to truly random numbers.

winning is a task of some considerable complexity. However, a simple method of obtaining an approximation of the probability is to play many games using well-shuffled decks of cards, and note the outcome of each game. As the sample size becomes larger, the approximation of probability will become more accurate, until the answer is correct within a desired tolerance. The repetitive nature of this task makes it extremely well suited to calculation using a computer.

It is possible to apply the same principle to much more complex problems. For example, Brownian motion is the random walk performed by a relatively large particle in a liquid as a result of its constantly being buffeted by the motion of the liquid molecules. It would be possible to simulate this directly by following all the collisions of the molecules in the liquid— both with each other and with the larger particles— and then tracking the motion of the larger particles. This would of course involve keeping track of several thousand molecules even in a relatively small simulation. If all we are interested in is the motion of the larger particles, it is much less computationally expensive to simulate the *effect* of the molecular buffeting.

The following approximation is useful in the design of a Monte Carlo simulation of Brownian motion. A particle undergoing Brownian motion will continue in a straight line at a constant velocity until its path is interrupted by the action of molecules in the liquid. At this point, its velocity vector will be adjusted, changing both speed and direction. It will then continue at the new velocity until the next event that causes it to change. Associated with this process are two quantities which can form the basis of a Monte Carlo simulation: there is a finite probability of a given particle undergoing a change of

velocity in a given small time interval Δt , and the particles in the system will have a well-defined distribution of velocities (e.g. a normal distribution).

Starting with an initial random configuration of particles at time t_0 , it is possible to move to the state of the particles at $(t_0 + \Delta t)$ by considering the probability of velocity change (p_{vc}) in that interval in relation to a random number between 0 and 1 (η). If a particle does change momentum (if $\eta < p_{vc}$), its new velocity is chosen at random according to the known distribution of velocities, and its position is updated accordingly. The process is repeated for all particles, and for many time steps. If Δt is small enough, then a good approximation to the behaviour of the particles can be obtained. This is the basis of the Monte Carlo method.

3.1.3 The Ising model

In 1925 Ernst Ising proposed a model to describe the behaviour of ferromagnetic systems [99]. This model is based on spin vectors (σ_i) arranged in a square lattice (i), which can have a value of either +1 or -1. Ising proposed that adjacent spins should have an energy associated with the “bond” between them, such that opposing adjacent spins have an energy “cost” ($+J$) and parallel spins are energetically favourable ($-J$). The total energy of the system can thus be found by summing across the lattice, and is represented by the Hamiltonian

$$E = -\frac{J}{2} \sum_{(i,j)} \sigma_i \sigma_j. \quad (3.1)$$

Assuming a Maxwell-Boltzmann distribution of energies, at a temperature T , the probability of a particular configuration of spins e with energy $E(e)$ will

be proportional to the Boltzmann factor

$$P(e) \propto \exp\left(\frac{-E(e)}{k_B T}\right), \quad (3.2)$$

and the exact probability of a given configuration can be calculated by normalising with the partition function Z , where $Z = \sum_e P(e)$.

In two dimensions, this model exhibits a phase transition from disordered spins above a critical temperature T_c to ordered spins of the same alignment below T_c . As such, this is a very successful model of ferromagnetism, especially considering its simplicity. Although the two-dimensional Ising model was solved analytically at the critical temperature by Lars Onsager in 1944, the solution is far from simple and spans more than thirty mathematically dense pages [100]. Furthermore, in three dimensions such a solution has yet to be found. For this reason, the system lends itself well to study by the Monte Carlo method. The Metropolis algorithm is an excellent tool to this end.

3.1.4 The Metropolis algorithm

Nicholas Metropolis proposed a method for evaluating equations of state using “fast computing machines” in 1953 [101]. His algorithm is a particular variation on the Monte Carlo method which represents a simple way to evolve a system towards its equilibrium state. Described in terms of the Ising model, the Metropolis algorithm proceeds according to the following steps:

1. A spin site is selected at random, and provisionally inverted, taking the system from state e_1 to state e_2 .

2. The energy difference $\Delta E = E(e_2) - E(e_1)$ is evaluated, and if the inversion is found to be energetically favourable ($\Delta E < 0$), then it is retained.
3. If $\Delta E > 0$, a random number (η) is generated, and if $\eta < \exp(-\Delta E/k_B T)$ then the spin flip is accepted, if $\eta > \exp(-\Delta E/k_B T)$ then the spin is flipped back to its original state.

The whole process is then repeated, until the system reaches equilibrium. Three structures produced by the method described above are shown in Fig. 3.1.

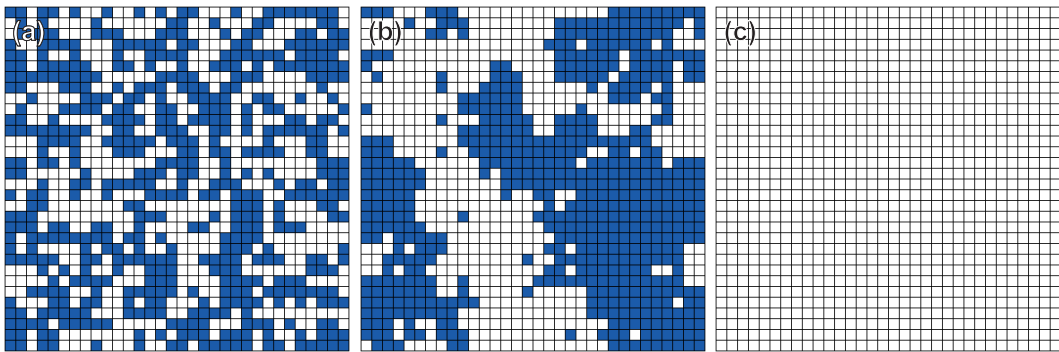


Figure 3.1: The equilibrium state of the Ising model (spin +1 is blue, -1 is white) calculated by a Metropolis algorithm at different temperatures showing the system (a) well above the critical temperature, with no overall magnetisation, (b) exactly at the critical temperature, with slowly fluctuating domains of each spin, and (c) below the critical temperature where one spin direction fills the whole lattice.

Comparing the Boltzmann factor to a random number creates an approximation to the Maxwell-Boltzmann energy distribution, and is a simple way to determine the probability of a spin having enough energy to reach state e_2 . It is derived from an integration of the Maxwell-Boltzmann probability distribution from $E = \Delta E$ to $E = \infty$. It is important to note, however, that using the Boltzmann factor does not take into account any energy barrier that

may be associated with a transition, only the difference in the energies of the two states. If the energy difference is not a good approximation for the magnitude of the activation barriers, a simulation may not display the true dynamic behaviour of the system. Nonetheless, it is possible to simulate many different systems with an Ising model using the Metropolis algorithm. In addition to ferromagnetism, the model works well when applied to binary mixtures such as alloys or polymer blends. More relevant to nanoparticle self-organisation, however, is the fact that this method can also be used to simulate the evaporation of a liquid.

3.2 Nanoparticle simulations

3.2.1 The Rabani et al. model

In 2003, Rabani et al. published a paper describing a Monte Carlo simulation technique that appeared to reproduce many of the features seen in far from equilibrium nanoparticle experiments [1]. The model is based on the interplay between the solvent evaporation and the random walks of nanoparticles. The algorithm controlling the behaviour of the solvent is essentially a modified Ising model, with liquid and vapour in place of the two spin states in the magnetic case. In addition, randomly walking nanoparticles are included within this two-dimensional lattice gas.

Although complicated by the inclusion of nanoparticles, the basic model is very similar to the Ising model described above. Each cell of a square lattice, i , may contain either liquid ($L_i = 1$), vapour ($L_i = 0$), or nanoparticle ($n_i = 1$), and the presence of a nanoparticle excludes the presence of solvent. As a

starting point, a single lattice site is said to represent a square of side 1nm, and the particles are represented by squares of side 3nm (although it should be noted that these are not rigid definitions, merely suggestions based on the system being modelled: within an order of magnitude or so, length scale is not critical).

To perform the simulation, each solvent cell is examined, and an attempt is made to convert the cell from liquid to vapour (or vice-versa) with a Metropolis acceptance probability $p_{acc} = \min[1, \exp(-\Delta E/k_B T)]$, where ΔE is the change in energy that would result from such a conversion, as described earlier. This energy change is calculated from the interaction energies between adjacent cells. The total energy of the system can be represented by the Hamiltonian

$$E = -\epsilon_l \sum_{\langle ij \rangle} l_i l_j - \epsilon_n \sum_{\langle ij \rangle} n_i n_j - \epsilon_{nl} \sum_{\langle ij \rangle} n_i l_j - \mu \sum_i l_i, \quad (3.3)$$

where ϵ_l , ϵ_n , and ϵ_{nl} are the interaction energies between two adjacent sites that are occupied by solvent, nanoparticle, or solvent and nanoparticle, respectively. As discussed by Rabani et al., the value of μ (the chemical potential) determines the mean equilibrium density of solvent on the surface. It represents the free energy difference between the liquid and vapour phases of the solvent. It can be thought of as an effective parameter representing any interaction energy that is not explicitly taken into account by the other parameters (for example, the interaction of the solvent with the substrate, which shall be discussed in Chapter Five). The behaviour of the model is also controlled by the temperature of the system, T , and the fractional coverage of nanoparticles.

As the solvent is evaporating, the nanoparticles perform a random walk

on the lattice, and are only able to move into “wet” areas of the substrate (i.e. into areas containing three liquid cells). This restriction mimics the low mobility of nanoparticles on the substrate in the absence of solvent, and is vital for the coupling between the particles and the evaporating solvent. As a particle moves, the three liquid cells that were in front of it are replaced in its wake. This ensures particle motion does not affect the liquid solvent density.

The random walk of each particle is controlled by the Metropolis algorithm in a similar way to the solvent evaporation. Each particle is examined in turn, and a random direction is chosen for motion (up, down, left, or right). The energy change that would result from a move of one lattice site in that direction is calculated, and if it is energetically favourable, the move is performed. If the move would require the input of energy, the Boltzmann factor is compared with a random number and the move is carried out, or not, according to the result of the comparison. The effective mobility of the particles is controlled by the number of times each particle is examined in one solvent cycle. This ratio of particle steps to solvent steps, the *mobility ratio* (MR), has useful values between approximately 5 and 100.

The simulation is subject to circular boundary conditions, such that if a particle wanders off one side of the lattice, it will return from the opposing side. Interestingly, in two dimensions on a square lattice, this gives the simulation the non-Euclidean geometry of a toroidal surface. Although this can become significant when there is only a small number of lattice points, for large lattices circular boundaries allow for the elimination of edge effects without the introduction of geometry-related artefacts. A flow diagram describing the details of the simulation is shown in Fig. 3.2, and a pictorial representation of a section

of simulation lattice is shown in Fig. 3.3a, illustrating the colours that will be used in simulation images throughout this work.

3.2.2 Anisotropy modification

My simulations differ from those of Rabani et al., in that not only nearest but also next-nearest neighbours are taken into account when calculating the energy change associated with a particular solvent transition. This modification was necessary to compensate for anisotropy observed in the limit of slow, nucleation-driven evaporation. Without the inclusion of next-nearest neighbour interactions, vapour “bubbles” tend to form as squares with their sides aligned to the lattice (as shown in figure 3.4). This is simply because a solvent cell on a liquid-vapour interface that is diagonal (at 45° to the square lattice) has two liquid nearest neighbours, rather than three in the case of a horizontal or vertical interface. Hence diagonal interfaces are less stable, and tend to retreat rapidly until they form the corner of a square. This is clearly an unnatural state of affairs, as in reality the solvent is an isotropic medium, which should result in vapour bubbles that are approximately circular.

To implement this modification, the first and third terms of equation 3.3 are calculated over eight neighbours when examining the solvent, and the next-nearest neighbours are given a weighting of $1/\sqrt{2}$, as compared to unit weighting for the nearest neighbours. A re-normalisation factor was also introduced for these terms, so that the same parameters could be used as in the nearest neighbour model, and the results compared directly. This was manually determined to be 0.562 by matching the nucleation rate in the thermal nucleation regime.

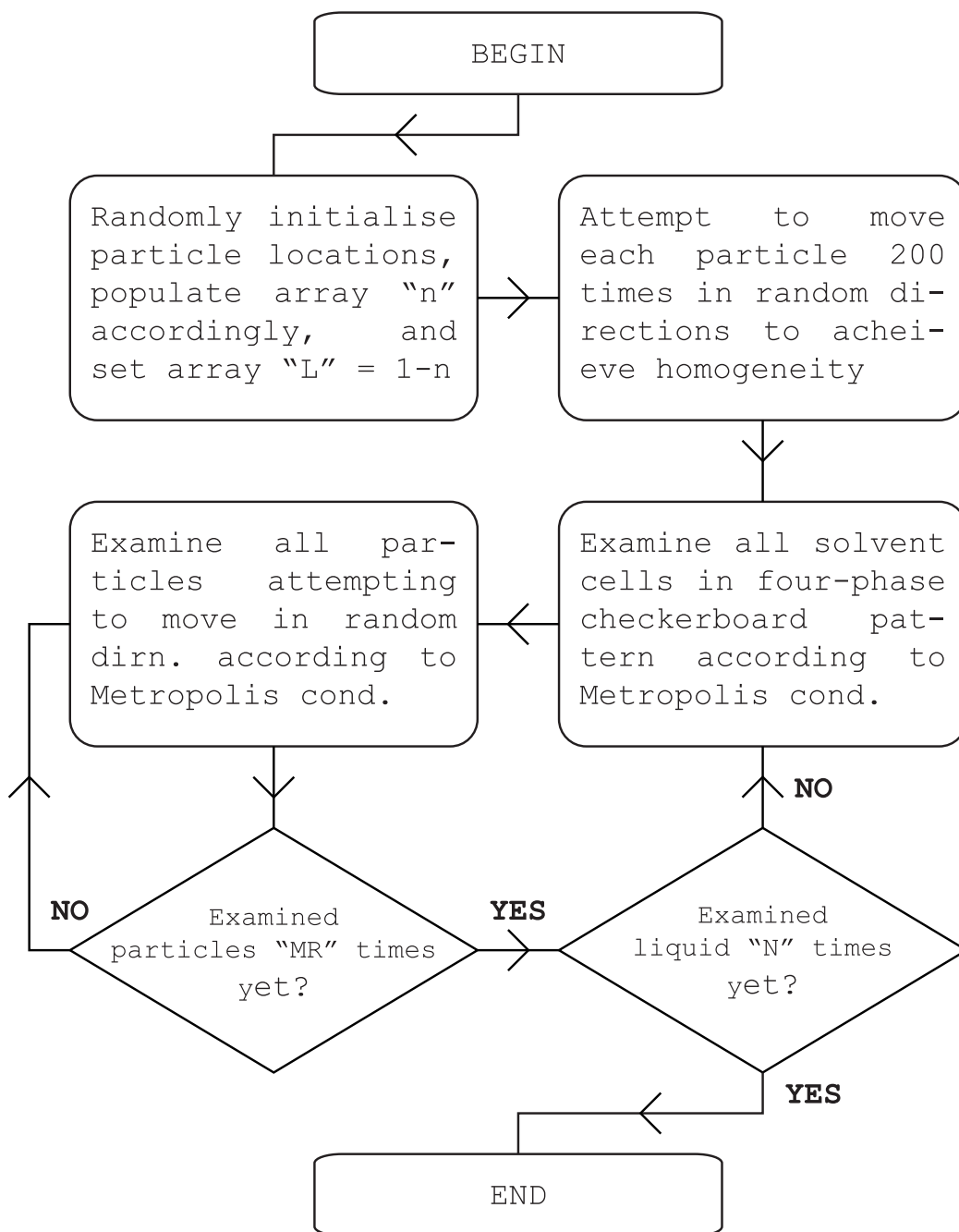


Figure 3.2: Schematic flow diagram illustrating how the Rabani model simulation proceeds.

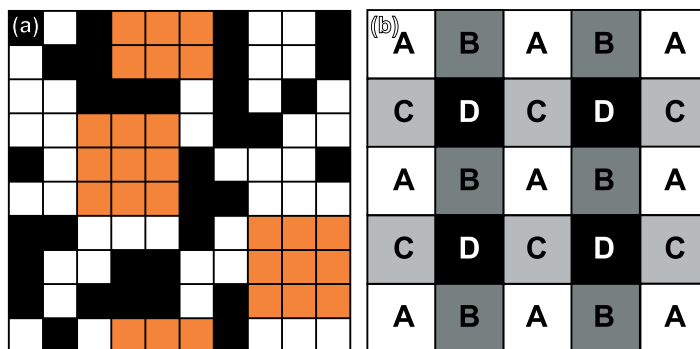


Figure 3.3: Panel (a) shows a pictorial representation of the Rabani model simulation, showing liquid solvent in white, solvent vapour in black, and nanoparticles in orange. The particle in the bottom right is able to move up or down, but not to the left where the substrate is not completely wet. Panel (b) shows an illustration of the four-phase checkerboard pattern that is used in the examination of the solvent (see section 3.2.3).

3.2.3 The four-phase checkerboard

It should be noted that the evaporation of the solvent is carried out in a four-phase “checkerboard” pattern (see figure 3.3b, in which each phase is labelled with a different letter and shade). This is necessary to prevent the interactions of neighbouring cells leading to anisotropy according to the order in which the cells are examined. Cells in a single phase of the checkerboard are not affected by the evaporation or condensation of each other, and so can be examined sequentially. If the whole lattice were to be examined sequentially, the order in which this was done would affect the result. The apparent non-randomness of the examination does not therefore influence the dynamics of solvent evaporation. The alternative to the four-phase checkerboard is completely random selection of solvent cells, which would be more computationally intensive, and provide no significant advantage. This idea was implemented by Rabani et al. in their simulations, but with only two phases, as the code did not include

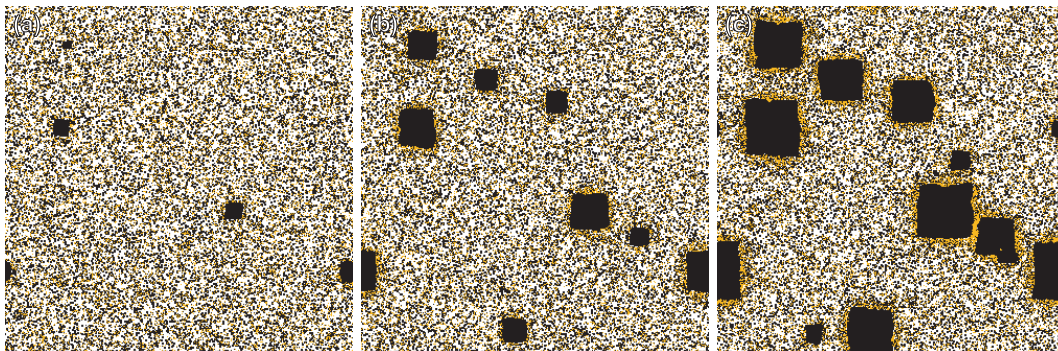


Figure 3.4: Three frames from a 1000x1000 simulation in the thermal nucleation regime without the inclusion of next-nearest neighbour interactions. The vapour bubbles are clearly square even after only 101 MC steps (a). The square bias has continued up to 201 MC steps (b), and after 301 MC steps even the collision of two vapour bubbles still leaves reasonably linear sides (c).

the interaction of next-nearest neighbours [102].

3.2.4 Example morphologies

Fig. 3.5 shows four examples from the wide parameter space associated with these simulations. Panel (a) shows the result of rapid evaporation, and exhibits a labyrinthine structure reminiscent of spinodal processes. Panels (c)-(d) all show cellular structures, but with significantly different morphologies. The classic cellular network in 3.5b, which is formed by thermal nucleation in a regime of slow evaporation, can be modified by increasing the particle coverage to resemble a “wet foam” [28] as shown in 3.5c. Panel (d) is an interesting example of “viscous fingering” in a cellular network. The appearance of “fingers” perpendicular to the retreating solvent front is brought about by reducing the particle mobility (which is akin to increasing the viscosity). These patterns are very similar to those in Fig. 2.12a, and are again reminiscent of those formed in a Hele-Shaw cell [94]. The range of structures that can be produced

by this type of simulation is very large, and these images represent just a small selection. Numerous specific structures will be discussed in more detail in the coming chapters.

3.2.5 The simulation code

Prototypes of the simulations were originally written in “Matlab”, due to its excellent range of built-in functions. However, Matlab is not designed for large-scale Monte Carlo simulation, and its large usage of memory and inefficient execution of code in loops meant that it was deemed productive to convert the code into “C”. Although initially time-consuming, this was indeed found to be extremely worthwhile, and led to a *70-fold* increase in speed when executed on the same computer in a Microsoft Windows environment. The acquisition of a Linux-based high-performance computing (HPC) facility by the University meant that converting the code to run in Linux would be advantageous, and this was carried out by our collaborator Ioan Vancea, in the Max-Planck-Institut für Physik komplexer Systeme in Dresden, Germany.

The code is now best suited to compilation and execution in Linux, and in this environment further speed advantages are obtained. In addition, the HPC facility allows many instances of the code to be executed simultaneously with different parameters. This enables relatively rapid exploration of the parameter space. This code is available on the Internet at <http://thesis.cpmartin.net/> where I shall endeavour to maintain it, along with other resources related to this work, as long as I am able.

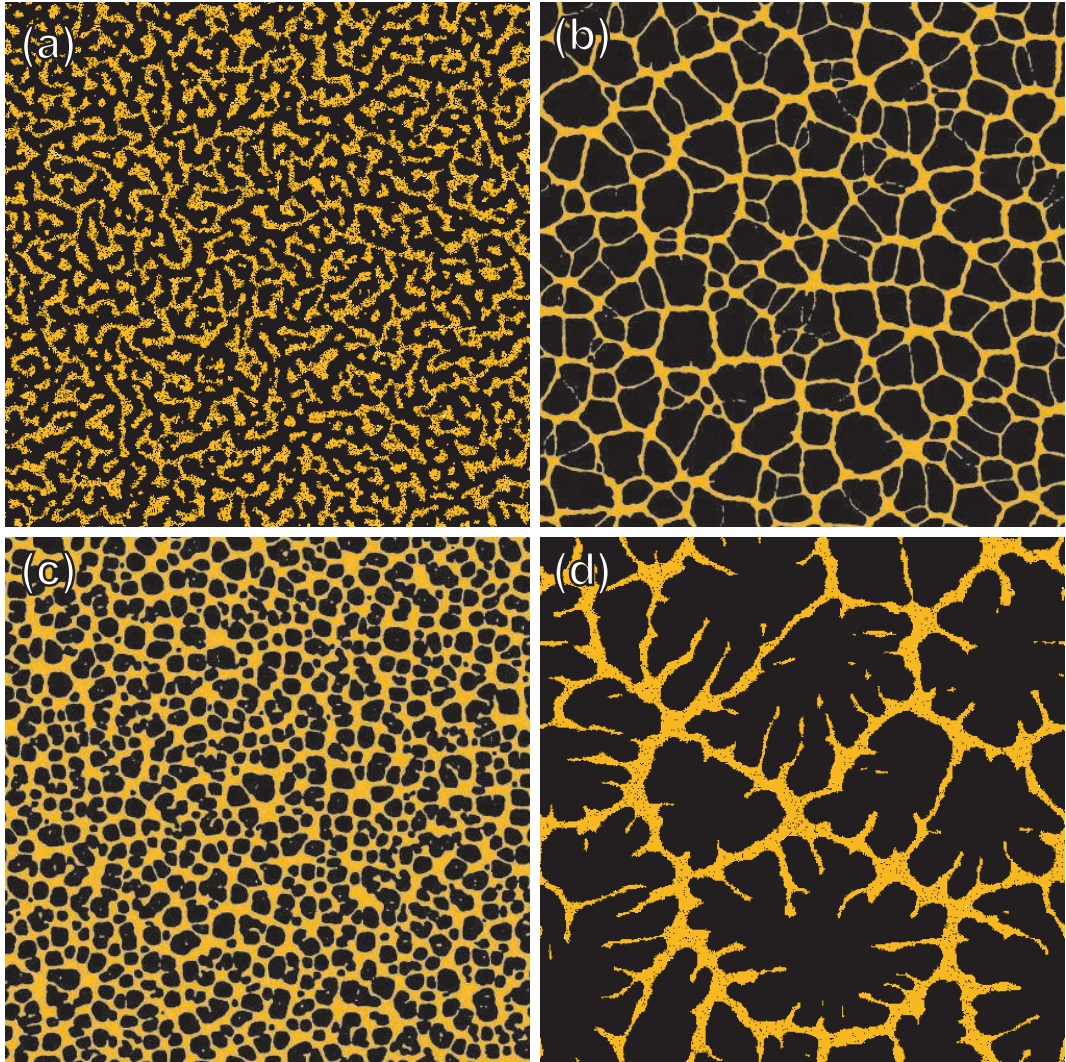


Figure 3.5: Some sample morphologies obtained from simulations, showing (a) a 1008×1008 lattice with $k_B T = \epsilon_l/2$, $\epsilon_n = 2\epsilon_l$, $\epsilon_{nl} = 1.5\epsilon_l$, $\mu = -2.25\epsilon_l$, $MR=30$, and a coverage of 30% after 69 MC steps, (b) a 4008×4008 lattice with $k_B T = \epsilon_l/4$, $MR=30$, coverage 20% after 1003 MC steps, (c) a 3000×3000 lattice with $k_B T = \epsilon_l/2$, $MR=50$, coverage 35%, after 399 MC steps, and (d) a 1008×1008 lattice with $k_B T = \epsilon_l/4$, $MR=10$, coverage 20% after 1003 MC steps.

3.3 Atomic force microscopy

The atomic force microscope (AFM) was invented by Binnig, Quate, and Gerber in 1986 as a modification to the STM that was capable of imaging non-conductive samples [103]. Almost all the experimental images in this work were obtained using AFM (for example those in Fig. 2.10), and the work in Chapter Five is based on a lithographic technique employing AFM. This section will describe the principles of AFM, and the lithographic technique that is employed in Chapter Five.

3.3.1 Basic principles

Contact mode

The basic operation principle of AFM is similar to that of STM, except that the feedback is provided by different means. In STM, the magnitude of the tunnelling current between the sample and an atomically sharp tip is used to determine the distance of the tip from the sample. This signal is used to keep the tip at a constant separation from the surface through feedback circuitry. In the simplest version of AFM, a nanoscopically sharp tip is attached to the end of a cantilever, which is placed into contact with the surface of the sample. The deflection of the cantilever is proportional to the force applied to it by the surface. Measurement of this deflection therefore provides a signal that can be used as feedback to keep the tip at a constant applied force. Cantilevers are commonly made from silicon or silicon nitride, and a typical AFM cantilever is shown in Fig. 3.6.

The most common method of detecting the deflection of the cantilever is

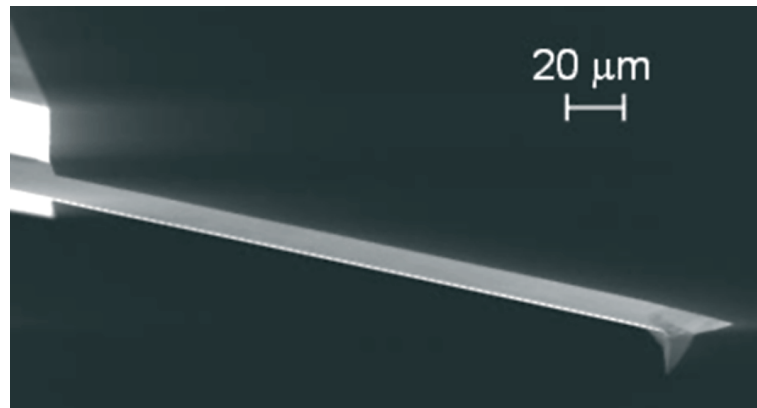


Figure 3.6: A scanning electron micrograph of an AFM cantilever, showing the tip in the bottom right.

by focusing a laser onto its upper surface, and monitoring the position of the reflected beam, which is directed to the centre of a segmented photodetector. The difference in intensity received by different sections of the photodetector indicates the forces that are acting on the cantilever. In this mode, the vertical deflection is monitored, and the sample is scanned in the x and y directions beneath the tip by means of two piezoelectric actuators. A fixed *set point* of force can be maintained by controlling the voltage applied to a third (z) actuator using the feedback from the photodetector. The voltage applied to this actuator is proportional to the height of the surface in contact with the tip, and this can be recorded line-by-line to build an image of the surface topography. This is known as *contact mode*, and a schematic of this mode of operation is shown in Fig. 3.7.

One drawback of imaging in contact mode is the relatively strong interactions that exist between the tip and the sample during scanning. Hard, non-deformable substances such as silicon can be imaged well in this mode, but softer material such as biological samples, or mobile objects on surfaces

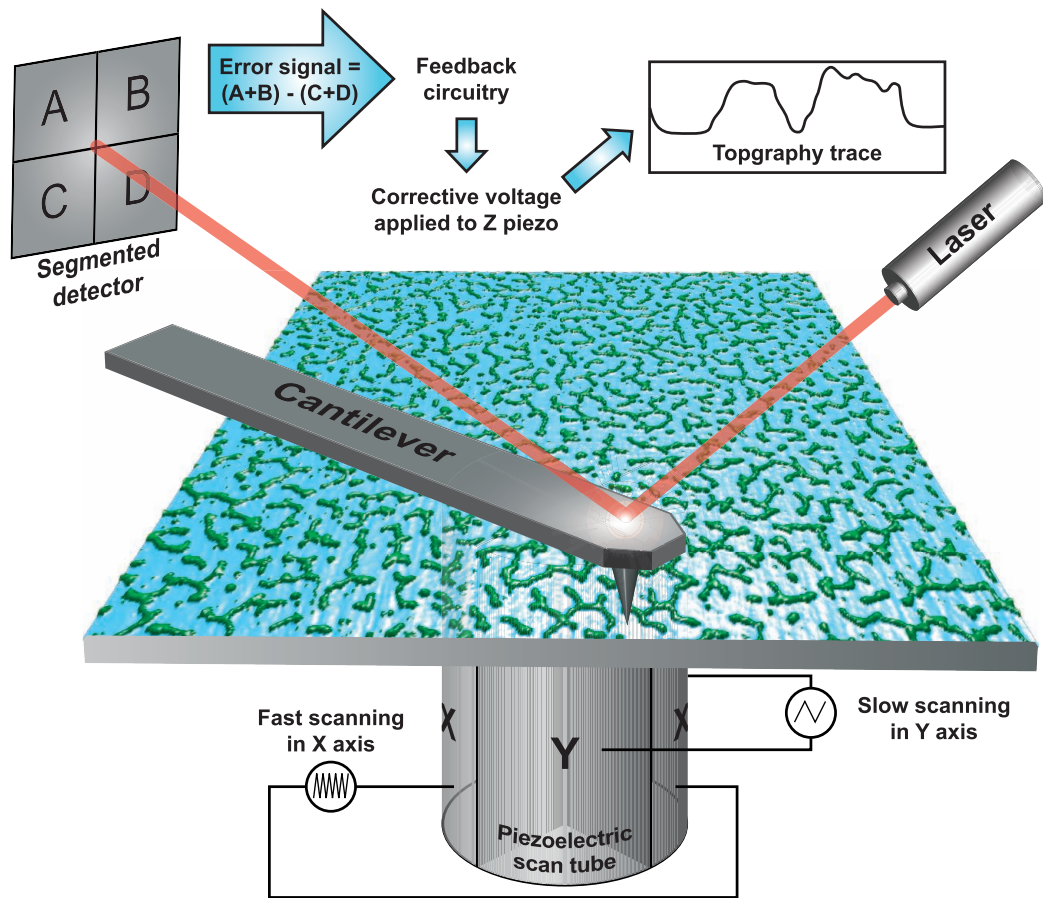


Figure 3.7: The basic operation of an atomic force microscope (AFM) in contact mode.

such as nanoparticles, will be damaged or moved by the scanning action of the tip. For this reason, a different mode was used for imaging nanoparticle samples in this work.

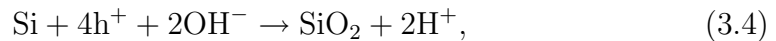
Intermittent contact mode

“Intermittent contact mode”, also known as “tapping mode” or “AC mode” is a modification to the principle described above, and is particularly suited to imaging softer or more easily damaged samples. In this mode, the cantilever is driven near to its natural oscillation frequency, which is generally several tens or hundreds of kHz. The sample is then raised towards the vibrating tip until it is just within the sweep of the oscillation, and the tip begins to “tap” on the surface. The error signal used for feedback in this mode is the amplitude of the cantilever’s oscillation rather than its deflection. The set point in this case is a fixed amplitude of oscillation, which corresponds to a constant interaction with the surface. All the AFM images in this work were obtained by intermittent contact mode.

The images obtained by AFM can have a resolution good enough to reveal single atoms, but this is strongly dependent on the nature of the tip. Because the image produced is actually a convolution of the surface topology with the shape of the end of the tip itself, atomic resolution requires an atomically sharp tip. Nonetheless, the lateral resolution of AFM with inexpensive commercial cantilevers is routinely a few tens of nanometres. Height resolution depends on the precision of the z -actuator and its associated feedback circuitry, but is commonly better than 1Å.

3.3.2 Lithographic AFM oxidation

It is possible to use a conductive AFM tip (usually coated with platinum-iridium) to draw an arbitrary pattern on the surface of a hydrogen-passivated silicon sample. Hydrogen passivation is the process by which the native layer of oxide is removed from a standard silicon wafer using hydrofluoric acid, and replaced with hydrogen groups. This makes the sample conductive, and local re-growth of the oxide can be induced by applying a voltage between the tip and the sample in a humid environment [104, 105]. The oxygen required for this process is obtained from a meniscus of water that forms between the tip and sample when the humidity is high enough. Avouris et al. proposed [106] that the reaction is initiated by the concentrated electric field in the region beneath the tip, and proceeds thus:



where h^+ represents an electron hole. A schematic of the process is shown in Fig. 3.8.

Lithographic AFM oxidation is able to produce lines of oxide that are as thin as 10nm, and are up to 3nm high. It has been found that SiO_2 will also form beneath the level of the original substrate, down to a maximum depth of about $2\frac{1}{2}$ nm. This is a technique that allows very local control of the surface topography and chemistry, and has been studied extensively [107]. Such local control of the surface properties is extremely useful in understanding and indeed controlling far from equilibrium nanoparticle pattern formation, as shall be discussed in Chapter Five.

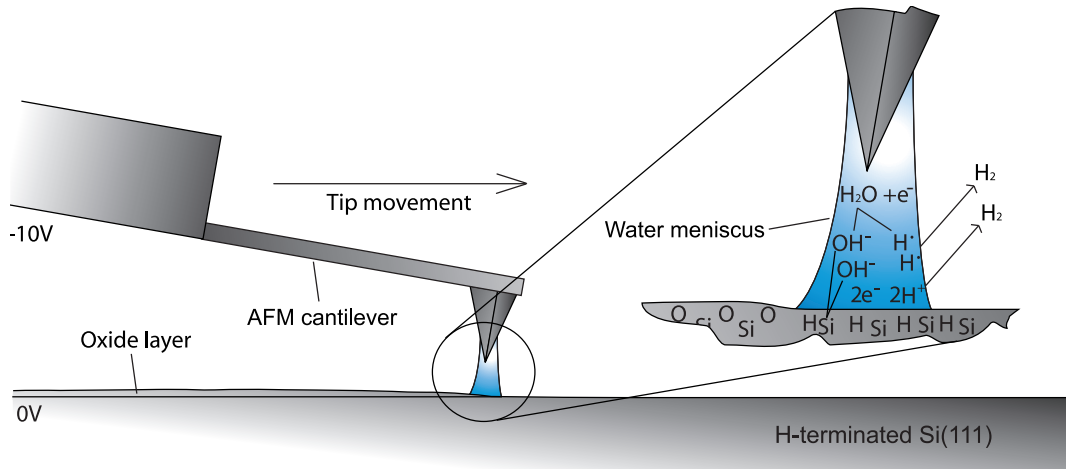


Figure 3.8: A schematic of the lithographic AFM oxidation process.

3.4 Real-time observation of evaporation

It is possible to observe the process of spin-casting a liquid onto a substrate in real-time. Although it is very difficult to observe the real-space nanoscopic dynamics of this process, reflecting a laser from the surface of a substrate during spin-casting allows the observation of a scattering pattern that is a reciprocal-space representation of the structures present on the substrate, albeit with a resolution limited by the wavelength of the laser and the scattering angle. Moreover, the thickness of the film can be monitored by examining the periodic variation in intensity of the reflected light as a result of constructive and destructive interference occurring between light reflected from the substrate and the surface of the solvent.

Jukes et al. developed such an instrument at Sheffield University [108]. The instrument consists of a spin-coater mounted at the centre of rotation of two large aluminium discs, to which a HeNe laser and light detectors are attached, allowing the angle of each to be adjusted with respect to the substrate. Spec-

ularly reflected light is collected by a silicon photodiode, and scattered light is collected on a screen and recorded using a CCD camera. We had the opportunity to perform some experiments using solutions of thiol-passivated gold nanoparticles with this equipment

3.5 Contact angle measurements

As discussed in section 1.1 the macroscopic contact angle can aid the understanding of the interfacial energy of a liquid on a solid substrate. It is therefore a useful measurement to make for the liquids and the substrates used in these experiments. It would perhaps initially seem trivial to obtain a measure of the contact angle: a drop can be placed on a surface, and observed with a microscope with its optical axis parallel to the substrate. Indeed, for large drops of non-wetting liquids of low volatility, this method is quite accurate. However, the solvents used in our nanoparticle experiments (mostly toluene, hexane, or chloroform) are extremely volatile, and are macroscopically almost completely wetting on both native-oxide and hydrogen-passivated silicon. These facts make measuring the contact angles of these systems somewhat challenging.

As a drop of volatile liquid evaporates, its contact angle will be reduced because of viscous drag at the retreating edge of the drop. A piece of apparatus available to us in the School of Pharmacy at the University is capable of monitoring the contact angle of a very small drop of liquid during evaporation, and extrapolating back to obtain the static contact angle. A number of experiments were performed using this apparatus. It should be noted, however, that the error in these measurements is large: as much as $\pm 10^\circ$ in some

cases. Furthermore, it is worth re-iterating that the macroscopic contact angle is not necessarily indicative of the nanoscopic wetting behaviour, and it does not describe the complete interface potential.

3.6 Summary

This chapter has described the experiments and simulations which will form the basis of the work in the coming chapters. The next chapter will discuss some of the results of the simulations, and their implications for the formation mechanisms of nanoparticle structures. Chapter Five will bring together these simulations and experimental techniques to gain a greater understanding of the formation mechanisms.

Chapter 4

Nanoparticle Networks: Self-organised or Disorganised?

“I have had my results for a long time: but I do not yet know how I am to arrive at them.”

Karl Friedrich Gauss (1777–1855)

This chapter will describe techniques for the analysis and comparison of two-dimensional structures, and examine results both from experimental images, and from simulated structures. Particular attention is paid to the deviations from random statistics exhibited by structures formed through dewetting and evaporation, and the mechanisms behind these deviations. The work in this chapter is based on the statistical analyses I performed in [109] and [110].

4.1 Pattern analysis and comparison

The myriad patterns that are generated by nanoparticle solutions can be divided into basic groups according to their morphology. Arguably, there are just three major non-equilibrium structures: isolated islands, labyrinths, and cellular networks; other patterns can be considered variations or combinations of these three. For example, worm-like structures could be considered an intermediate stage between islands and labyrinths. In truth, this example provides evidence that the range of patterns is actually more of a continuum, and the specific variations on these three themes can provide details of the processes involved in their formation.

Before it is possible to understand the origin of a particular structure, it is important to be able to describe its morphology not just qualitatively, but also *quantitatively*. Being able to quantify the particular subtle variations on the theme of a pattern can give significant clues as to the mechanisms that dominate the pattern formation process. This section presents an overview of some techniques that can be used to numerically classify and hence to compare nanoparticle structures.

4.1.1 The fast Fourier transform

One of the simplest pieces of information that can be gleaned from an image is the size of the features it exhibits. A simple way to examine the spatial frequencies present in an image is to examine its inverse-space counterpart in the form of a discrete Fourier transform. The two-dimensional fast Fourier transform (2DFFT) is an efficient algorithm for obtaining a discrete Fourier

transform of an image. If the image contains a dominant spatial frequency (i.e. has many features of a similar spacing), this will be shown by a ring in the 2DFFT. A good way to highlight such a ring is to perform a radial average of the 2DFFT. The ring will then appear as a peak in a wavevector spectrum, which can be used to find the dominant feature wavelength.

The presence of a preferred wavelength in a system is often cited as the signature of a spinodal process (e.g. [52]). This is because such processes inherently select a particular wavelength by the competition between long- and short-range processes, as discussed in Chapter Two. However, this assumption relies on the principle that other processes (e.g. nucleated processes) do not lead to the existence of a preferred feature size. This shall be discussed later in this chapter.

4.1.2 The Voronoi tessellation

There are a number of structures that can be represented by a set of point co-ordinates, such as isolated small islands and cellular networks. A tool that can be used for the analysis and comparison of such structures is the *Voronoi tessellation*. In the case of a cellular network, the Voronoi tessellation is constructed by first locating the point which is the centroid of each cell, and then drawing the perpendicular bisector of the lines that join each point to its immediate neighbours. In this way, an area is defined which is closer to that point than any other, and the whole of the space is filled with such areas. This is identical to the manner in which the Wigner-Seitz unit cell is constructed in solid state physics. Fig. 4.1b shows a Voronoi tessellation of the network in 4.1a. Note in this case that the whole area is not covered with cells, as the

edge cells would have vertices at infinity resulting from the unknown locations of their neighbours.

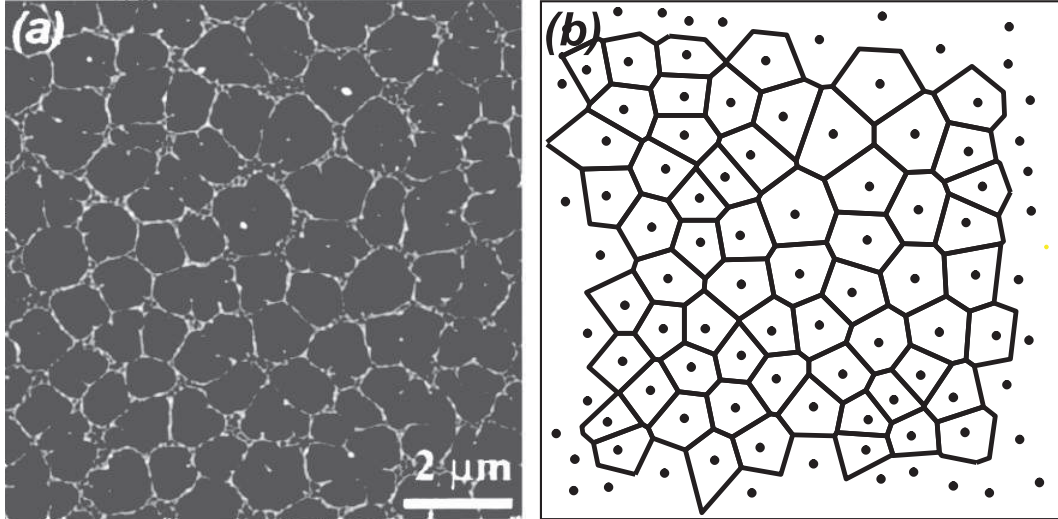


Figure 4.1: (a) A typical Atomic Force Microscope (AFM) image of a cellular network obtained from spin-casting Au nanoclusters in toluene onto a Si substrate [89], and (b) the same network reduced to a Voronoi tessellation.

Further information about the morphology of a network can be gleaned from numerical analysis of the Voronoi tessellation. A plot of the probability of finding a cell with a given number of sides, $p(n)$, can qualitatively reveal the degree of order or disorder of a structure. A Voronoi tessellation from a completely random (Poisson) set of points (known as the random Voronoi tessellation, or RVT) will have an asymmetric $p(n)$ plot with a distinct tail towards higher values of n . Conversely, such a plot from a honeycomb will be highly symmetric, and most likely have only a very small number of cells (if any) with a number of sides other than six. We can describe these observations numerically using two values that are associated with $p(n)$: the first moment about the mean, μ_2 , also known as the *variance* of the distribution; and the

entropy, S . The variance gives us an indication of the uniformity of a structure: the higher the variance, the less uniform the structure. The entropy is defined in a similar way to the entropy in statistical mechanics:

$$S = - \sum p(n) \ln p(n). \quad (4.1)$$

The greater the entropy, the higher the degree of disorder in the structure. The RVT– the archetypal disordered tessellation– is known to have an entropy of 1.71 and a variance of 1.78 [111]. Values lower than these indicate a degree of order greater than that which can be obtained merely by the random selection of co-ordinates.

Whatever the specific morphology, an infinite network in a two-dimensional plane will have a mean number of sides that is defined as $\bar{n} = 6$. This constraint can be derived from Euler’s equation in two dimensions:

$$F - E + V = \chi, \quad (4.2)$$

where F , E , and V are the number of cells (or *faces*), edges, and vertices in a network respectively. The parameter χ is the Euler characteristic of the space in which the network is defined, and this is equal to 1 in a Euclidean plane [31]. In a two-dimensional foam, each vertex is formed by three edges, and each edge is shared between two vertices, so that $V = \frac{2}{3}E$. Substituting this into equation 4.2, we find that in the limit $F \rightarrow \infty$, the relation $\frac{E}{F} = 3$ holds. As each edge is the boundary between exactly two cells, we can say that $\bar{n} = 6$ in an infinite network. In finite systems, however, there may be sampling error deviations from this value of the order $1/N$, where N is the

number of cells in the sample. For example, in Fig. 4.1b, we find that $\bar{n} = 5.89$ from a sample of 63 cells.

4.1.3 Minkowski Morphometry

The Minkowski measures

Another technique for morphological image analysis is based on a group of tools known as *Minkowski measures*. While the Voronoi tessellation can give us information about the distribution of a group of points, Minkowski measures can give us more specific information about the nature of an image. For a binary image in two dimensions, there are three Minkowski measures. These are the total covered area, A , the perimeter or boundary length, U , and the connectivity number (also known as the *Euler characteristic*), χ , of an image. The latter equals the number of regions of connected black pixels minus the number of completely enclosed regions of white pixels [112]. This gives a numerical representation of the connectivity of a binary structure. For example, if white pixels represent Au particles, and black pixels represent bare substrate, then a large and negative χ would indicate a structure of many isolated Au islands on the substrate. Conversely, a positive χ would suggest a network-like structure, with a connected arrangement of Au particles, and a number of separate “holes”.

However, the Euler characteristic alone cannot be used to define absolutely the nature of an image. For example, if an image consisted largely of isolated ring-like structures, with circles of white pixels enclosing black pixels, then χ would be very near to zero. This may mistakenly lead an automatic algorithm

to the conclusion of a featureless surface. If the value of U in this system were examined, it would be found to be quite large, which would not occur in a featureless system. Likewise, a featureless system would be expected to have either an extremely low or extremely high fractional coverage. Hence, if one is to gain a useful understanding of topology, these measures must be taken and interpreted as a group.

Minkowski measures are computationally inexpensive to calculate, as the processes involved use only the counting of pixels. Fig. 4.2 shows how an image can be broken down into a number of black squares (n_s), edges of black squares (n_e), and vertices (n_v). These can be used to calculate the Minkowski measures with the formulae

$$A = n_s, \quad U = -4n_s + 2n_e, \quad \text{and} \quad \chi = n_s - n_e + n_v. \quad (4.3)$$

The first of these is intuitive, and the last is a re-statement of Euler's equation noted above (Eq. 4.2). The expression for the perimeter results from the fact that each square has four sides, and in a system with zero perimeter, each of these sides will meet exactly one other side to form an edge. Every edge not between black squares (i.e. on the outside of a shape) will therefore be counted as part of the perimeter by this equation. An efficient algorithm for the calculation of the Minkowski measures using this principle is described by Pratt [113].

In the case of results from a simulation, calculation of Minkowski measures is relatively straightforward, as the system is inherently free from noise. They can therefore be useful for following the evolution of a structure, for example

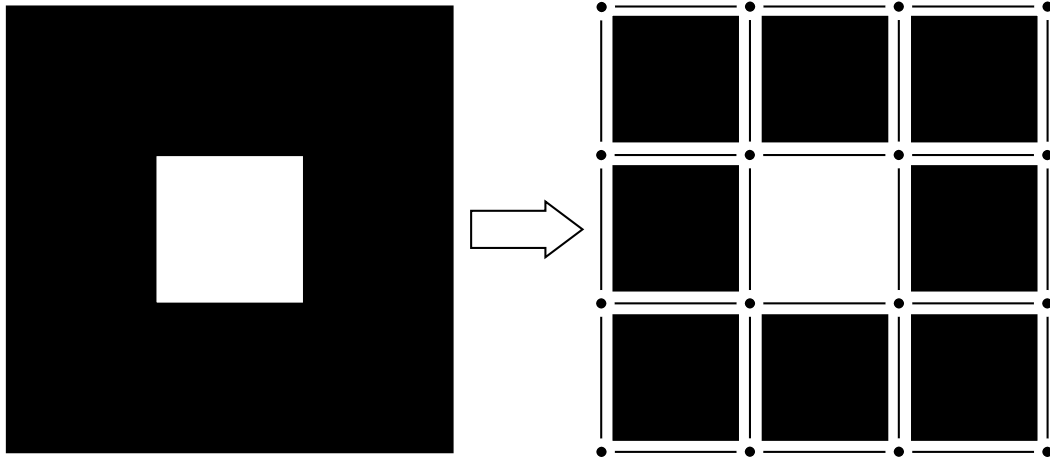


Figure 4.2: Decomposition of the pixels of a two-dimensional binary pattern (left) into squares, edges and vertices (right). For this example: number of squares $n_s = 8$, number of edges $n_e = 24$ and number of vertices $n_v = 16$ [112].

by calculating the three measures at different stages of a simulation. This is discussed in more detail in Chapter Six. Real images, however, must first be binarised before they can be analysed. Images such as those obtained by AFM may contain noise or particular features that mean isolating the underlying pattern is difficult. Furthermore, with certain types of structure, if the effective magnification of the AFM image is increased to such an extent that a pattern can be isolated, then the area available for analysis is often reduced to one of low statistical significance when the error is considered. In some of these cases, it is possible to use Minkowski measures in a different manner to analyse a spatial distribution of points.

Minkowski grain growth

Michielsen and De Raedt describe a method for Minkowski analysis of systems that can be reduced to point patterns [112]. In the previous section, I described

the way in which a cellular structure can be simplified to a Voronoi tessellation by using the locations of the centroid of each cell. If these locations are instead each used as *germs* for the growth of a two dimensional *grain*, then the values of A , U , and χ as a function of grain size (known as Minkowski *functionals*) can give us information about the distribution of the point set. The grains can be any shape, but as Fig. 4.3 illustrates, square grains are not subject to distortions by pixel discretisation. For this reason, all my analysis with this technique is based on square grains.

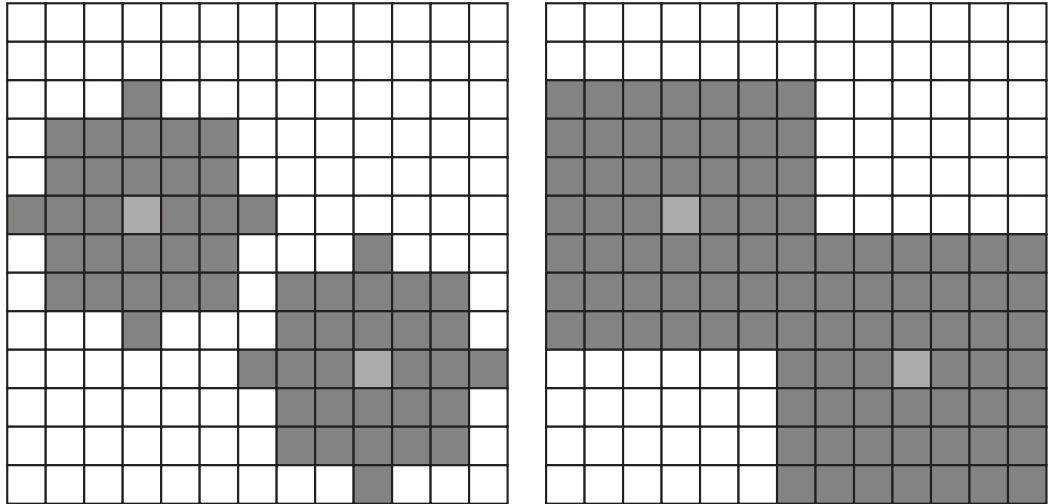


Figure 4.3: The decoration of germs (light grey) with grains (dark grey) that are discrete approximations to circles (left) and squares (right) [112].

The plots of the Minkowski functionals can be normalised for ease of comparison using the relations

$$\tilde{A} = A/L^2, \quad \tilde{U} = U/LN^{1/2}, \quad \text{and} \quad \tilde{\chi} = \chi/N. \quad (4.4)$$

where L is the edge length of the (square) image, and N is the number of grains. This leads to a normalised grain size $x = r/L$, where r is the radius

of the grain. The normalised Minkowski functionals for a Poisson distribution of points are known analytically. As with the Voronoi tessellation, a strong deviation from these graphs indicates that the distribution of points is not completely random. Conversely, a lack of deviation from the Poisson plots can be used to prove that a point distribution is random. Jacobs et al. were able to use this technique to demonstrate that, in certain conditions, the rupture mechanism of a PS film on silicon substrate is heterogeneous nucleation [47].

4.2 Analysis of experiments and simulations

4.2.1 Dewetted organometallic clusters

The analysis techniques described above can be applied to a wide range of systems. Fig. 4.4a shows a three-dimensional rendering of an AFM image of a structure formed by a dewetting process [109]. The specific system involved is organostannoxane [114] spin-cast onto a native-oxide silicon substrate. Fig. 4.4b shows a radially-averaged 2DFFT of the image in 4.4a, which exhibits a clear peak corresponding to feature sizes of the order 250nm. As mentioned earlier, this is often considered an indication of a spatially-correlated formation process such as spinodal dewetting.

Constructing a Voronoi tessellation of this cellular structure reveals a deviation from Poisson statistics: the entropy of the tessellation is 1.4 ± 0.1 , compared to the expected value of 1.71 for a Poisson distribution. Furthermore, the variance of the number of cell sides is 1.0 ± 0.1 . As mentioned earlier, a Poisson distribution is associated with a variance of 1.78. The points used to construct the Voronoi tessellation were then used as germs for the Minkowski

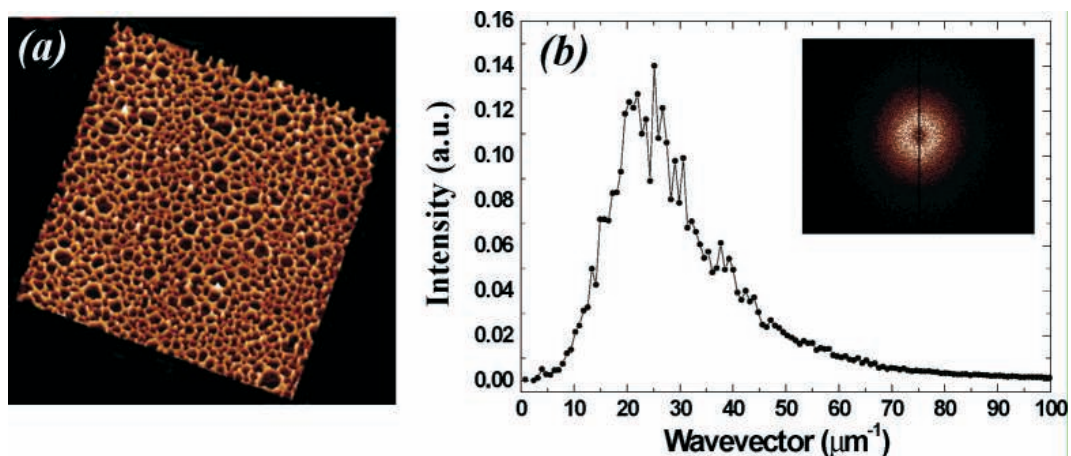


Figure 4.4: (a) Tapping mode atomic force microscope (AFM) image ($8\mu\text{m}\times 8\mu\text{m}$) of a thin stannoxane film spin-cast from toluene onto a native-oxide-terminated Si(111) substrate. The film has a cellular morphology with a mean thickness of approximately 4nm. The dewetting holes in the film expose the underlying SiO_2/Si substrate. (b) A radial average of a two-dimensional Fourier transform of the image shown in (a), with the 2DFFT shown in the inset. Note the presence of a peak at a wavevector of $25\mu\text{m}^{-1}$, suggesting the presence of an inter-cell correlation length of the order $2\pi/25\mu\text{m}$ (i.e. 250nm). Note that the somewhat poor statistics associated with the radially averaged Fourier transform which arises from the relatively small scan area (and thus small number of cells) associated with this image. [109].

grain growth technique.

The normalised Minkowski functionals for this distribution of cells are shown in Fig. 4.5. Considering first the x -dependent variation for a Poisson distribution of points (represented by the solid lines in Fig. 4.5a-c), we note that for small x , the grains are isolated. This produces a small covered area, a small boundary length, and a positive Euler characteristic. As the grain size is increased, the degree of overlap rises in a characteristic manner until the entire 2D plane is covered with black pixels producing a “saturated” covered area (Fig. 4.5a). The boundary length curve exhibits a clear peak (Fig. 4.5b) at intermediate values of x , while the Euler characteristic turns

negative (Fig. 4.5c). The minimum in the Euler characteristic curve (Fig. 4.5c) arises from the highly interconnected and “void-ridden” structure present at intermediate x values.

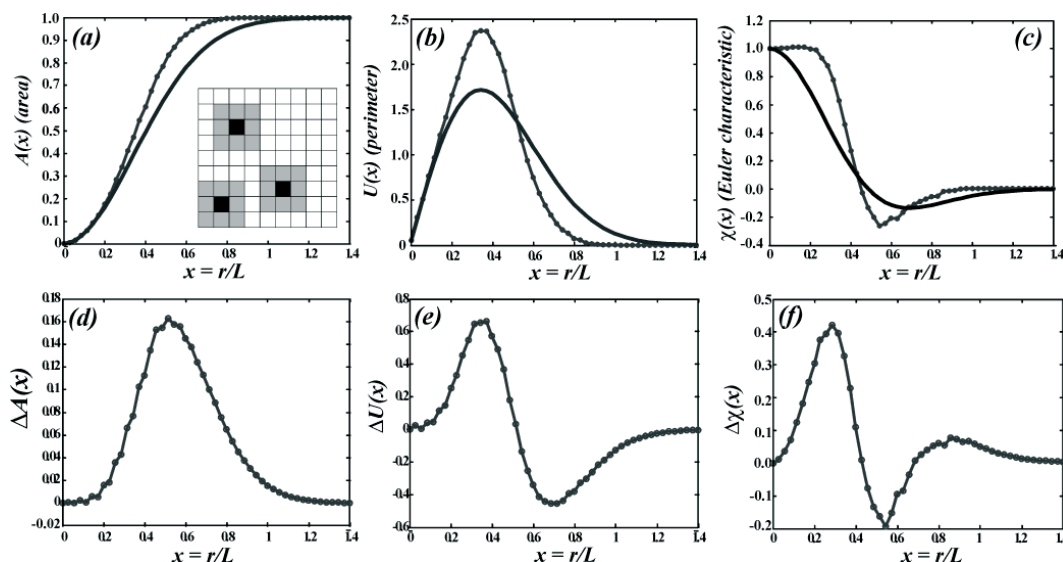


Figure 4.5: (a-c) Minkowski functionals (covered area, boundary length, and Euler characteristic respectively) for a Poisson distribution of points and a point set based on the coordinates of the dewetting cell centres for the image shown in Fig. 4.4 (solid lines and filled circles/solid lines, respectively). In each case, the functionals are plotted as a function of x , the normalized grain size. The inset to (a) depicts the difference between germs (the black pixels) and grains (grey pixels) centred on the germs. Note the strong deviation of each of the Minkowski functionals for the stannoxane-derived point system from the functionals for a Poisson-distributed set of points. (d-f) Difference between the stannoxane- and Poisson-derived result for each 2D Minkowski functional [109].

The behaviour of the Minkowski functionals for the stannoxane network is markedly different. For each measure, the curve for the stannoxane film centres (open circles-solid lines in Fig. 4.5a-c) deviates significantly from the Poisson line. It is particularly interesting to note that the Euler characteristic decreases much more rapidly for a Poisson distribution at low values of x than for the

distribution of points derived from the dewetting centres in the stannoxane film. This is a result of the local clustering of points that is inherent in a Poisson distribution. To highlight these deviations more clearly, Fig. 4.5d-f shows graphs of the stannoxane film-related Minkowski functionals minus the corresponding Poisson-derived functional. That the distribution of dewetting centres in the stannoxane film is far removed from that expected for a Poisson distribution of points is clear from these graphs.

This result is in agreement with the peak in the 2DFFT, in that it indicates a preferred length-scale of pattern formation, and a quantifiable deviation from purely random statistics. This fact could be used as an argument for a spinodal dewetting process, but a recent discussion of an entirely different system has raised some questions about the nature of ordering in such structures. Brinkmann et al. examined the spatial distribution of isolated islands of organometallic clusters deposited onto a hydrogen-passivated silicon surface [115]. Although their system results in a relatively ordered Voronoi tessellation, it was concluded that this was a result of droplet coalescence: the initially randomly distributed clusters were able to merge and form larger clusters. There is a defined “cut-off distance” inside which small islands can be captured by larger islands, and this was concluded to be the driving force behind the increased level of order in this system.

Although a system of isolated islands may at first seem to be the exact inverse of the dewetting organostannoxane system, the comparison is important. The formation of holes in a film is a process very similar in its dynamics to the growth of islands. However, rather than the capture of material from nearby islands, the growth of holes instead involves the coalescence of adjacent holes.

This is proposed as a possible mechanism to drive such structures to a higher degree of order. Although it is difficult to directly observe the dewetting process in this case, analysis of simulations can provide an insight into the types of pattern that can be formed by specific processes.

4.2.2 Simulated structures

Fig. 4.6 shows three frames from a simulation, along with a radially averaged 2DFFT of the final frame. It is apparent from 4.6a that the nucleation sites are uncorrelated: the vapour “bubbles” are clustered in some areas, and other areas have little or no nucleation. This is unsurprising, as the program dynamics are entirely stochastic, and the only possible nucleation mechanism is thermally activated. This distribution of bubbles is entirely consistent with thermally-activated nucleation. In 4.6b, the bubbles have expanded somewhat, and several have collided with other bubbles, either leaving a thin wall of particles, or in some cases almost completely merging together to leave only isolated particle groups.

In the final frame, 4.6c, the structure is foam-like and best described as a cellular network. Qualitatively, this structure appears to be much like many that have been observed in our nanoparticle experiments, and is similar to the structures described in section 2.1.1. More importantly, the two-dimensional Fourier transform 4.6d reveals the familiar ring which is sometimes cited as evidence for long-range ordering. This is clearer from the radial average, which has a very distinct peak. As a more quantitative examination of the same pattern, Fig. 4.7a shows a Voronoi tessellation of the final structure, along with Fig. 4.7b a plot of the probability of finding a cell with a given number of sides.

This reveals an entropy of 1.5 ± 0.1 , which agrees with the organostannoxane network within error.

Panels (c) and (d) of Fig. 4.7 show another simulation image, alongside the AFM image of the dewetting pattern of organometallic clusters on silicon. When compared, the two images appear to have very much in common. Moreover, when Minkowski functional grain growth analysis is applied to the simulation image, the resulting plots are virtually indistinguishable from those obtained from the experimental image. Fig. 4.8a-c show plots of the three Minkowski functionals as a function of the normalised edge length of square grains for both images. It is clear that the plots follow each other very closely, as do the difference plots, (d-f).

Tessellation analysis of the simulation image gives values of variance and entropy that correspond to those of the organostannoxane networks to within one decimal place ($\mu_2 = 1.0 \pm 0.1$ and $S = 1.4 \pm 0.1$). Although the systems are different, in that our simulation patterns result from evaporation and the patterns in (d) result from dewetting, their morphology is not only qualitatively similar but also *quantitatively indistinguishable*.

The patterns produced are known to be the result of random nucleation due to local thermal fluctuations, yet there still appears to be some kind of ordering. Put together, this evidence points strongly to one conclusion: *deviation from Poisson statistics, and the appearance of a well-defined correlation length, does not necessarily indicate an ordered formation mechanism*. So how do these deviations arise when the mechanism is known to have Poisson-distributed nucleation sites?

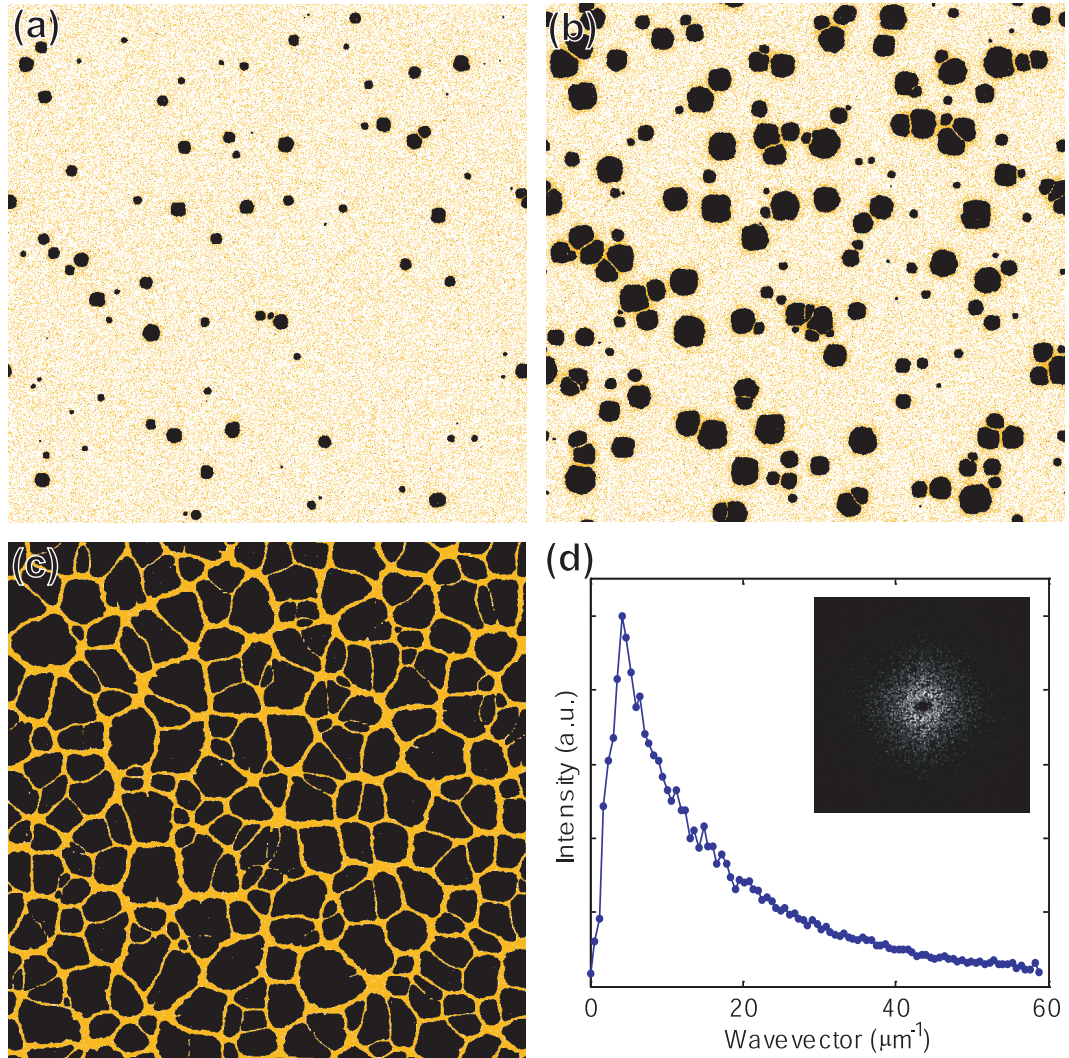


Figure 4.6: Simulated images from the homogeneous thermal nucleation regime, with $k_B T = \epsilon_l/4$, $\epsilon_n = 2\epsilon_l$, $\epsilon_{nl} = 1.5\epsilon_l$, $\mu = -2.25\epsilon_l$, $\text{MR}=30$, and a nanoparticle coverage of 20%, showing the early stages of pattern formation in a 4008×4008 pixel system after (a) 99 MC steps, with a distribution of nucleation sites that is clearly uncorrelated, (b) 199 MC steps, illustrating coalescence of neighbouring nucleation sites, and (c) 899 MC steps, the stable end result, which is best described as a cellular network. Pane (d) shows a radially averaged two-dimensional Fourier transform of (c), with a clear peak resulting from the ring visible in the inset.

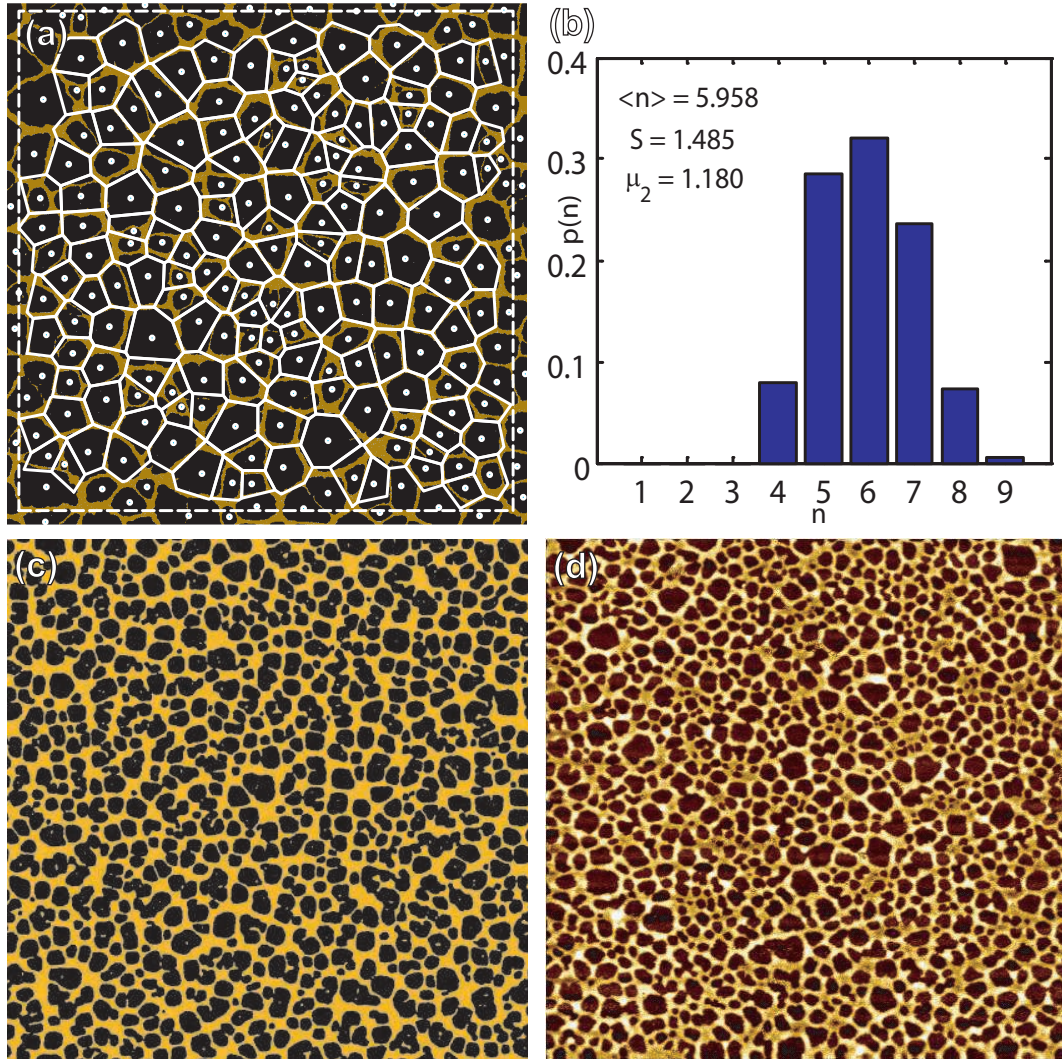


Figure 4.7: Statistical analysis showing (a) a Voronoi tessellation of figure 4.6c highlighting the cellular structure, and (b) a graph indicating the probability of a cell having a given number of sides in the tessellation. Panel (c) shows another simulation image, this time 3000×3000 , $k_B T = \epsilon_l/3$, $MR=50$, and a coverage of 35%, and panel (d) is the image from Fig. 4.4a, shown alongside panel (c) for ease of comparison. The qualitative similarity between these two images is striking.

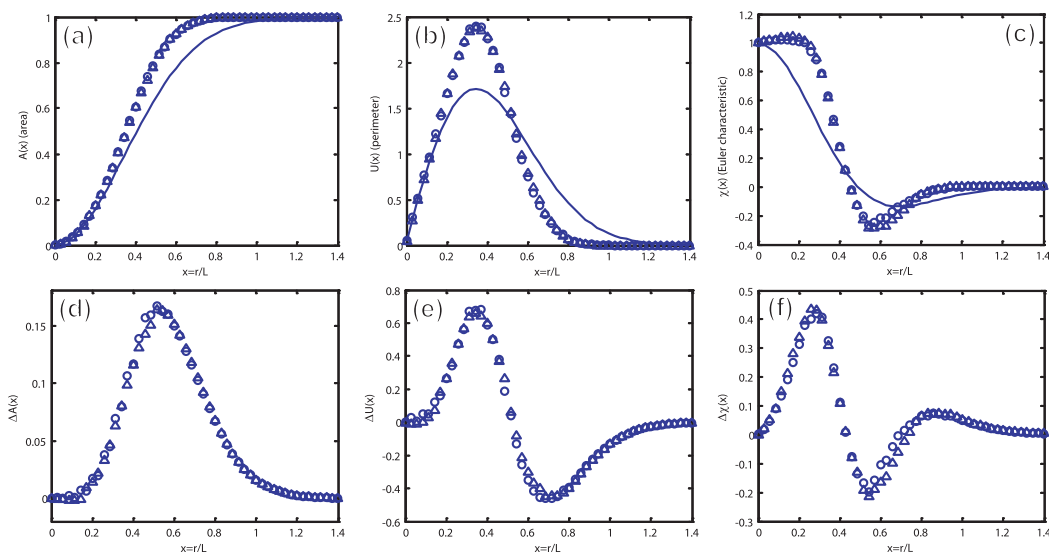


Figure 4.8: Minkowski functional grain growth analysis for the organostannoxane dewetting pattern (open circles) and the simulated nanoparticle image of Fig. 4.7c (triangles). Panels (a-c) show the plots of area, perimeter, and Euler characteristic respectively, with the expected behaviour for a Poisson distribution shown by the solid line. Panels (d-f) show the deviation from the Poisson lines in each case. It is clear that not only do both patterns have a strong deviation from the Poisson distribution, but they also follow each other quite closely.

4.3 Discussion and conclusions

Observing the progress of our simulations has led us to propose the following suggestion for a possible mechanism. Firstly, in a nucleation-driven dewetting or evaporation scenario, it is understood that the system conditions (temperature, volatility, or the balance of interfacial energies and viscosity) will lead to a specific nucleation rate. That is to say, there will be a certain number of nucleation events per unit area per unit time. As vapour bubbles (or dewetting centres) expand, there will be a smaller area available for nucleation. Furthermore, the area remaining will be less likely to host a nucleation event as the concentration of particles (or the thickness of the film) will be proportionally

greater. As a result, the nucleation rate will decay as the holes in the film expand. This means there is a limited time window in which nucleation can occur. This limits the maximum possible size of a vapour bubble and also narrows the overall hole size distribution.

Secondly, nucleation occurring close to the edge of an existing vapour bubble, or the coincidence of several nucleation events in the same region (a feature common in Poisson distributions), will generally lead to coalescence. The degree to which this coalescence occurs will depend on the dynamics of the system: in a system containing particles that are highly mobile (or a fluid that has a low viscosity and a strong dislike for the substrate) coalescence of holes is much more likely. An important thing to note however, is that the the closer together two nucleation events are (in both space and time), the more likely the resulting holes are to coalesce. This will effectively “wipe out” the clustering that is inherent in a Poisson distribution of points, even in a relatively immobile or viscous system.

These two points lead directly to the result that is seen so often: a cellular structure, with a narrow distribution of cell sizes, and a low degree of small-cell clustering. We cannot say definitively that structures that display these characteristics are not the result of a spinodal process, but it seems clear that in isolation, deviations from Poisson statistics do not provide sufficient evidence for long-range ordering.

Chapter 5

Organising Nanoparticles by Directed Dewetting

“Natura enim non imperatur, nisi parendo.”

Francis Bacon (1561–1626)

The behaviour of the solvent plays a key role in the formation of colloidal nanoparticle structures. This chapter describes a new technique that enables highly localised control of the morphology of nanoparticle patterns by direct modification of the solvent evaporation dynamics, and facilitates nanoscale confinement of single layers of particles by local manipulation of dewetting processes. Modifications to the simulation model of Rabani et al. [1] allow accurate reproduction of the nanoparticle patterns observed in these experiments. My simulations reveal that microscale oxide areas slow the evaporation of the solvent, such that the resulting morphology of particle patterns can be altered over a clearly defined region a few microns across [116].

5.1 Real-time observation during spin-casting

Section 3.4 briefly discussed the way in which the behaviour of the solvent during spin-casting could be examined by observing laser light reflected from the spinning sample. This technique is important for understanding the way in which the film thins. The late stage of evaporation— when there is a layer of liquid only a few nm thick— is particularly of interest as this represents the temporal domain of the simulations. This section describes the results obtained from real-time observation during spin-casting toluene solutions of gold nanoparticles passivated with different lengths of thiol molecule. This work was carried out at The University of Sheffield, in collaboration with Dr. Sasha Y. Heriot and Prof. Richard A. L. Jones of the Polymer Physics Group.

Fig. 5.1 shows a typical specular reflection trace taken from the apparatus. With knowledge of the refractive index of the liquid and the wavelength of the laser, it is possible to extract the thickness variation over time by measuring the positions of the peaks in this trace. The result of this is shown in Fig. 5.2. It should be noted, however, that this is only an approximation: the increasing concentration of particles will modify the refractive index of the solution, particularly in the late stages of drying.

The thickness data fit well to a sixth-order polynomial (although this choice of fit is arbitrary). Extrapolating this fit to $h=0$ — a small interval considering the spacing of the points— allows us to obtain an approximation of the time it takes the last nanometre of liquid to evaporate. The results of this are shown in Table 5.1. Interestingly, there appears to be a clear dependence on the length of the thiol chain: longer chains seem to cause the last nanometre of

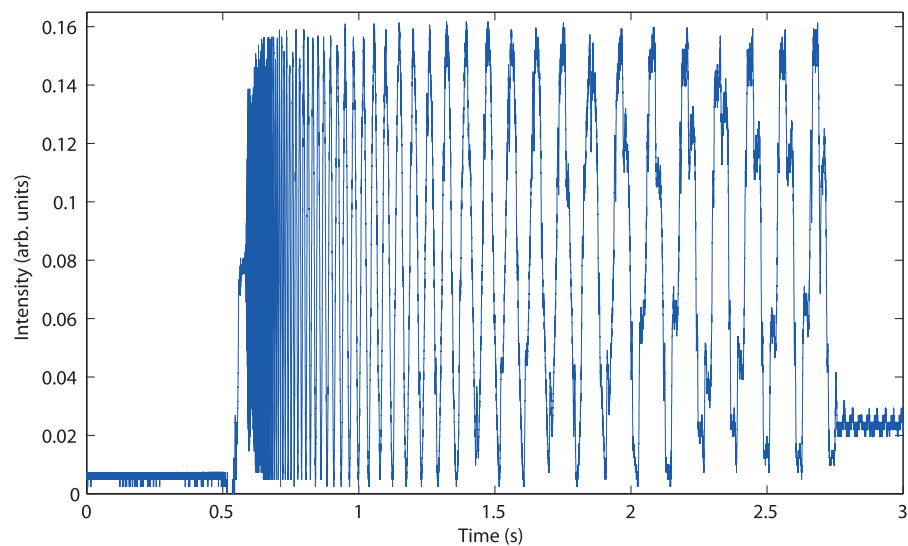


Figure 5.1: A typical specular trace from the optospinometer, showing the distinctive oscillations resulting from constructive and destructive interference between light reflected from the substrate and light reflected from the toluene surface.

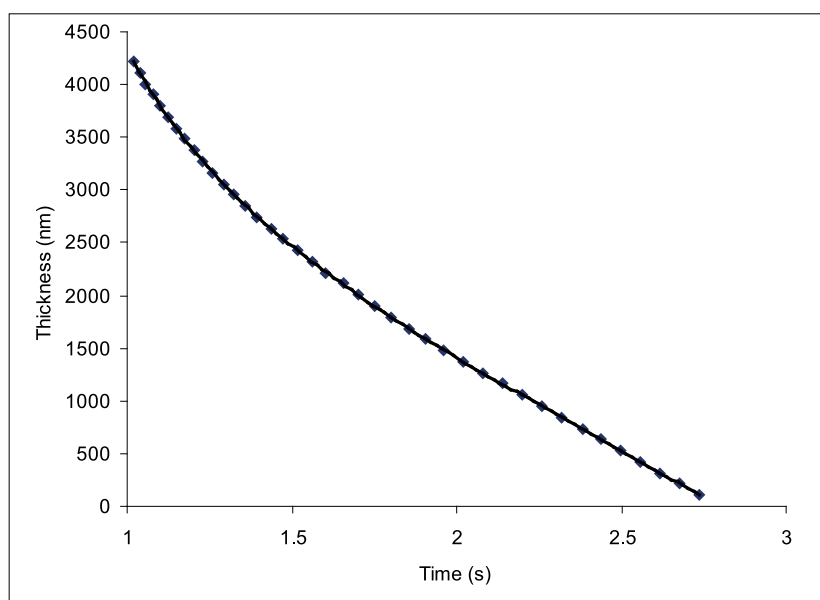


Figure 5.2: The thickness trace obtained from Fig. 5.1 (filled diamonds), with a sixth-order polynomial fit (solid line).

liquid to evaporate more slowly. It should of course be noted that this apparent difference could also be down to differing refractive indices as mentioned earlier, or differences in the level of “interdigitation” of thiol chains of different lengths. This dependence is therefore only tentatively noted, as further experiments would be required for confirmation. The important result, however, is the order of magnitude of the time of the evaporation of the last nanometre, which is approximately 1ms. The importance of this shall be discussed later.

Thiol carbon chain length	Approximate evaporation time of last nm (ms)
5	0.61
8	0.74
12	0.86
18	1.00

Table 5.1: The approximate time taken for the evaporation of the last nm of liquid for passivating thiols of different chain lengths.

5.2 Modifications to the simulations

5.2.1 Background

The simulations described in Chapter Three are capable of replicating a large number of the basic structures that are seen in our spin-casting experiments. Patterns of isolated islands, worm-like domains, continuous labyrinthine patterns, and polygonal networks can be produced by varying the particle coverage and the rate of solvent evaporation. Certain classes of cellular structure in particular are reproduced with an accuracy that renders them statistically indistinguishable from experiment, as discussed in the previous chapter. In each of these cases, the driving force behind pattern formation is the nanoscopic

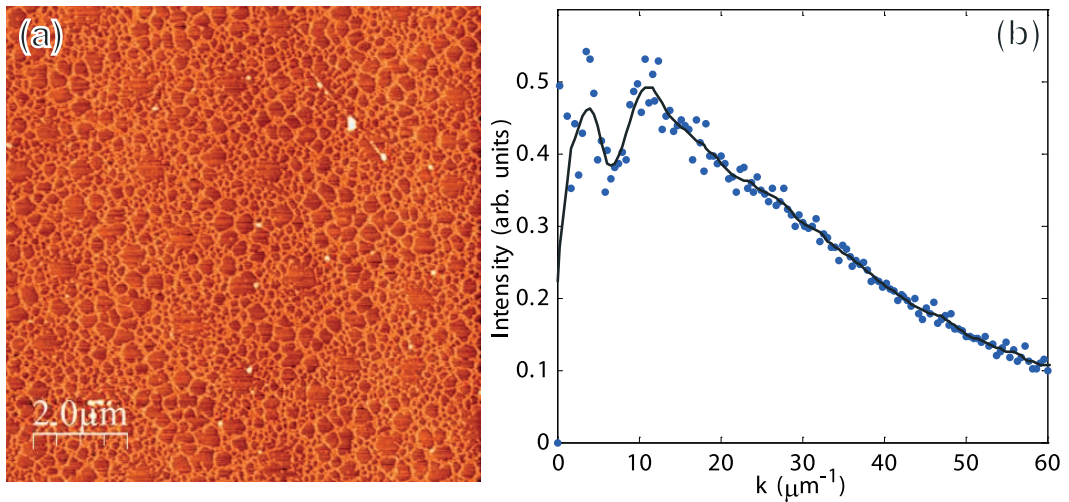


Figure 5.3: (a) An AFM image of a two-level cellular structure formed by spin-casting a solution of gold nanoparticles in toluene onto a silicon substrate, and (b) a radially-averaged two-dimensional fast Fourier transform of (a), with the original “binned” data shown as filled circles. The solid line is the same data after smoothing by a 10-point “LOWESS” method, which clarifies the bimodal nature of the distribution.

dynamics of solvent evaporation. There are, however, a number of common experimental phenomena that cannot be simulated by this method. For example, Fig. 5.3a shows a structure that is frequently observed in our experiments. A radially-averaged 2DFFT of this image (Fig. 5.3b) reveals that the pattern exhibits not just one, but two preferred cell sizes.

A detailed examination of the parameter space has shown that it is not possible to reproduce this structure by means of the simulations described in Chapter Three. Fig. 5.4 shows a phase diagram that is broadly representative of the structures that can be produced, and Fig. 5.5 shows a detailed section of this, which illustrates the main morphologies, and the temperature and particle coverage ranges over which they occur. Although this is only a two-dimensional cross-section of the parameter space, wider exploration has revealed that in no

region is there a cellular network that exists on two (or more) length scales. The only way that it has been possible to reproduce this type of structure is by considering the three-dimensional behaviour of the system, and incorporating a compensation for this into the simulation.

5.2.2 A dynamic chemical potential

Although the original model was two-dimensional, Sztrum et al. [117] have recently extended it to three dimensions to explain the formation of nanoparticle “stalagmites”. However, the pattern-forming processes discussed here occur within the final few nanometres of the evaporating solvent. Therefore, the physical nanoparticle “sub-system” is truly two-dimensional whereas the solvent “sub-system” retains some three-dimensional aspects. In particular, the interaction of the solvent with the substrate, and therefore its evaporation rate depends on the amount of solvent remaining. A simple change to the Hamiltonian of the original two-dimensional model is sufficient to capture the resulting partially three-dimensional nature. Specifically, by making the chemical potential an explicit function of the global solvent density[†], we can model an increase in the modulus of μ as the solvent layer thins during evaporation. In this “pseudo-three-dimensional” approach, the density dependence corresponds to a thickness-dependent disjoining pressure [37], accounting for substrate wettability in continuum models [118, 119]. As a result, the solvent evaporates with a rate inversely proportional to its coverage.

Fig. 5.6a shows a detailed section from the image in Fig. 5.3a, and Fig. 5.6b

[†]Trials were performed using the *local* solvent density, but it was found that this only served to increase the computational effort required, and produced no discernible difference from simulations using the global solvent density.

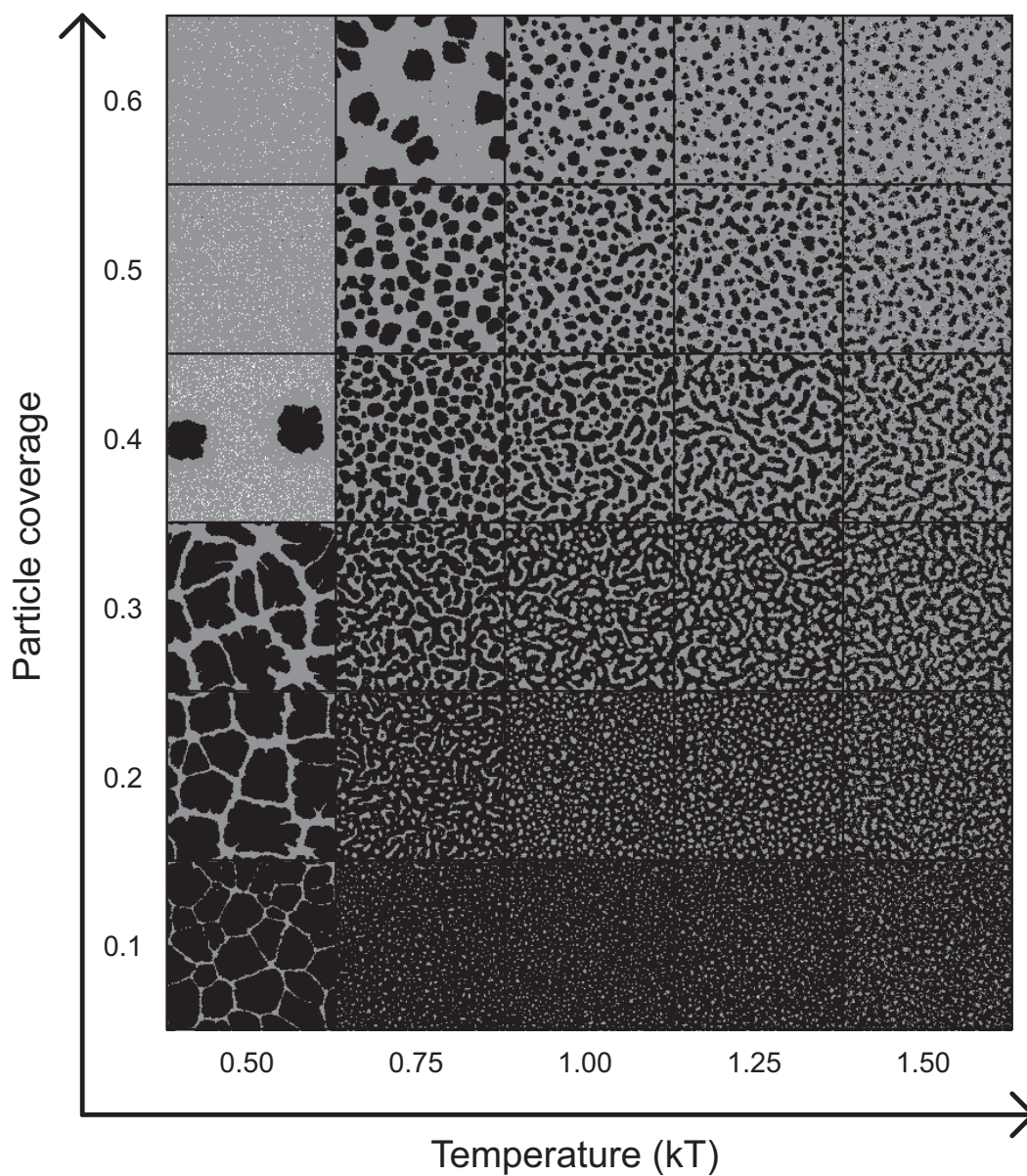


Figure 5.4: A representative broad phase diagram showing the structures that are produced at different temperatures and coverages after 1000 MC steps in a 1024×1024 solvent cell system with the parameters $\epsilon_l = 2$, $\epsilon_n = 2\epsilon_l$, $\epsilon_{nl} = 1.5\epsilon_l$, $\mu = -2.25\epsilon_l$, and $MR=20$.

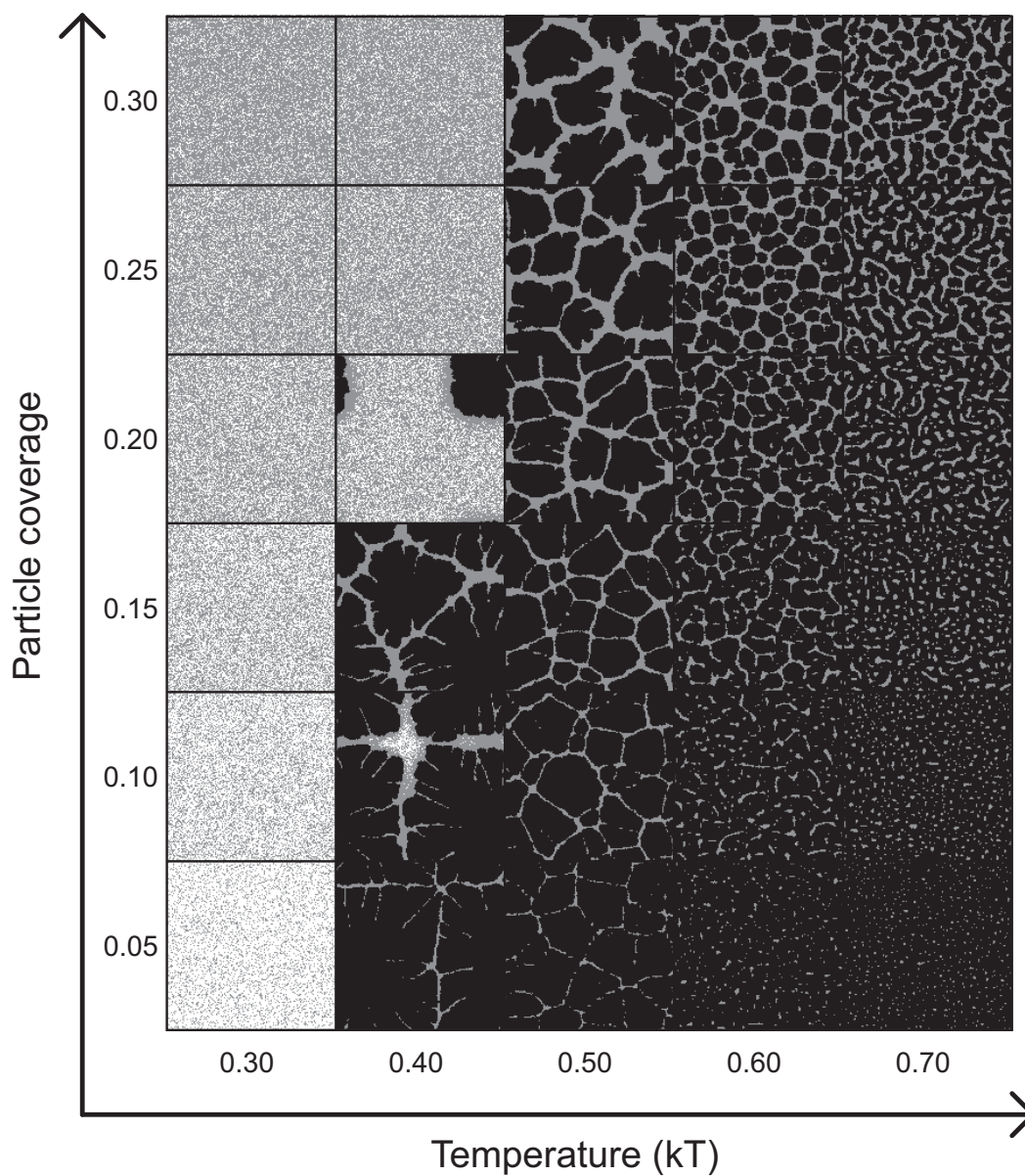


Figure 5.5: A more detailed version of a small region of the phase diagram in Fig. 5.4 (but after 2000 MC steps), showing the range of temperatures and coverages over which the majority of common structures are produced. One edge of the useful parameter space is defined by parameter ranges where no evaporation occurs in a reasonable time scale (i.e. at low temperatures).

is a simulated image showing the result of making μ a function of global solvent density. The exact relation which best matches the experimental data in this case is a fractional power law, as detailed in the figure caption. This functional form causes “normal” slow nucleation and growth of holes in the early stages, followed by a rapid acceleration in the evaporation rate leading to accelerated nucleation in the later stages, producing two distinct length scales of network. The simulation matches the experimental image not just qualitatively, but also quantitatively using Voronoi tessellation and Minkowski analysis of the positions of the cell centres (Figs. 5.7 and 5.8).

Increasing the coupling between μ and solvent coverage produces a wider distribution of cell sizes, as illustrated in Fig. 5.6d. This replicates the effect of using chloroform as the solvent in the experiments (5.6c), which is significantly more volatile than toluene. It is interesting to note that the large holes in these simulated structures are formed spontaneously, without the manual introduction of nucleation sites described by Yosef and Rabani [95]- a technique which shall be discussed later.

5.2.3 Exploring the dynamic chemical potential

It is possible to produce a wide range of multiple length scale patterns by varying the functional form of $\mu(v)$. A number of functional forms were tested, and a power law was found to provide good flexibility with two simple parameters (the exponent, A , which determines the shape of the curve, and a multiplier defining the minimum value of μ). An exploration of the parameter space with values of A from 0.1 to 10, and a multiplier of 0.1 or 0.5 is shown in Figs. 5.9-5.12. All of the images shown appear to be physically plausible: none would

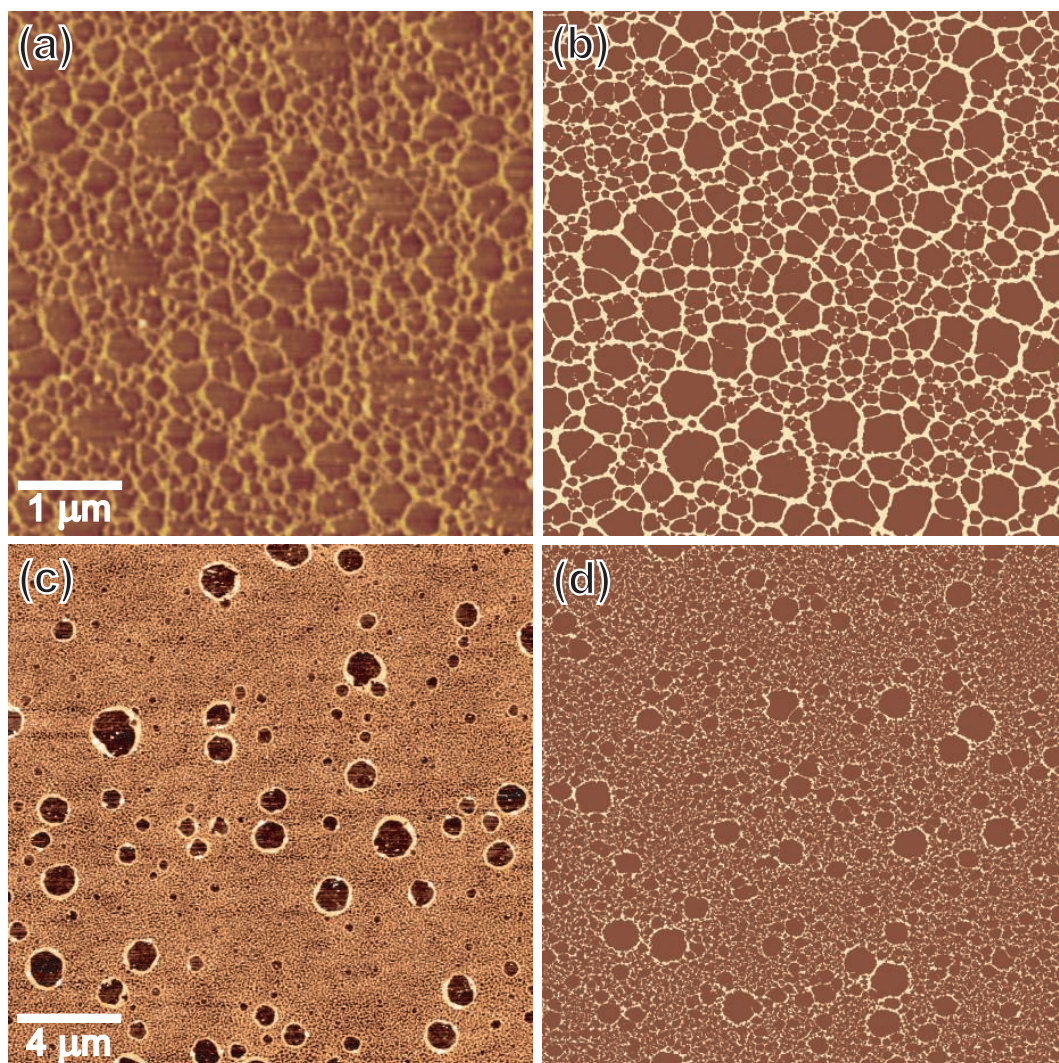


Figure 5.6: (a) An AFM image of a two-level cellular structure formed by spin-casting a solution of gold nanoparticles in toluene onto a silicon substrate (M. O. Blunt), (b) a simulated structure formed by linking the chemical potential (μ) to the solvent density (in the form $\mu(v) = \mu_0 + (0.1\mu_0 \times v^{0.7})$, where v is the fraction of solvent that has become vapour, and μ_0 is the value of μ at the beginning of the simulation), (c) an AFM image of gold nanoparticles spun onto silicon from solution in chloroform (M. O. Blunt), and (d) a simulated image with a much stronger coupling between μ and solvent coverage (in the form $\mu(v) = \mu_0 + (0.5\mu_0 \times v^{0.7})$)

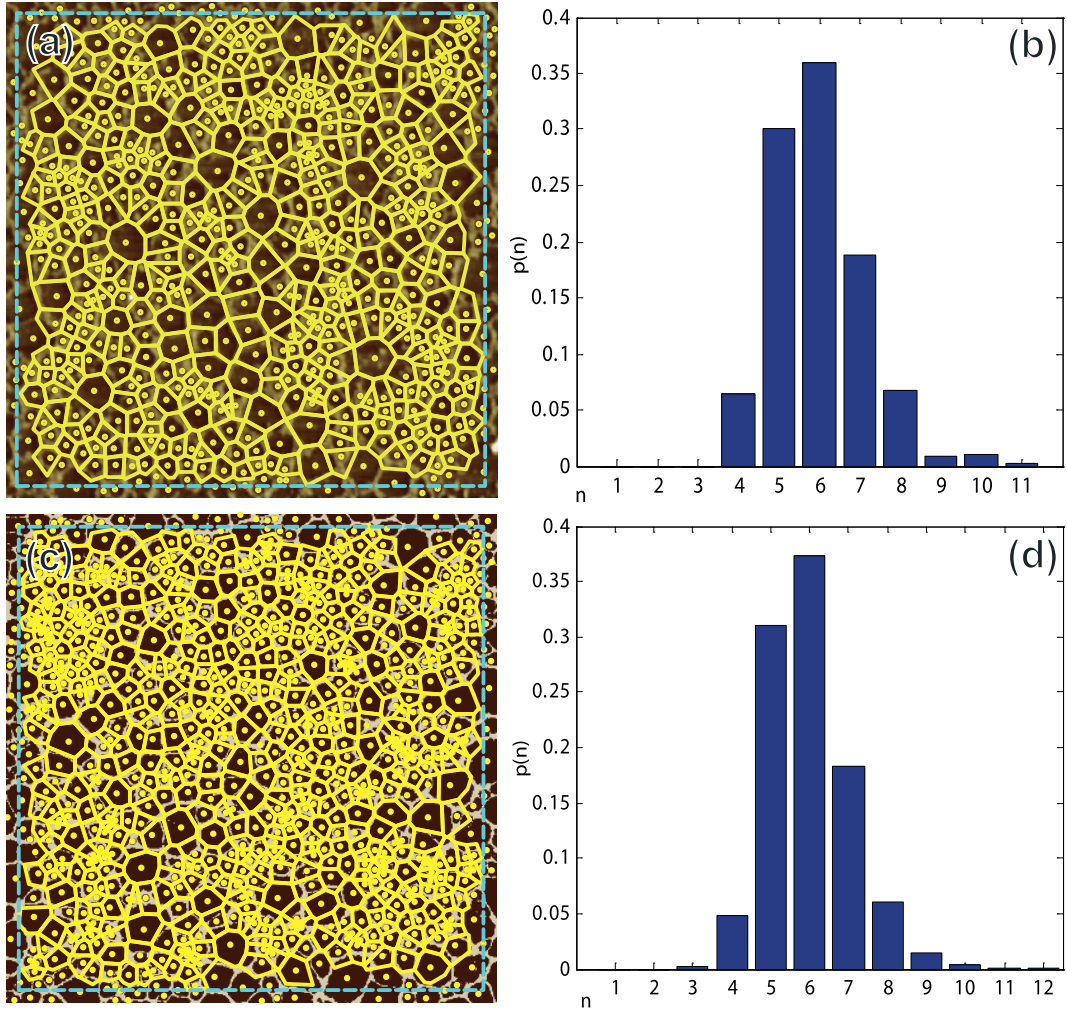


Figure 5.7: (a) The AFM image from Fig. 5.6a with a Voronoi tessellation superimposed, (b) a plot of the frequency distributions of cells with a given number of sides for the tessellation in (a), having a variance of 1.3 ± 0.1 , and an entropy of 1.50 ± 0.06 , (c) a simulation image with a coupling between μ and solvent coverage with a superimposed Voronoi tessellation, and (d) a plot of the frequency distributions of cells with a given number of sides for the tessellation in (c), having a variance of 1.3 ± 0.1 , and an entropy of 1.48 ± 0.06 .

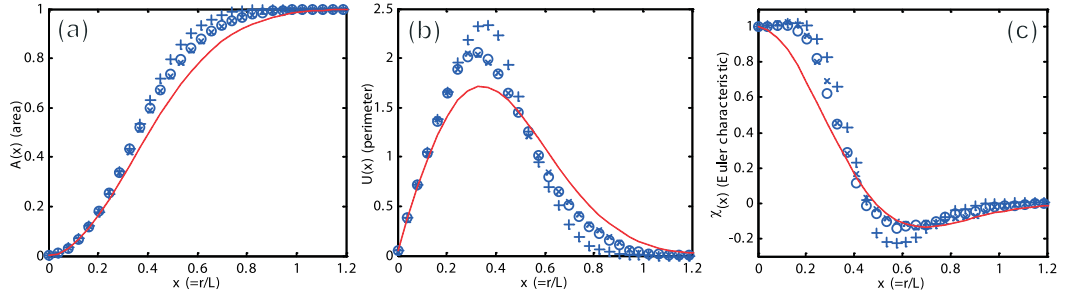


Figure 5.8: Square-grain Minkowski functional comparison of the structures in Fig. 5.6 (a) and (b), showing the experimental data as crosses, simulated data as open circles, and for the purposes of comparison, data from a single-length-scale network is shown as plus symbols, and the solid line represents the theoretical result for a purely random distribution.

look out of place in an AFM scan. Furthermore, as illustrated in Fig. 5.6, many have indeed been seen in experiments.

As an interesting aside, many images in these sets appear to have been started from identical pseudo-random seeds, and show very similar nucleation sites (this is particularly noticeable in the last three images in Fig. 5.10). This results from a quirk in the way in which the HPC grid distributes tasks, combined with the use of a time-based random seed in my program. If several versions of the code (albeit with different parameters) are passed to the HPC grid at the same time, then each will start at the same moment on the (synchronised) clock of each node. The random seed will therefore be the same, as it is based on the time of the clock. With hindsight, intentionally setting the same seed for each run could in fact be a good way to visually compare the specific effect of a change in parameters.

The parameter space with a dynamic chemical potential is almost unlimited, as the functional form can be chosen arbitrarily. Indeed, the choice of a power law was arbitrary, and a number of other possibilities could be explored,

including non-monotonic functions. The interesting point is that although the power law is simple, it does appear to reproduce a number of two-level cellular structures.

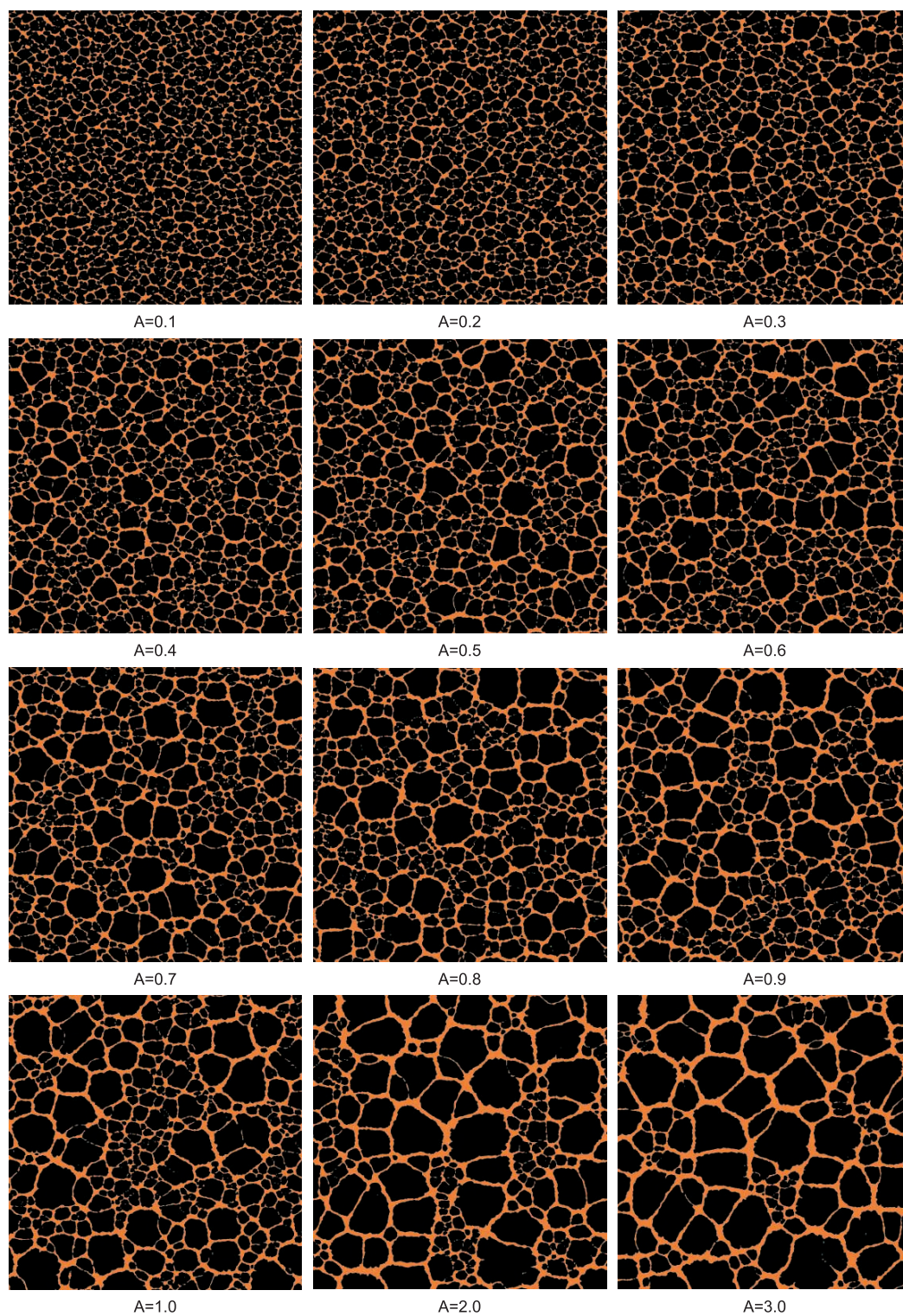


Figure 5.9: Simulation results with dynamic μ , continued in Fig. 5.10.

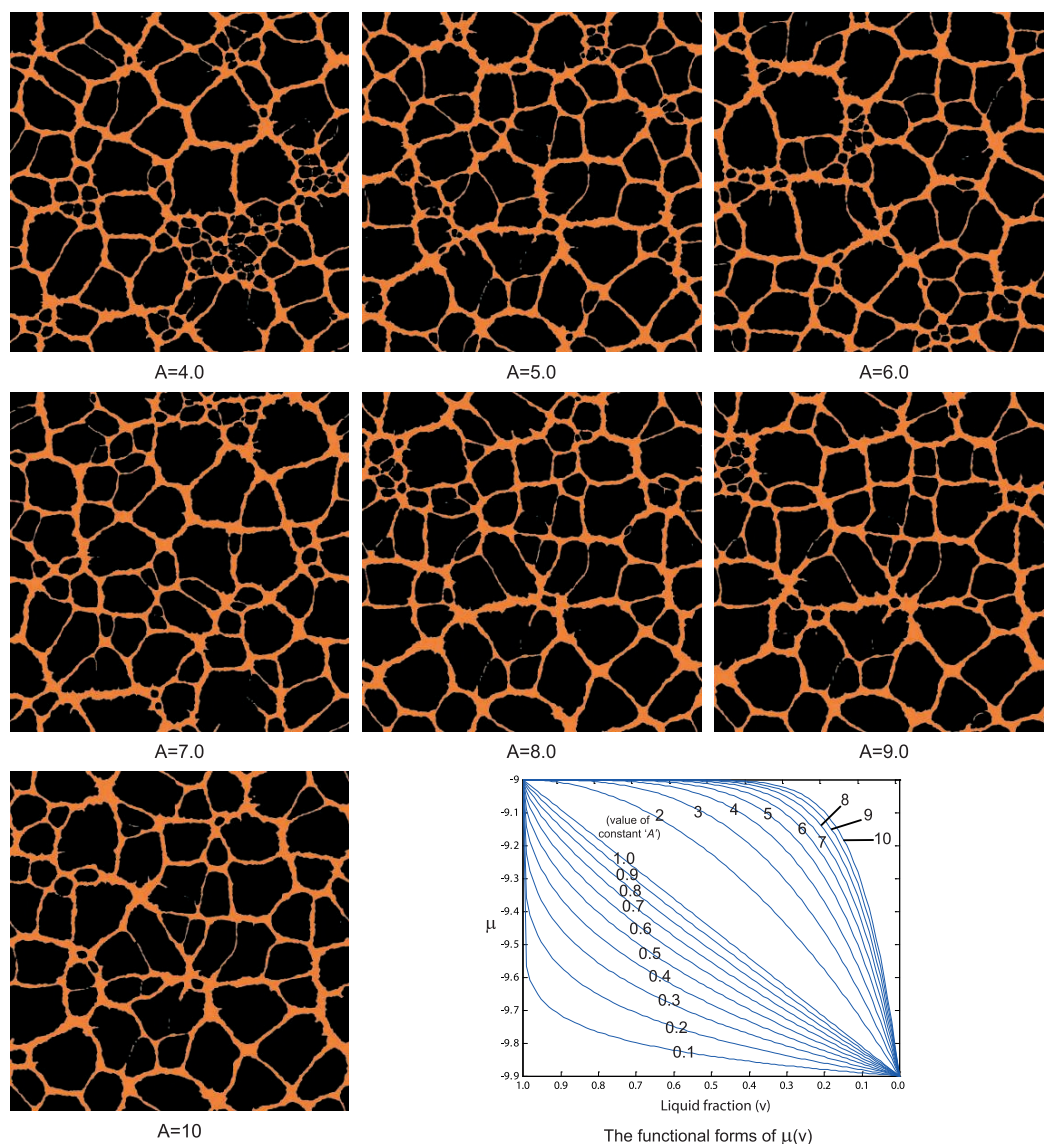


Figure 5.10: Continued from Fig. 5.9, the range of images produced when $\mu(v) = \mu_0 + (0.1\mu_0 \times v^A)$, where v is the fraction of solvent that has become vapour, and μ_0 is the value of μ at the beginning of the simulation. The last panel shows plots of these functional forms of $\mu(v)$. All images are 2048 lattice sites square, with all parameters (excluding μ) identical to those used to produce Fig. 3.5b.

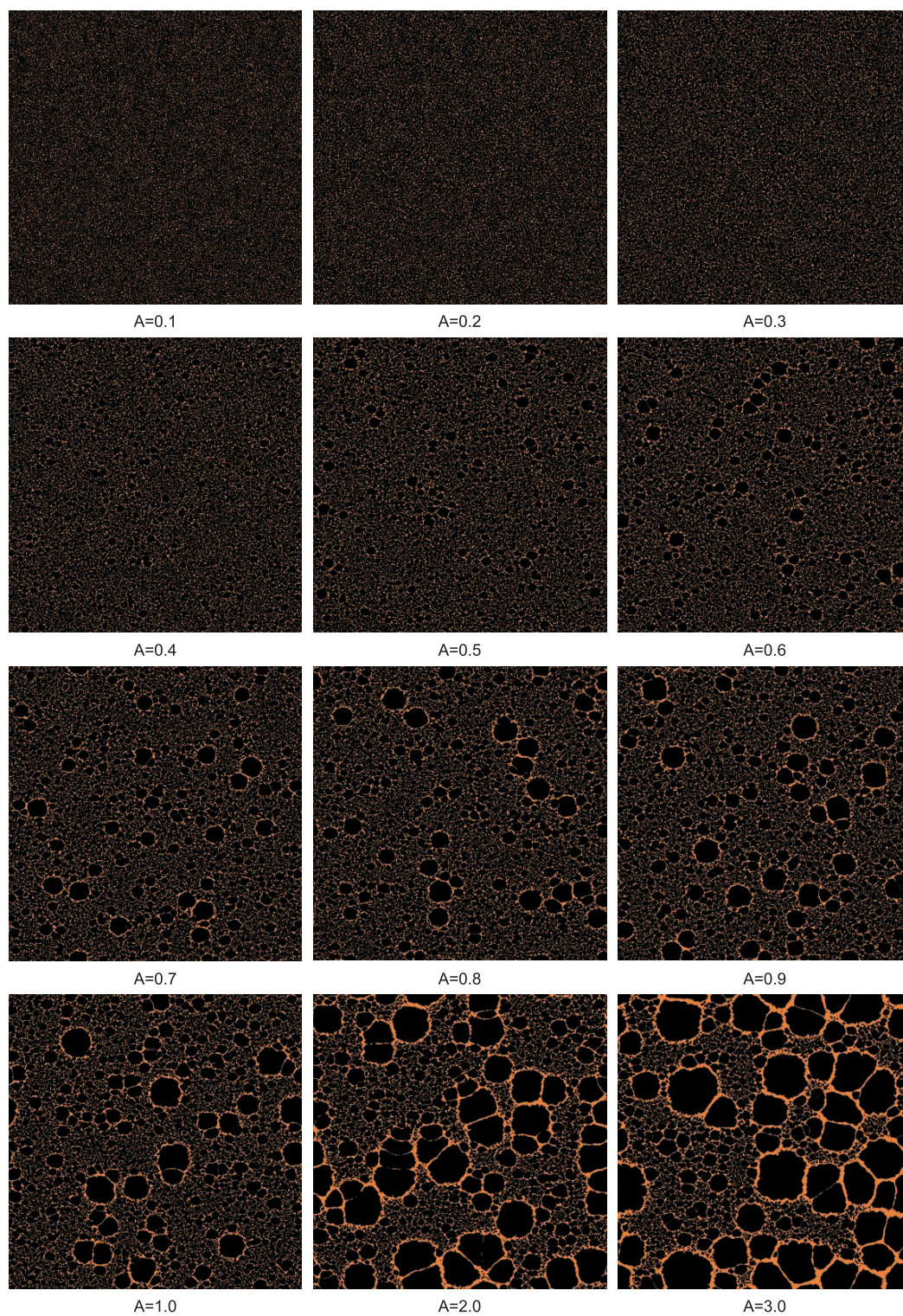


Figure 5.11: Simulation results with dynamic μ , continued in Fig. 5.12.

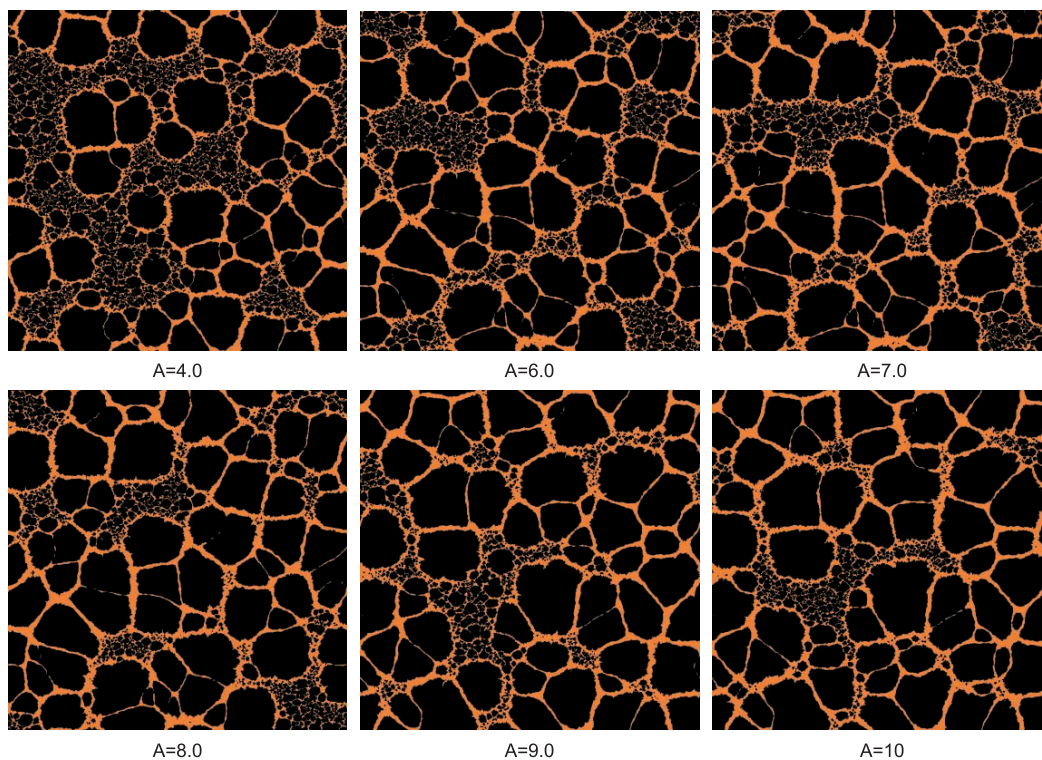


Figure 5.12: Continued from Fig. 5.11, the range of images produced when the gradient in μ is much steeper, such that $\mu(v) = \mu_0 + (0.5\mu_0 \times v^A)$, where v is the fraction of solvent that has become vapour, and μ_0 is the value of μ at the beginning of the simulation. Again, all images are 2048 lattice sites square, with all parameters (excluding μ) identical to those used to produce Fig. 3.5b.

5.2.4 Heterogeneous surfaces

It is clear that the behaviour of the solvent plays a critical role in determining the nature of the nanoparticle patterns that are observed; to a large extent, the particles are merely passengers on the tide of the solvent, and their final positions describe the history of flow and evaporation. Modifying the surface of the substrate to perturb the behaviour of the solvent must therefore lead to a modification of the nanoparticle structures. Indeed, Parker et al. [120] have previously demonstrated that photolithographically patterned substrates

can be used to drive three dimensional cluster accumulation along the edges of microstructures formed in photoresist. It is possible to dramatically extend this “guiding” principle to control, with a remarkable degree of precision, two-dimensional pattern formation in nanoparticle assemblies.

Experimental method

Native-oxide terminated silicon (111) samples of 1cm x 1cm were prepared for hydrogen-passivation in a clean room environment by ultrasonic cleaning in ethyl lactate, acetone, methanol, and then isopropanol. This was followed by further cleaning in “piranha solution” (a 4:1 mixture of concentrated sulphuric acid and 30% aqueous hydrogen peroxide solution) at 140°C to remove any trace of organic residue. The hydrogen passivation was carried out by an aqueous hydrofluoric acid etch followed by an anisotropic etch in ammonium fluoride to create a near atomically smooth surface. Gold markers (approx 20nm thick) were then deposited in vacuum through a shadow mask in order to locate oxide structures more easily after nanoparticle deposition. An Asylum Research MFP-3D AFM system operating in intermittent contact mode with closed-loop control was used for both imaging and local oxidation of the hydrogen-passivated silicon samples. Nanosensors PPP-EFM-50 platinum-iridium coated silicon probes (tip radius <7nm) were used to carry out the oxidation and to obtain post-oxidation images. Oxidation was carried out at a probe bias of -10V, and in 70% humidity. Octanethiol-passivated Au nanoparticles were prepared in toluene using the method pioneered by Brust et al. [27]. A 25 μ l droplet of an appropriately diluted solution was then placed on the locally oxidised substrate and the sample subsequently spun at 4krpm.

Olympus AC240 silicon probes (tip radius 7nm) were then used to acquire images after deposition of nanoparticles.

Results and simulations

Fig. 5.13a shows the striking effect on nanoparticle organisation of an AFM-oxidised $4\mu\text{m} \times 4\mu\text{m}$ square on hydrogen-passivated silicon. There is a clear and extremely sharp transition from a cellular structure on the oxide region, to broken worm-like pattern elsewhere. Given that the edge of the oxide region should in principle represent a steep gradient in wettability, with strong implications for dewetting-mediated pattern formation, the lack of a region denuded of nanoparticles at the edge of the oxide is intriguing. I shall return to a discussion of this important point later.

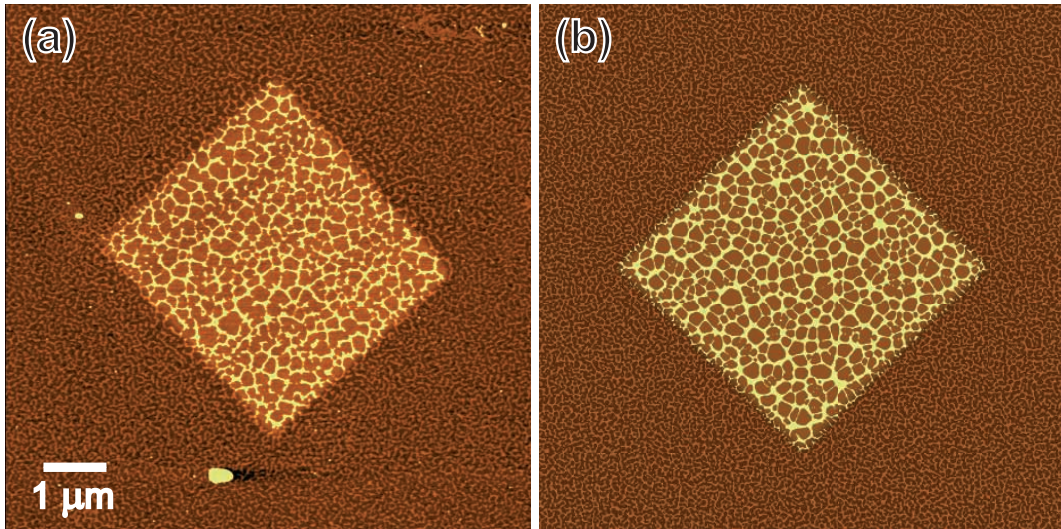


Figure 5.13: (a) An AFM image of gold nanoparticles spun from solution in toluene onto a hydrogen-passivated silicon substrate with an AFM-patterned $4\mu\text{m} \times 4\mu\text{m}$ square of oxide in the centre (M. O. Blunt), and (b) the result of a simulation with $|\mu|$ 6% lower on the oxide area.

Simulations indicate that cellular networks are generated by slower solvent

evaporation than that which occurs in the formation of labyrinthine structures. This would suggest that evaporation is somehow retarded by the presence of the oxide. One way to achieve this effect in simulation is to make temperature a function of position, and define the oxide area as cooler than the surroundings. Physically, this could be the result of the 100-fold difference in thermal conductivity between SiO₂ and bulk silicon [121]; the cooling effect of evaporation could be offset by a rapidly equilibrating flow of heat from the bulk, except where the oxide barrier exists.

Assuming a bulk temperature of 290K (17°C), simulations indicate that the surface of the oxide area would need to be at 235K (-38°C) to produce this effect. However, calculations based on the thermal conductivity of SiO₂ tell us that a temperature difference of 55K across a 3nm thick 4μm square will cause a flow of heat of the order $\frac{1}{2}$ Watt. This is enough for a layer of toluene on the oxide surface several nanometres thick to reach thermal equilibrium with the bulk in a matter of a few tens of picoseconds, orders of magnitude faster than the time-scale determined by the real-time observations in section 5.1.

The alternative explanation is that the solvent finds the oxide areas more wettable. Fig. 5.13b shows the result of spatially varying the value of μ , such that its modulus is very slightly (6%) lower on the oxide than in the surrounding area, with an interface region comprising a 100nm linear transition. This equates to a stronger attraction to the surface (and therefore a greater wettability) in the region of the oxide. The image shown in Fig. 5.13b matches the experimental result extremely well: the simulated cellular structure on the oxide is statistically indistinguishable from that in the experimental image.

Contact angle measurements (determined from profiles of toluene droplets)

show, however, that there is no observable difference in the wettability of macroscopic volumes of toluene on H:Si(111) and native oxide-terminated Si(111) surfaces having comparable roughness. Both substrates yield a contact angle close to zero ($\approx 5^\circ$), albeit with a very large error bar ($\pm 50\%$). These measurements would seem to be at odds not only with the results of Fig. 5.13, where a greater wettability of the oxide region is observed, but with estimates of Hamaker constants [37] which yield different signs for the air/toluene/silicon and air/toluene/silicon oxide systems. We can, however, explain these apparent discrepancies between wetting theory and experiment in terms of the nanoscale structure of the silicon oxide-silicon system. First, as pointed out by Seeman et al. [122], the appropriate system to consider for the estimation of Hamaker constants is air/toluene/SiO/Si where the native oxide layer is $\approx 2\text{nm}$ thick. In this context, the high wettability of toluene on native oxide-terminated silicon seen in the contact angle measurements is not unexpected. Second, and of key importance for our directed dewetting experiments, the stronger affinity of the apolar solvent for the oxide region rather than for the H:Si(111) surface in Fig. 5.13 can largely be rationalised in terms of the higher degree of roughness/porosity of silicon oxide formed using scanning probe nanolithography as compared to oxides prepared by more conventional (chemical/thermal) methods [106, 123].

Below a critical feature linewidth ($\approx 200\text{nm}$), the effect of oxide regions on the far from equilibrium flow of solvent is radically different from that shown in Fig. 5.13. Fig. 5.14a shows nanoparticle patterns formed in the presence of SiO₂ rings of $1\mu\text{m}$ diameter on hydrogen-passivated silicon. The 100nm -wide lines are almost completely free of particles, and a clearly denuded zone extends

around them for a further 100nm. It is possible to reproduce this effect in our simulations by completely removing sections of solvent and nanoparticles from regions representing the oxide rings prior to the start of the simulation. This is similar to the technique employed by Yosef and Rabani [95]. Although this modification may seem unphysical, it is in fact a further compensation for the two-dimensional nature of the simulation. The importance of dewetting nucleated by a gradient in wettability has been discussed in some depth for thin liquid and polymer films on heterogeneous substrates [124–126]. While a wettability gradient exists for the AFM-defined patterns shown in both Fig. 5.13 and Fig. 5.14, it is only for the latter that a denuded zone free of nanoparticles is observed in the vicinity of the surface heterogeneity, indicating that the feature linewidth plays a fundamental role in driving the rupture of the solvent/nanoparticle film.

In addition to the chemical heterogeneity represented by the oxide regions, as the solvent thins by evaporation, there comes a point when the 3nm height difference of the small oxide regions becomes very significant. These regions are likely to be the first in which the thickness of the film becomes small enough for the disjoining pressure to cause nucleation of a hole in the film. This tailor-made hole will then grow by evaporation, isolating a small group of nanoparticles inside the ring. A simulation including this modification, and also a solvent density-dependent chemical potential (as described for Fig. 5.6), is shown in Fig. 5.14b. This directed dewetting process enables confinement within specific nanoscale surface regions without the need for chemical functionalisation of the nanoparticles.

The effect of the greater roughness of the oxide regions can be exploited

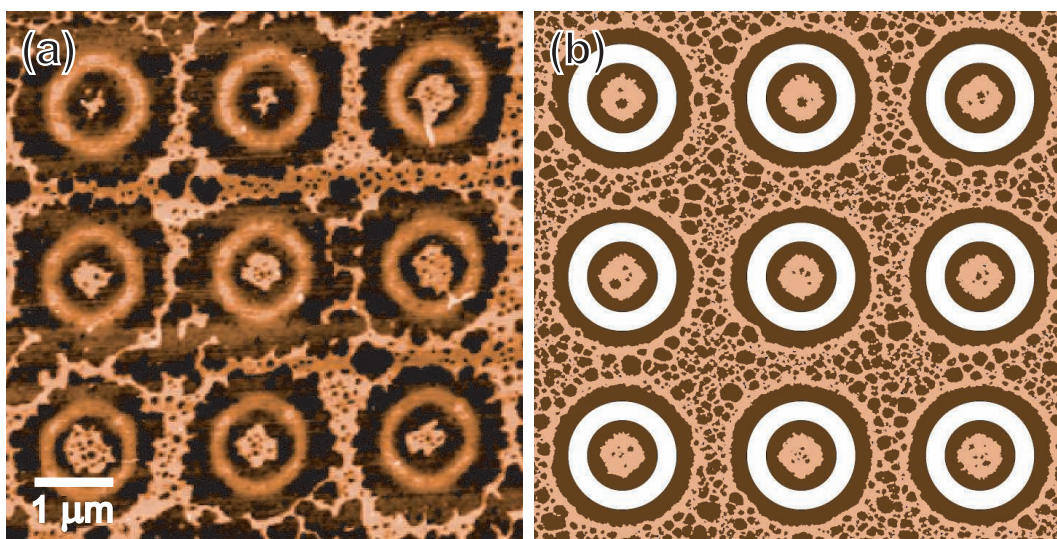


Figure 5.14: (a) An AFM image showing the effect of $1\mu\text{m}$ diameter rings of oxide on nanoparticle pattern formation (M. O. Blunt), and (b) a simulation in which sections of solvent and particles have been removed (indicated in white) to approximate the effect of dewetting from the oxide regions before the realm of the simulation.

in an experimental regime that is much closer to equilibrium conditions. The oxide square in Fig. 5.15a has more than twice the RMS roughness of the surrounding hydrogen passivated surface. When a nanoparticle solution is allowed to evaporate from this surface over a period of hours rather than seconds, the significantly decreased mobility of the particles on the rougher areas becomes apparent. If a small polytetrafluoroethene (PTFE) ring is placed on the substrate [96], the liquid can be contained in a concave meniscus, which allows the solvent to evaporate over a period of about two hours. This slow evaporation mode proceeds by a gradual radial “retreat” of the solvent. Particles that are otherwise quite mobile tend to accumulate on the roughened areas as the solvent retreats over them. Unable to escape, they build up to form a near complete single layer that is confined quite accurately within the boundary of

the oxide (Fig. 5.15b). Moreover, we find that a triangular “box” with boundaries just a few tens of nanometres thick has a similar effect. A close-packed monolayer is formed as particles enter the container from solution, only to find themselves unable to surmount the walls and follow the solvent as the thinning edge withdraws.

5.3 The fingering instability

A region of the simulation parameter space not yet discussed is that where a fingering instability is observed. If the mobility ratio (MR) is reduced in the thermal nucleation regime, “fingers” begin to appear perpendicular to the retreating solvent fronts. These are a result of local fluctuations in particle density, which lead to accumulations of particles that are unable to retreat with the solvent. Behind these accumulations, particles remain largely stationary as the solvent flows past them, forming finger-like structures. As mentioned earlier, these bear a striking resemblance to fingering in a viscous fluid [94]. Decreasing the particle mobility in this two-dimensional system can be considered akin to increasing the effective viscosity of the fluid.

Fig. 5.16 shows the effect of changing the value of MR. When MR is high enough, the particles are able to move with the solvent fronts as they retreat, leaving smoothly rounded cells. At slightly lower values, the cells become more angular, as the particles pack slightly closer together. As the mobility is lowered further still, small fingers begin to appear, reaching into the cells. Eventually, the branching is so significant it becomes difficult to discern the original nucleation sites, and the structure is more dendritic in appearance than

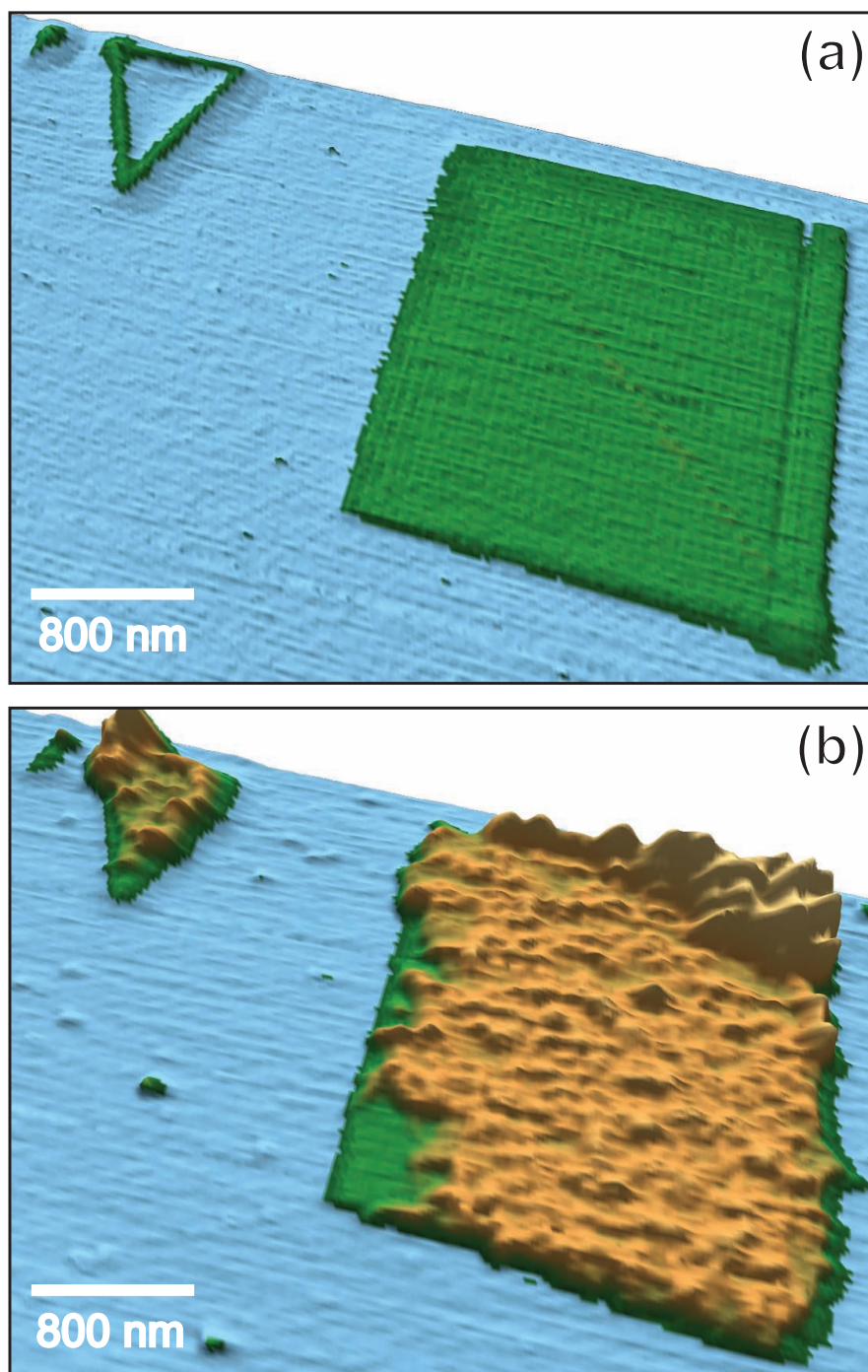


Figure 5.15: (a) A three-dimensional rendering of an AFM image of raised oxide areas on a hydrogen-passivated silicon surface (C. P. Martin), and (b) the same areas covered with trapped nanoparticles after slow (close to equilibrium) evaporation of a gold nanoparticle solution (E. Pauliac-Vaujour).

it is cellular. The experimental structures shown in Fig. 2.12 may therefore be a result of low particle mobility. It should be noted, however, that 2.12b also displays a non-fingered cellular structure on a smaller length scale, indicating it may have been formed by two distinct processes occurring at different film thicknesses. The fingering instability is a region of the parameter space that is currently under investigation by our collaborators in Dresden [127].

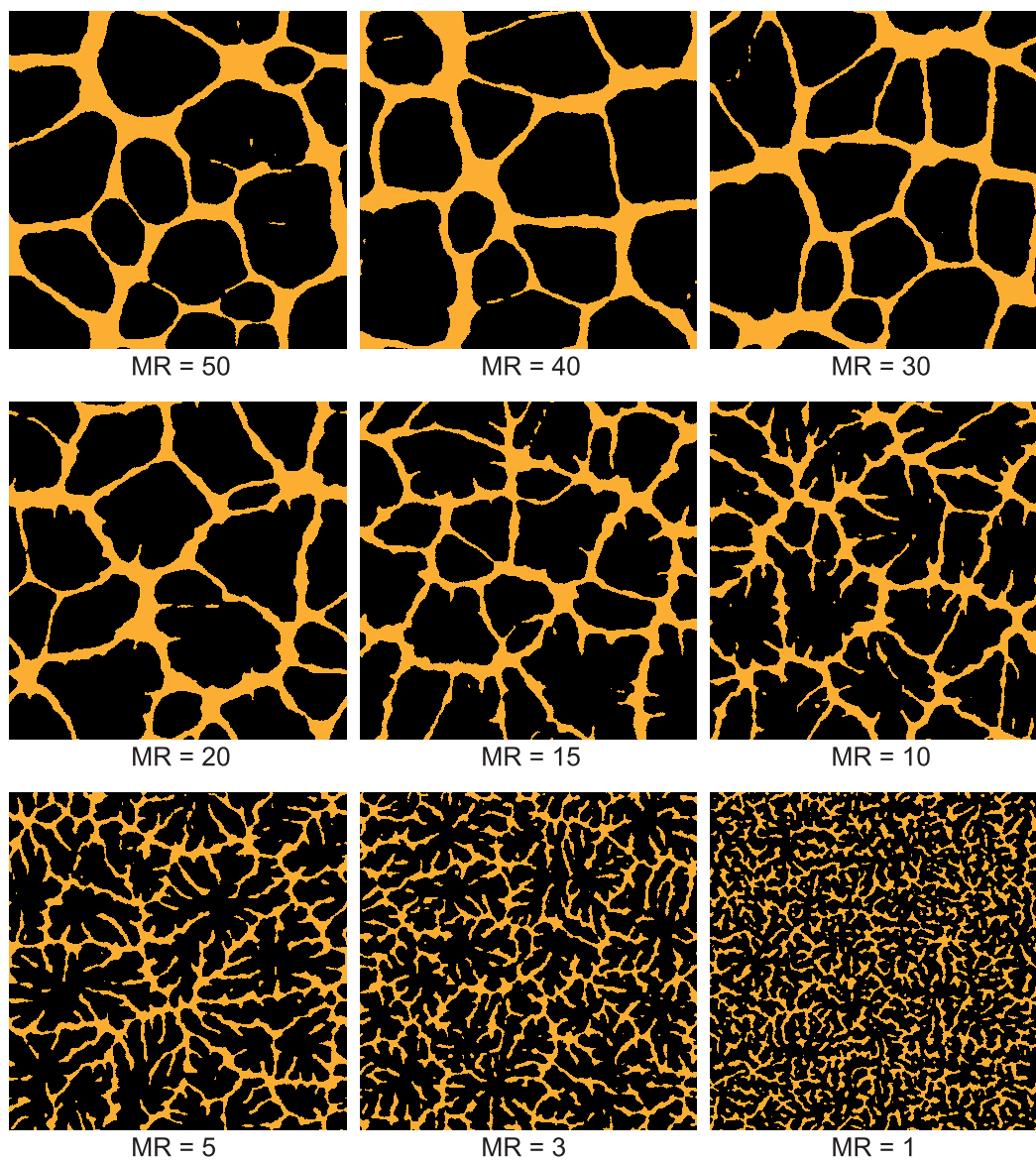


Figure 5.16: The effect of the mobility ratio (MR) on the development of fingers in a simulated cellular structure. In each case the interaction parameters are the same as in Figs. 5.4 and 5.5, with $kT=0.50$, and a particle coverage of 20%.

5.4 Conclusions

The ability to control the organisation and pattern forming properties of nanoparticles using the dynamics of solvent dewetting and evaporation is an important development on the road to self-organised nanoparticle devices. The absence of the requirement for particle functionalisation allows this technique to be employed with a wide range of different particle types and thus different physical, chemical, and electronic properties. The approach described thus opens up a rich new parameter space in directing the assembly of nanoparticle arrays.

Chapter 6

Scaling and Evolution of Nanoparticle Structures

“...theres nothing like millions of years of really frustrating trial and error to give a species moral fibre and, in some cases, backbone.”

Terry Pratchett (1948–)

Recent experiments carried out in our group have shown that under some conditions, dynamic scaling behaviour in nanocrystal networks can be induced by interaction with an AFM probe [2]. This chapter presents the results of a study of simulated scaling behaviour in simulations based on the model of Rabani et al. [1]. The final section of this chapter will discuss the use of a genetic algorithm approach to obtain a target structure in a simulation. [128].

6.1 Coarsening

Coarsening, or *dynamic scaling*, is a process during which a system maintains its morphology, but has a distinct and progressive increase in the length scale of its structure. This can be observed in a soap foam as smaller bubbles coalesce over time to form larger bubbles [129], or in the increasing size of droplets in a mixture of oil and water that has been shaken vigorously [130]. This process is often driven by a reduction in surface energy as a result of decreasing interface area. Coarsening is characterised by a power law such that $L(t) \propto t^\gamma$, where $L(t)$ is the length scale of the system at time t , and γ is known as the *scaling exponent*. The value of the scaling exponent can give an indication as to the coarsening mechanism.

Ostwald ripening is a phenomenon by which large clusters are able to grow at the expense of smaller clusters by a net transfer of monomers from smaller to larger islands (e.g. in epitaxial growth [131]). In Ostwald ripening in two dimensions, if the rate limiting step is the detachment/attachment of monomers, a scaling exponent of $\frac{1}{2}$ is obtained [132]. Alternatively, if the rate limiting step is the diffusion of the monomers across the surface, a scaling exponent of $\frac{1}{3}$ is obtained. A scaling exponent of $\frac{1}{4}$ is consistent with a cluster diffusion and coalescence process [133, 134], whereby cluster growth occurs solely by coalescence of wandering clusters. It should be noted, however, that the value of the scaling exponent may be insufficient to distinguish between different growth mechanisms, as a number of different processes can exhibit the same exponent. For this reason, it is useful to also consider the distribution of the island sizes, which will have a signature shape that is indicative of the mechanism involved.

6.1.1 Mechanically-induced coarsening

The recent experiments carried out by M. O. Blunt et al. in our research group [2] demonstrated that a system of nanoparticles on a surface can be driven to coarsen by interaction with an AFM probe. Scaling exponents were obtained for two different experimental morphologies by following the position of the peak in the radially-averaged 2DFFT. Fig. 6.1 shows four AFM images taken from a scaling labyrinthine structure.

An interesting result of this work is that two distinct scaling exponents were obtained depending on the morphology of the nanoparticle structures involved. For interconnected labyrinthine structures, an exponent of $\frac{1}{4}$ was consistently obtained. For systems of isolated islands, however, the exponent was consistently found to be $\frac{1}{2}$. This suggests that different mechanisms could be involved in the evolution of the two structures. Examination of my simulation results has allowed a clearer understanding of these phenomena.

6.1.2 Rabani et al. simulations

Rabani et al. observed coarsening in isolated islands of nanoparticles in their simulations, and found a scaling exponent of $\frac{1}{4}$ by calculating the mean size of islands as a function of time [1]. As discussed earlier, an exponent of $\frac{1}{4}$ is consistent with cluster growth occurring solely by diffusion and coalescence. However, this exponent is at odds with the results of our experiments, which indicate an exponent of $\frac{1}{2}$ in this regime, consistent with detachment-limited Ostwald ripening. To confirm the results of Rabani et al., further simulations were carried out.

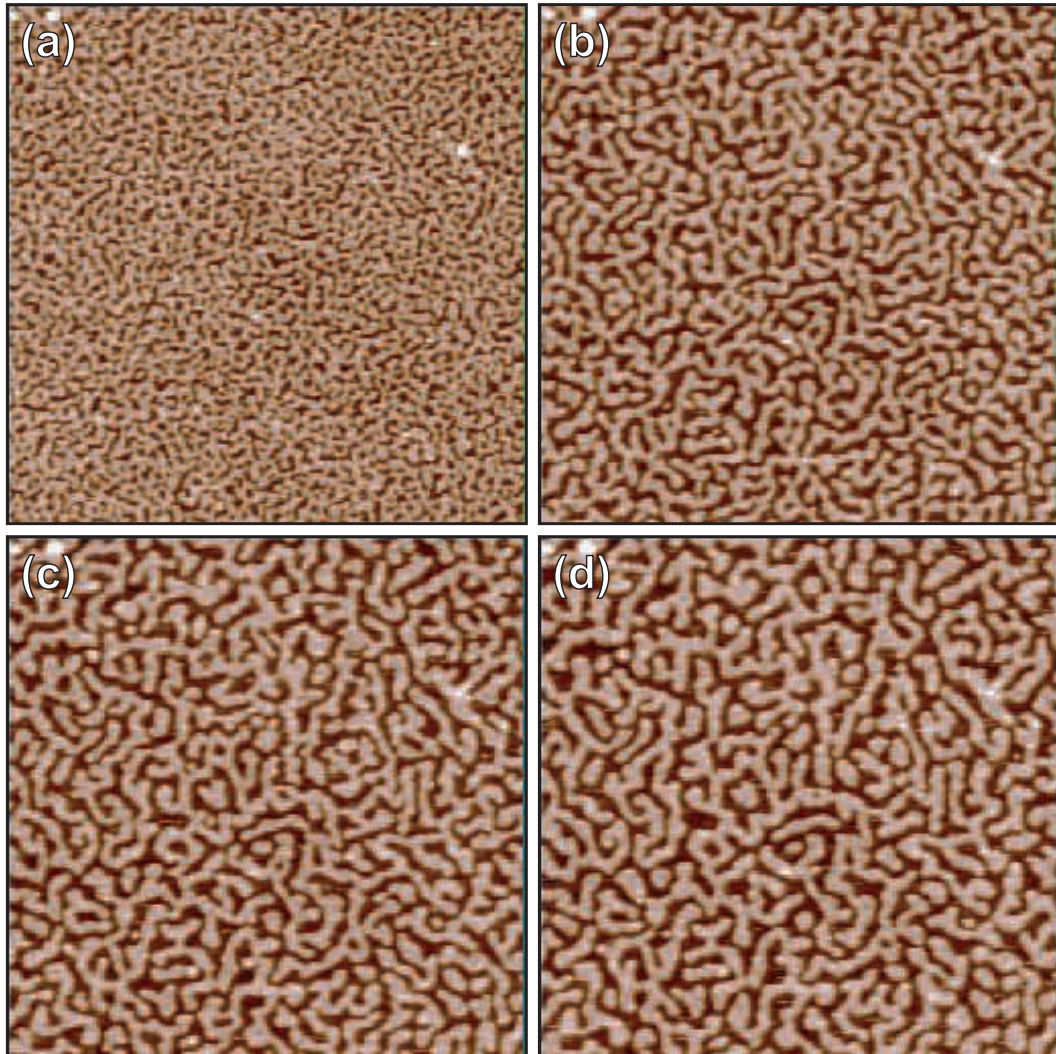


Figure 6.1: Coerced coarsening evolution of an interconnected nanoparticle assembly (M. O. Blunt, from [2]). All images are $1\mu\text{m} \times 1\mu\text{m}$. Images are taken from evenly spaced points throughout the experimental run, (a) 1st scan, (b) 15th scan, (c) 30th scan, and (d) 45th scan. The fractional area coverage of nanoparticles remains constant at approximately 0.55ML throughout the experimental run.

Isolated islands

In the early stages of evolution, a coarsening system will go through a transient regime while it asymptotically approaches a constant exponent. When obtaining a scaling exponent, it is therefore important to ensure that the system has reached this asymptotic limit, and the exponent is truly representative of the scaling behaviour. A thorough analysis of simulated isolated island systems using the University's high performance computing (HPC) grid has found the exponent of $\frac{1}{4}$ to be extremely consistent. Measuring the mean size of islands over a period of 200,000 MC steps (far beyond the common range of simulation time previously discussed) for a range of values of nanoparticle-nanoparticle interaction ($0.25\epsilon_l < \epsilon_n < 4\epsilon_l$, with $\epsilon_l = 2$ and $k_B T = 1$), has been able to produce no exponent that is conclusively and significantly above 0.27. Fig. 6.2 shows a summary of these results. A similar result was obtained from following the evolution of the peak in the radially-averaged 2DFFT.

Labyrinthine structures

There was no discussion in [1] of coarsening in regimes of different morphology, such as in labyrinthine structures. By setting the temperature such that $k_B T = \epsilon_l/2$, with a particle coverage of 30%, we reach a region of the parameter space with rapid and homogeneous evaporation. Under these conditions, solvent evaporation occurs uniformly across the lattice, as opposed to the random nucleations that occur at lower temperatures. Fig. 6.3 shows three frames from such a simulation. After a relatively short time, the majority of the solvent has evaporated, leaving the pattern shown in 6.3a. Although there seems to be little solvent remaining, closer inspection reveals a thin ($\approx 1\text{nm}$)

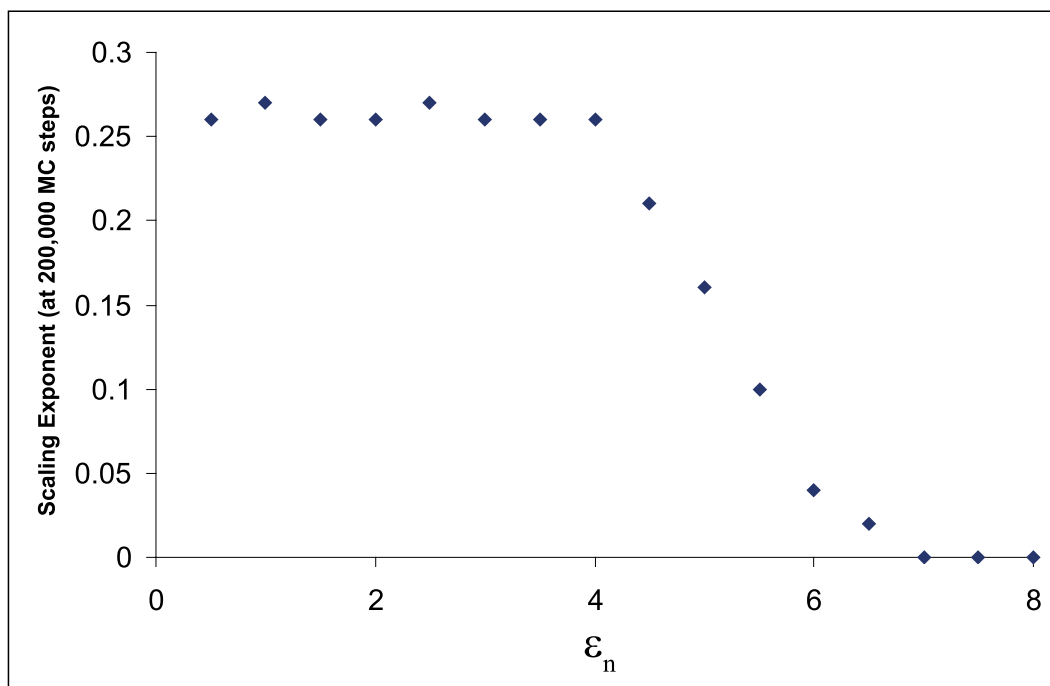


Figure 6.2: Scaling exponent after 200,000 MC steps of an isolated island system as a function of ϵ_n . Beyond the value of $\epsilon_n = 4\epsilon_l$, the particles become increasingly immobile, and the system will either take a very long time to begin stable scaling or simply remain completely immobile.

wetting layer that covers the domain boundaries. This gives the particles a certain freedom to move at the edges of each domain. Figs. 6.3b and 6.3c show frames at later times which have an increased length scale.

Measuring the mean cluster diameter in a system of islands is something that is easily carried out automatically, but this is not a measure that can be obtained from a labyrinthine system. The length scale of a bicontinuous structure can be obtained from the 2DFFT, but measuring the position of the peak in a radially-averaged 2DFFT is a process that is much more prone to noise than measuring the size of a number of islands. For this reason, a more robust technique was developed involving the use of Minkowski measures. This

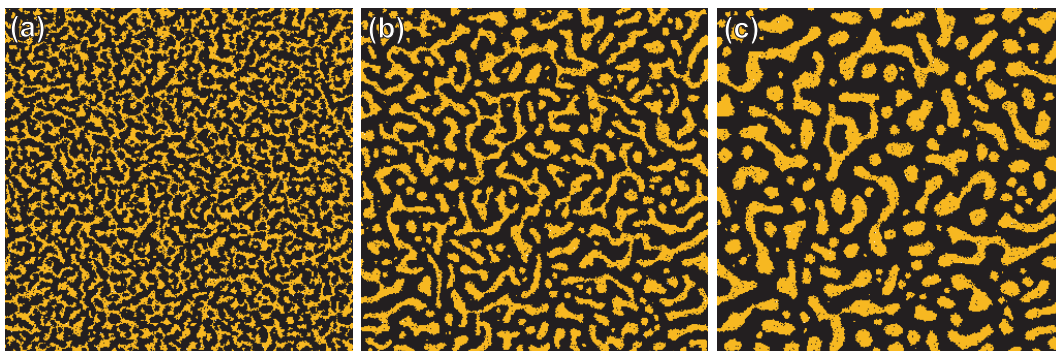


Figure 6.3: Three frames showing scaling of worm-like features after rapid evaporation in a 1008×1008 system with $k_B T = \epsilon_l/2$, $MR=30$, and a coverage of 30%, after (a) 39 MC steps, where the majority of the solvent has already evaporated leaving only a thin wetting layer around the domains, (b) after 299 MC steps showing a visibly increased length scale, and (c) after 999 MC steps where the length scale has clearly increased further.

has the added advantage of also following the evolution of the morphology of the structure.

The simplest measurement of scaling by Minkowski measures can be obtained from a plot of the Minkowski perimeter, (U), as a function of time. The actual characteristic length scale, L , can be extracted from the perimeter using the relation $L = A_{total}/U$, where A_{total} is the total area of the simulation. Fig. 6.4 shows a comparison of the two techniques— note the higher degree of noise in the Fourier graph. In a worm-like morphology, over 1000 MC steps, the exponent obtained from the Minkowski length-scale plot was found to be 0.26, with a very good fit to the later stages. The Euler characteristic (χ) was also found to scale at approximately this value, although it appeared to have a more extended transient region. This is perhaps not surprising, as this measure is more subject to noise than the measurement of the perimeter.

As the Minkowski measures provide a good description of morphology, they

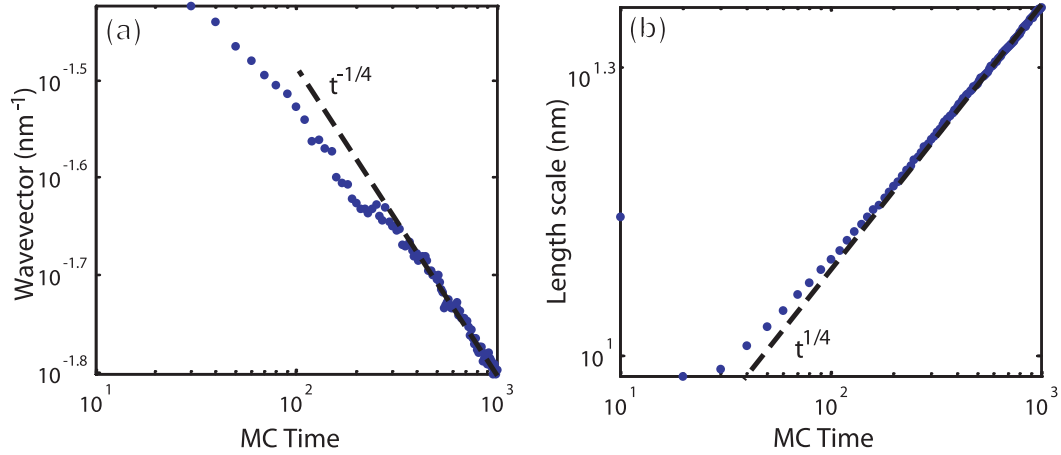


Figure 6.4: Numerical analysis of the scaling regime showing (a) the evolution of the peak in the 2D FFT, and (b) the evolution of the Minkowski length scale $L = A_{total}/U$ of the pattern. Both reveal an approach to an exponent of size $\frac{1}{4}$.

can also provide an indication of morphological stability in the simulations. A plot of $\chi(t)/U(t)$ for this system tends towards a constant value, indicating a constant ratio between the two numbers. Moreover, a plot of the differential of this ratio (i.e. $\frac{d(\chi(t)/U(t))}{dt}$) clearly and relatively rapidly tends to zero. This is a strong indication that not only is the length scale increasing with a $\frac{1}{4}$ exponent, but the overall nature of the structure is constant during the evolution—a characteristic feature of dynamic scaling. These two plots are shown in Fig. 6.5.

One exponent

An extensive search of the parameter space in the labyrinthine, worm-like, and isolated island areas has shown that $\frac{1}{4}$ is the only scaling exponent that is consistently obtained in the model of Rabani et al. In experimental labyrinthine structures, the scaling exponent is in agreement with these simulations. This could suggest a process of mass transport along the boundaries of the labyrinth.

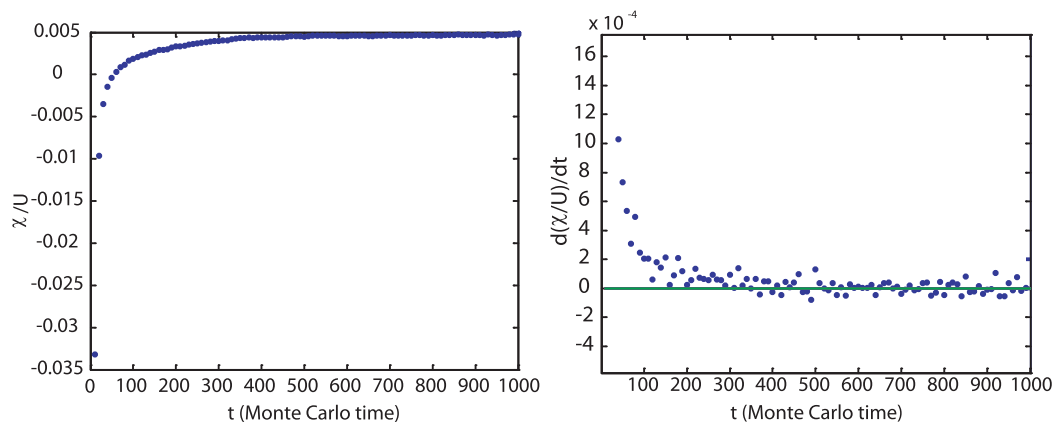


Figure 6.5: Two plots indicating morphological stability of a simulated labyrinthine system in the scaling regime. The right hand graph shows an even clustering around zero after 400 MC steps indicating the structure is stable.

Visually, this is the mechanism occurring in the scaling labyrinthine simulations: a thin wetting layer of solvent remains around the boundaries of the labyrinth, in which particles can diffuse and reduce the overall curvature (and therefore energy) of the structure. However, Huse et al. argue that Ostwald ripening can also give rise to an exponent of $\frac{1}{4}$ [135], so this is not necessarily the mechanism occurring in our experiments. Moreover, the exponent obtained in the experimental island morphologies does not match our simulations.

The exponent of $\frac{1}{2}$ obtained experimentally in the case of island morphologies has to result from a process not modelled by the Rabani et al. simulations. One of the mechanisms proposed for this evolution is that particles could be picked-up by the AFM probe and dropped elsewhere during scanning. This could lead to a situation similar to evaporation- and condensation-mediated Ostwald ripening. For this reason, I wrote a modified version of the Rabani et al. model in an attempt to replicate this process, and to try to obtain the

same exponent. To this end, the section of the code involved in performing the random walks of particles was removed, and replaced with an exchange of single particles with the tip.

There were a number of limitations associated with this modified Rabani et al. model, not least the existence of solvent during coarsening, which may or may not be present in experiments. The only exponents that could be conclusively obtained in this way were $\frac{1}{3}$ and $\frac{1}{4}$. The former was obtained when particles were allowed to be picked up and replaced in completely different regions of the substrate, and is the exponent expected for diffusion-limited Ostwald ripening. The latter occurred when particles were only allowed to be dropped within a few “scan lines” of being picked up, in an attempt to mimic the raster effect of the tip. Neither of these exponents matches the island morphology experimental exponent of $\frac{1}{2}$.

Island size distributions

Analysis of the distribution of island sizes was able to reveal the actual coarsening mechanism involved. Fig. 6.6 shows the theoretical island size distributions expected from the two main processes of Ostwald ripening [132, 136]. The filled circles are the data from the experimental island system. Although these data do not match either of the plots, the theoretical Ostwald ripening island size distributions are derived from a mean-field theory approximation, which assumes that there is a low volume fraction and the islands are widely separated. In the experimental system, this approximation is not valid as the volume fraction is significant. Conti et al. proposed that when the islands are closer together, a secondary process of binary coalescence will provide a sig-

nificant contribution to the shape of the island size distribution [137]. The fit to the experimental data shown in Fig. 6.6 is based on the solution of Conti et al., and appears to be an extremely good match.

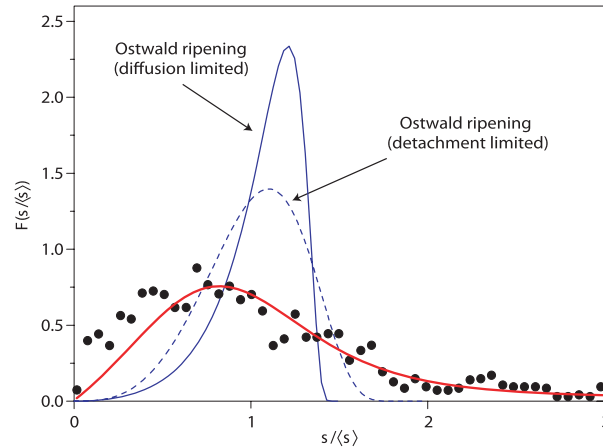


Figure 6.6: The island size distributions expected for the two main modes of Ostwald ripening (blue curves) and the distribution of island sizes in our mechanically-driven coarsening experiments (filled black circles). The solid red line is a fit to these data using the approximate form proposed by Conti et al. [137], which takes account of binary coalescence events (M. O. Blunt & P. Moriarty, from [2]).

6.2 Genetic algorithms

When all possible variables are taken into account, the parameter space of the Rabani et al. simulations is very large (and larger still with the inclusion of the dynamic chemical potential described in Chapter Five). To accurately replicate a particular experimental morphology requires a slow process of trial and error, the results of which are not necessarily always quite perfect. The ability to simulate a particular morphology that has been observed experimentally is a significant aid to understanding the process that generated that morphology. In collaboration with the School of Computer Science and Information Technology, a solution to this problem has been developed using a *genetic algorithm* (GA) [128]. The principle is simple: a target morphology is provided, and a population of phenotypes (morphologies) is generated from random genotypes (sets of parameters). The similarity of each phenotype to the target is measured, and the genes are re-combined and mutated to produce a second generation of phenotypes. The process continues until, for example, a desired level of “fitness” is reached. A section of pseudocode describing this procedure is shown in Fig. 6.7.

To enable the use of a GA with nanoparticle simulations, a *fitness function* must be defined so that it is possible to numerically compare a simulated structure to the target morphology. Chapter Four discussed the use of Minkowski measures as a tool for image comparison. Together, the three Minkowski measures can provide an accurate description of the morphology of a nanoparticle structure. A computationally inexpensive yet robust fitness function therefore can be defined using the root mean squared error (RMSE) between the target

```
while (stopping condition not fulfilled)
  parents = select parents from population
  with a defined probability
  'mate' the parents to form (usually) two children
  else
  children = parents
  with a defined probability
  mutate children
  insert children into population
  evaluate and cull population
```

Figure 6.7: Pseudocode representing the GA evolution method (P. Siepmann).

Minkowski values and those derived from the evolved patterns. The actual fitness function used is the reciprocal of the RMSE value.

To test this fitness function, and the effectiveness of the GA, a four experimental morphologies—deemed to be representative of a wide range of structures—were selected as targets for evolution. For each target image, the GA was run for 100 generations using a population of 20 individuals, and in each case the simulation was allowed to run for 1000 MC steps. This type of system is well-suited to execution on the University’s HPC facility, as it can easily be distributed over 20 nodes: one for each individual. This dramatically decreases the time required for execution of the GA. Fig. 6.8 shows results that are representative of the output from the GA. Fig. 6.9 shows how the evolution progressed in each case with plots of the fitness function over the generations.

It is clear that the GA has managed to produce structures that are visually very similar to the target structures, even using a relatively small population of individuals. A good result was obtained in each of the ten runs performed for each target, despite the often large standard deviations. Even for the least fit individuals, the visual correspondence is good. This indicates that the chosen

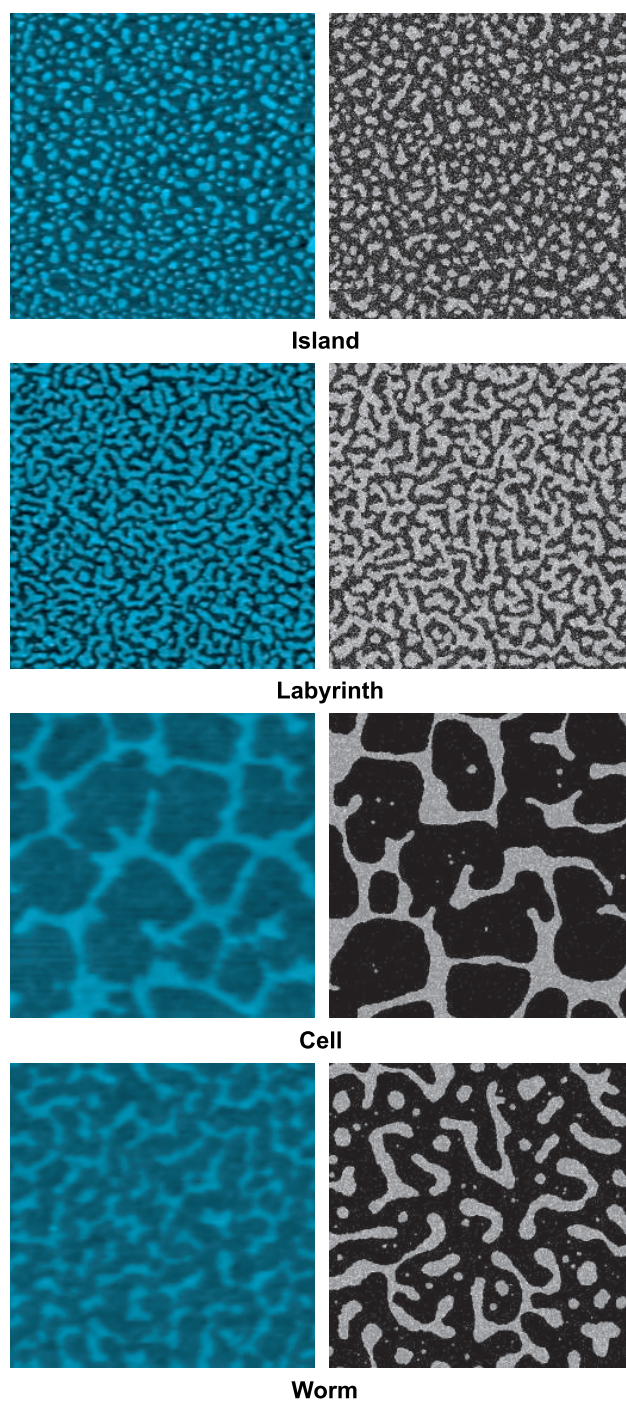
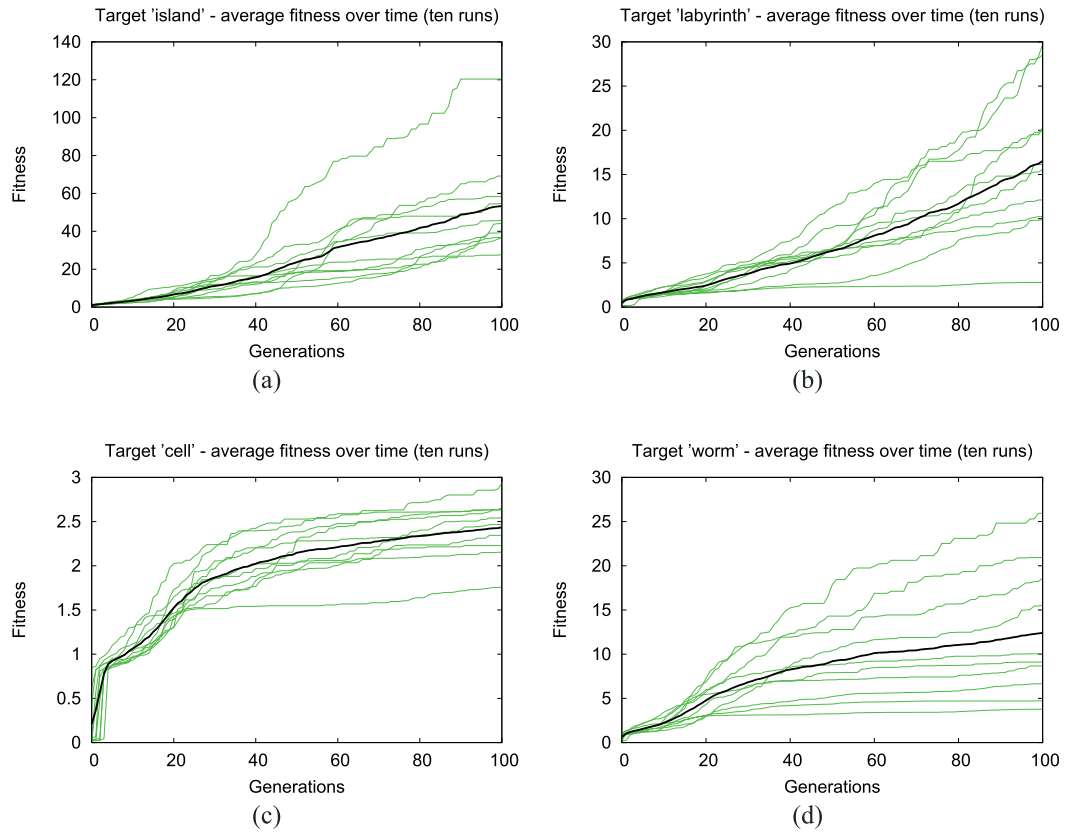


Figure 6.8: Evolved patterns using Minkowski measure RMSE fitness function, with experimental AFM target images in the left column, and the resulting simulated output from the GA in the right column (from [128]).



Target	Average fitness	Best fitness	Worst fitness	Fitness deviation
Island	111.9305	460.6708	36.07952	126.0549
Labyrinth	36.51094	84.49821	2.851095	27.09551
Cell	2.742406	3.632334	1.934135	0.427782
Worm	20.88366	50.97714	3.824032	17.15378

Figure 6.9: Population dynamics of the genetic algorithm (from [128]). Each experimental image was used as a target in ten independent runs of the GA. Panels (a)-(d) show the average population fitness as a function of time (“generations”) of each run as well as the average evolution (dark line). The table shows, for each experimental target, details of the fitness achieved by the winning individual in each of the ten runs.

fitness function is actually better at discerning a good match than the human brain— a device which is often prone to seeing a correspondence where none exists.

6.3 Conclusions

The Rabani et al. model is not able to reproduce the behaviour seen in mechanically induced coarsening of nanoparticle networks, even with the described modification. Although the scaling exponent matches for labyrinthine structures, the lack of correspondence for island morphologies, combined with the analysis of the island size distributions suggests both morphologies probably scale by means of Ostwald ripening, and individual particles are moved by the tip. In labyrinthine structures, coarsening proceeds by the transfer of monomers along domain boundaries [138], and in island structures the process involved is detachment limited Ostwald ripening, with the island size distribution modified by the coalescence of adjacent structures [137].

Development of a GA to evolve the Rabani et al. simulations towards a target morphology has presented a way to very accurately simulate an arbitrary experimental target morphology. The use of GAs could prove invaluable in evaluating new experimental results in the future. A possible next step, albeit a somewhat challenging one, is to attach an experimental nanoparticle system to a GA in order to evolve a physical structure to a desired morphology.

Chapter 7

Conclusions

“I may not have gone where I intended to go, but I think I have ended up where I needed to be.”

Douglas Adams (1952-2001)

7.1 Summary of findings

The work in this thesis has focused largely on pattern formation in nanoparticle arrays spin-cast from solution in organic solvents. Despite the apparent simplicity of the system, the range of nanoscale structures that are produced in this way is extremely diverse. Correspondingly, the mechanisms involved are many and varied. In this work, significant light has been shed on the processes that occur in the last few nanoseconds of evaporation.

Chapter Two discussed non-equilibrium pattern formation in the context of commonly encountered systems, highlighting the ubiquity of many of the

structures that are observed in nanoparticle systems. In particular, examples of cellular structures were given on a range of length scales spanning many orders of magnitude. The importance of the mathematical and geometric constraints that lead to the formation of cellular structures was emphasised. The behaviour of thin films of liquid on surfaces is central to the pattern formation mechanisms in this work, and the physics of such systems was discussed in detail in this chapter.

Monte Carlo simulation has formed a large fraction of the work carried out for this thesis, and simulations based on the model of Rabani et al. [1] are able to reproduce many of the structures that are seen in experiments. However, a significant fraction of the patterns that have been observed experimentally could not be replicated by these simulations. For this reason, a number of modifications were made to the model, with a large degree of success.

Morphological image analysis techniques were very successfully employed as both an aid to understanding pattern formation mechanisms, and to compare different structures. These techniques have improved scientific understanding of pattern formation not only in our colloidal nanoparticle system [110], but also in other dewetting-based systems [109].

Scanning probe lithography has been shown to be a technique that can alter the morphology of nanoparticle structures in an extremely well-defined region. In conjunction with my simulations, these experiments have demonstrated the important role that the surface chemistry plays in pattern formation processes. My modified simulations are able to reproduce the effects of local surface modification extremely well, indicating that we now have a very good understanding of the phenomena involved.

The large parameter space of the simulations can be automatically explored through the use of a genetic algorithm coupled to morphological image analysis routines. This will become increasingly important in future versions of the simulations, as the modifications to the Rabani et al. model have dramatically widened the parameter space by introducing several new degrees of freedom.

7.2 Further work

The parameter space of the modified simulations has not yet been fully explored, and there is much scope for further experimentation, particularly with different forms of chemical potential function; the parametric regions explored in Chapter Five represent a relatively thin slice of the parameter space. For example, reducing the mobility of the particles in the regime producing two sizes of cellular network may enable reproduction of the structure in Fig. 2.12b. However, if coupled to a genetic algorithm, such parameter space explorations may require more sophisticated fitness functions to discern features on multiple length scales.

With or without modifications, the Rabani et al. simulations are not able to reproduce the mechanically-induced scaling behaviour that is observed experimentally. For this reason, it may be worthwhile to write a new simulation based on our understanding of this process. This could help to confirm and clarify the conclusions reached in [2].

Although the difficulty of real-space observation of pattern formation processes has been consistently stated throughout this work, some inroads have been made in this direction. In an evaporation regime closer to equilibrium,

contrast-enhanced microscopy has allowed direct observation of retreating solvent fronts, and the formation of fingered structures [96]. Furthermore, high-speed camera technology could enable at least a macroscopic inspection of the spin-casting process. If the frame capture rate were to be synchronised with the rotation of the spinning stage (e.g. at 4000 frames per second), it would be possible to see how the solvent behaves in the early to intermediate stages of drying. However, a time resolution of 0.25ms is significantly coarser than would be required to observe the final stage of evaporation.

The level of control presented by the directed dewetting technique presents a significant step on the road to self-organised nanoparticle devices [116]. Nanoparticle structures produced by spin-casting have been shown to exhibit interesting electrical properties [139]. Future experimental work could therefore explore the possibility of the creation of a simple electronic device based on self-organised nanoparticle structures.

Bibliography

- [1] Eran Rabani, David R. Reichman, Phillip L. Geissler, and Louis E. Brus. Drying-mediated self-assembly of nanoparticles. *Nature*, 426:271–274, 2003.
- [2] M. O. Blunt, C. P. Martin, M. Ahola-Tuomi, E. Pauliac-Vaujour, P. Sharp, P. Nativo, M. Brust, and P. J. Moriarty. Coerced mechanical coarsening of nanoparticle assemblies. *Nature Nanotech.*, 2:167, 2007.
- [3] K. Eric Drexler. *Engines of Creation*. Anchor Books, New York, 1986.
- [4] Arthur C. Clarke. *Fountains of Paradise*. Victor Gollancz, London, 1979.
- [5] T.A. Fulton and G.J. Dolan. Observation of single-electron charging effects in small tunnel junctions. *Phys. Rev. Lett.*, 59:109–112, 1987.
- [6] R. Wetzal and D. V. Goeddel. Synthesis of polypeptides by recombinant DNA methods. *Peptides*, 5:1–64, 1983.
- [7] Richard A. L. Jones. *Soft Machines: Nanotechnology and Life*. Oxford University Press, New York, 2004.
- [8] *Nanoscience and nanotechnologies: opportunities and uncertainties*. The Royal Society & The Royal Academy of Engineering, London, 2004.

- [9] Erwin W. Müller. Study of atomic structure of metal surfaces in the field ion microscope. *J. Appl. Phys.*, 28:1–6, 1957.
- [10] D. M. Eigler and E. K. Schweizer. Positioning single atoms with a scanning tunnelling microscope. *Nature*, 344:524–526, 1990.
- [11] Richard P. Feynman. There’s plenty of room at the bottom. *Engineering and Science*, 23:22–36, 1960.
- [12] C. Toumey. Apostolic succession. *Eng. Sci.*, 68:16–23, 2005.
- [13] G. Binnig, H. Rohrer, Ch. Gerber, and E. Weibel. Tunneling through a controllable vacuum gap. *Appl. Phys. Lett.*, 40:178–180, 1982.
- [14] G. Binnig, H. Rohrer, Ch. Gerber, and E. Weibel. Surface studies by scanning tunneling microscopy. *Phys. Rev. Lett.*, 49:57–61, 1982.
- [15] Nadrian C. Seeman. DNA NANOTECHNOLOGY: Novel DNA constructions. *Annu. Rev. Biophys. Biomol. Struct.*, 27:225–248, 1998.
- [16] Kinneret Keren, Rotem S. Berman, Evgeny Buchstab, Uri Sivan, and Erez Braun. DNA-templated carbon nanotube field-effect transistor. *Science*, 302:1380–1382, 2003.
- [17] Richard Jones. *Self-assembly vs self-organisation – can you tell the difference?* Soft Machines Blog (<http://www.softmachines.org/wordpress/>), 15 November 2005.
- [18] H. Bénard. Les tourbillons cellulaires dans une nappe liquide. *Rev. Gén. Sci. Pure Appl.*, 11:1261–1271, 1900.

- [19] M. C. Cross and P. C. Hohenberg. Pattern formation outside of equilibrium. *Rev. Mod. Phys.*, 69:851–1112, 1993.
- [20] Alan W. Turing. The chemical basis of morphogenesis. *Philos. Trans. R. Soc. Lond., B, Biol. Sci.*, 237:37–72, 1952.
- [21] Philip Ball. *The Self-made Tapestry*. Oxford University Press, New York, 1999.
- [22] Fabio Raimondi, Günther G. Scherer, Rüdiger Kütz, and Alexander Wokaun. Nanoparticles in energy technology: Examples from electrochemistry and catalysis. *Angew. Chem. Int. Ed.*, 44:2190–2209, 2005.
- [23] A. Jaroenworarluck, W. Sunsaneeyametha, N. Kosachan, and R. Stevens. Characteristics of silica-coated TiO₂ and its UV absorption for sunscreen cosmetic applications. *Surf. Interface Anal.*, 38:473–477, 2006.
- [24] M. J. Bloemer, J. W. Haus, and P. R. Ashley. Degenerate four-wave mixing in colloidal gold as a function of particle size. *J. Opt. Soc. Am. B*, 7:790–795, 1990.
- [25] Günter Schmid. Large clusters and colloids. metals in the embryonic state. *Chem. Rev.*, 92:1709–1727, 1992.
- [26] Marie-Christine Daniel and Didier Astruc. Gold nanoparticles: Assembly, supramolecular chemistry, quantum-size-related properties, and applications toward biology, catalysis, and nanotechnology. *Chem. Rev.*, 104:293–346, 2004.

- [27] Mathias Brust, Merryl Walker, Donald Bethell, David J. Schiffrin, and Robin Whyman. Synthesis of thiol-derivatised gold nanoparticles in a two-phase liquid-liquid system. *J. Chem. Soc., Chem. Commun.*, pages 801–802, 1994.
- [28] D. Weaire and N. Rivier. Soap, cells and statistics: Random patterns in two dimensions. *Contemp. Phys.*, 25:59–99, 1984.
- [29] Volker Springel, Simon D. M. White, Adrian Jenkins, Carlos S. Frenk, Naoki Yoshida, Liang Gao, Julio Navarro, Robert Thacker, Darren Croton, John Helly, John A. Peacock, Shaun Cole, Peter Thomas, Hugh Couchman, August Evrard, Joerg Colberg, and Frazer Pearce. Simulations of the formation, evolution and clustering of galaxies and quasars. *Nature*, 435:629–636, 2005.
- [30] V. de Lapparent, M. J. Geller, and J.P. Huchra. A slice of the universe. *Astrophys. J. Lett.*, 302:L1–L6, 1986.
- [31] Denis Weaire and Stefan Hutzler. *The Physics of Foams*. Oxford University Press, New York, 1999.
- [32] Gudrun Schliecker. Structure and dynamics of cellular systems. *Adv. Phys.*, 51:1319–1378, 2002.
- [33] Homer. *Iliad*, ca. 800 BC.
- [34] Daniel W. Fong, Thomas C. Kane, and David C. Culver. Vestigialization and loss of nonfunctional characters. *Annu. Rev. Ecol. Syst.*, 26:249–268, 1995.

- [35] James D. Murray. How the leopard gets its spots. *Sci. Am.*, 258:80–87, 1988.
- [36] John W. Cahn. Phase separation by spinodal decomposition in isotropic systems. *J. Chem. Phys.*, 42:93–99, 1964.
- [37] Jacob N. Israelachvili. *Intermolecular and Surface Forces*. Academic Press, second edition, 1992.
- [38] B. V. Derjaguin and N. V. Churaev. Structural component of the disjoining pressure of thin layers of liquids. *J. Colloid Interface Sci.*, 49:249–255, 1974.
- [39] R. Seemann, S. Herminghaus, and K. Jacobs. Dewetting patterns and molecular forces: A reconciliation. *Phys. Rev. Lett.*, 86:5534–5537, 2000.
- [40] R. Seemann, S. Herminghaus, and K. Jacobs. Gaining control of pattern formation of dewetting liquid films. *J. Phys.: Condens. Matter*, 13:4925–4938, 2001.
- [41] Hyun I. Kim, C. Mathew Mate, Kelly A. Hannibal, and Scott S. Perry. How disjoining pressure drives the dewetting of a polymer film on a silicon surface. *Phys. Rev. Lett.*, 82:3496–3499, 1999.
- [42] E. F. Hare and Zisman W. A. Autophobic liquids and the properties of their adsorbed films. *J. Phys. Chem.*, 59:335–340, 1955.
- [43] Mark Geoghegan and Georg Krausch. Wetting at polymer surfaces and interfaces. *Prog. Polym. Sci.*, 28:261–302, 2003.

- [44] Günter Reiter. Dewetting of thin polymer films. *Phys. Rev. Lett.*, 68:75–78, 1992.
- [45] Ashutosh Sharma and Günter Reiter. Instability of thin polymer films on coated substrates: Rupture, dewetting, and drop formation. *J. Colloid Interface Sci.*, 178:383–399, 1996.
- [46] Ralf Seemann, Stephan Herminghaus, Chiara Neto, Stefan Schlagowski, Daniel Podzimek, Renate Konrad, HubertMantz, and Karin Jacobs. Dynamics and structure formation in thin polymer melt films. *J. Phys.: Condens. Matter*, 17:S267–S290, 2005.
- [47] Karin Jacobs and Stephan Herminghaus. Thin liquid polymer films rupture via defects. *Langmuir*, 14:965–969, 1998.
- [48] A. Vrij. Possible mechanism for the spontaneous rupture of thin, free liquid films. *Discuss. Faraday Soc.*, 42:23–33, 1966.
- [49] A. Vrij and J. Th. G. Overbeek. Rupture of thin liquid films due to spontaneous fluctuations in thickness. *J. Am. Chem. Soc.*, 90:3074–3078, 1968.
- [50] Günter Reiter. Unstable thin polymer films: Rupture and dewetting processes. *Langmuir*, 9:1344–1351, 1993.
- [51] Günter Reiter, Philippe Auroy, and Loïc Auvray. Instabilities of thin polymer films on layers of chemically identical grafted molecules. *Macromol.*, 29:2150–2157, 1996.

- [52] R. Xie, A. Karim, J. F. Douglas, C. C. Han, and R. A. Weiss. Spinodal dewetting of thin polymer films. *Phys. Rev. Lett.*, 81:1251–1254, 1998.
- [53] C. Bollinne, S. Cuenot, B. Nysten, and A. M. Jonas. Spinodal-like dewetting of thermodynamically-stable thin polymer films. *Eur. Phys. J. E*, 12:389–396, 2003.
- [54] C. Redon, F. Brochard-Wyart, and F. Rondelez. Dynamics of dewetting. *Phys. Rev. Lett.*, 66:715–718, 1991.
- [55] Günter Reiter, Ashutosh Sharma, Alain Casoli, Marie-Odile David, Rajesh Khanna, and Philippe Auroy. Thin film instability induced by long-range forces. *Langmuir*, 15:2551–2558, 1999.
- [56] Anthony M. Higgins and Richard A. L. Jones. Anisotropic spinodal dewetting as a route to self-assembly of patterned surfaces. *Nature*, 404:476–478, 2000.
- [57] Jean-Loup Masson and Peter F. Green. Pattern formation in thin polymer films: A new morphology. *Mat. Res. Soc. Symp.*, 629:FF1.2.1–FF1.2.5, 2000.
- [58] M. Mertig, U. Thiele, J. Bradt, G. Leibiger, W. Pompe, and H. Wendorf. Scanning force microscopy and geometric analysis of two-dimensional collagen network formation. *Surf. & Interf. Anal.*, 25:514–521, 1997.
- [59] M. Mertig, U. Thiele, J. Bradt, D. Klemm, and W. Pompe. Dewetting of thin collagenous precursor films. *Appl. Phys. A*, 66:S565–S568, 1998.

- [60] Uwe Thiele, Michael Mertig, and Wolfgang Pompe. Dewetting of an evaporating thin liquid film: Heterogeneous nucleation and surface instability. *Phys. Rev. Lett.*, 80:2869–2872, 1998.
- [61] J. Bischof, D. Scherer, S. Herminghaus, , and P. Leiderer. Dewetting modes of thin metallic films: Nucleation of holes and spinodal dewetting. *Phys. Rev. Lett.*, 77:1536–1539, 1996.
- [62] Ashutosh Sharma and Ruhi Verma. Pattern formation and dewetting in thin films of liquids showing complete macroscale wetting: From pancakes to swiss cheese. *Langmuir*, 20:10337–10345, 2004.
- [63] O. K. C. Tsui, Y.J. Wang, H. Zhao, and B. Du. Some views about the controversial dewetting morphology of polystyrene films. *Eur. Phys. J. E*, 12:417–425, 2003.
- [64] Peter Müller-Buschbaum. Dewetting and pattern formation in thin polymer films as investigated in real and reciprocal space. *J. Phys.: Condens. Matter*, 15:R1549–R1582, 2003.
- [65] Michael Giersig and Paul Mulvaney. Preparation of ordered colloid monolayers by electrophoretic deposition. *Langmuir*, 9:3408–3413, 1993.
- [66] Chad A. Mirkin, Robert L. Letsinger, Robert C. Mucic, and James J. Storhoff. A DNA-based method for rationally assembling nanoparticles into macroscopic materials. *Nature*, 382:607–609, 1996.
- [67] C. J. Kiely, J. Fink, M. Brust, D. Bethell, and D. J. Schiffrin. Spontaneous ordering of bimodal ensembles of nanoscopic gold clusters. *Nature*, 396:444–446, 1998.

- [68] Ronald P. Andres, Jeffery D. Bielefeld, Jason I. Henderson, David B. Janes, Venkat R. Kolagunta, Clifford P. Kubiak, William J. Mahoney, , and Richard G. Osifchin. Self-assembly of a two-dimensional superlattice of molecularly linked metal clusters. *Science*, 2:1690–1693, 1996.
- [69] P. J. Durston, J. Schmidt, R. E. Palmera, and J. P. Wilcoxon. Scanning tunneling microscopy of ordered coated cluster layers on graphite. *Appl. Phys. Lett.*, 71:2940–2942, 1997.
- [70] M. P. Pileni. Nanosized particles made in colloidal assemblies. *Langmuir*, 13:3266–3276, 1997.
- [71] Brian A. Korgel and Donald Fitzmaurice. Condensation of ordered nanocrystal thin films. *Phys. Rev. Lett.*, 80:3351–3354, 1998.
- [72] X. M. Lin, H. M. Jaeger, C. M. Sorensen, and K. J. Klabunde. Formation of long-range-ordered nanocrystal superlattices on silicon nitride substrates. *J. Phys. Chem. B*, 105:3353–3357, 2001.
- [73] Suresh Narayanan, Jin Wang, and Xiao-Min Lin. Dynamical self-assembly of nanocrystal superlattices during colloidal droplet evaporation by in situ small angle x-ray scattering. *Phys. Rev. Lett.*, 93:135503, 2004.
- [74] Terry P. Bigioni, Xiao-Min Lin, Toan T. Nguyen, Eric I. Corwin, Thomas A. Witten, and Heinrich M. Jaeger. Kinetically driven self assembly of highly ordered nanoparticle monolayers. *Nature Mat.*, 5:265–270, 2006.

- [75] L. Motte, F. Billoudet, E. Lacaze, J. Douin, and M. P. Pileni. Self-organization into 2D and 3D superlattices of nanosized particles differing by their size. *J. Phys. Chem. B*, 101:138–144, 1997.
- [76] James R. Heath, Charles M. Knobler, and Daniel V. Leff. Pressure/temperature phase diagrams and superlattices of organically functionalized metal nanocrystal monolayers: The influence of particle size, size distribution, and surface passivant. *J. Phys. Chem. B*, 101:189–197, 1997.
- [77] Manfred T. Reetz, Martin Winter, and Bernd Tesche. Self-assembly of tetraalkylammonium salt-stabilized giant palladium clusters on surfaces. *Chem. Commun.*, pages 147–148, 1997.
- [78] John Fink, Christopher J. Kiely, Donald Bethell, and David J. Schiffrin. Self-organization of nanosized gold particles. *Chem. Mater.*, 10:922–926, 1998.
- [79] Jiaying Huang, Franklin Kim, Andrea R. Tao, Stephen Connor, and Peidong Yang. Spontaneous formation of nanoparticle stripe patterns through dewetting. *Nature Mat.*, 4:896–900, 2004.
- [80] C. P. Collier, T. Vossmeier, and J. R. Heath. Nanocrystal superlattices. *Annu. Rev. Phys. Chem.*, 49:371–404, 1998.
- [81] Robert L. Whetten, Marat N. Shafigullin, Joseph T. Khoury, T. Gregory Schaaff, Igor Vezmar, Marcos M. Alcaez, and Angus Wilkinson. Crystal structures of molecular gold nanocrystal arrays. *Acc. Chem. Res.*, 32:397–406, 1999.

- [82] C. B. Murray, C. R. Kagan, and M. G. Bawendi. Synthesis and characterization of monodisperse nanocrystals and close-packed nanocrystal assemblies. *Annu. Rev. Mater. Sci.*, 30:545–610, 2000.
- [83] C. B. Murray, Shouheng Sun, W. Gaschler, H. Doyle, T. A. Betley, and C. R. Kagan. Colloidal synthesis of nanocrystals and nanocrystal superlattices. *IBM J. Res. & Dev.*, 45:47–56, 2001.
- [84] Mathias Brust and Christopher J. Kiely. Some recent advances in nanostructure preparation from gold and silver particles: a short topical review. *Coll. & Surf. A: Physicochem. Eng. Aspects*, 202:175–186, 2002.
- [85] Guanglu Ge and Louis Brus. Evidence for spinodal phase separation in two-dimensional nanocrystal self-assembly. *J. Phys. Chem. B*, 104:9573–9575, 2000.
- [86] M. Maillard, L. Motte, A. T. Ngo, and M. P. Pileni. Rings and hexagons made of nanocrystals: A marangoni effect. *J. Phys. Chem. B*, 104:11871–11877, 2000.
- [87] Mathieu Maillard, Laurence Motte, and Marie-Paule Pileni. Rings and hexagons made of nanocrystals. *Adv. Mater*, 13:200–204, 2001.
- [88] Cynthia Stowell and Brian A. Korgel. Self-assembled honeycomb networks of gold nanocrystals. *Nano Lett.*, 1:595–600, 2001.
- [89] Philip Moriarty, Michael D. R. Taylor, and Mathias Brust. Nanostructured cellular networks. *Phys. Rev. Lett.*, 89:248303, 2002.

- [90] J. N. OShea, M. A. Phillips, M. D. R. Taylor, P. Moriarty, M. Brust, and V. R. Dhanak. Colloidal particle foams: Templates for au nanowire networks? *Appl. Phys. Lett.*, 81:5039–5041, 2002.
- [91] Hajime Tanaka. Viscoelastic phase separation. *J. Phys.: Condens. Matter*, 12:R207–R264, 2000.
- [92] Jing Tang, Guanglu Ge, and Louis E. Brus. Gas-liquid-solid phase transition model for two-dimensional nanocrystal self-assembly on graphite. *J. Phys. Chem. B*, 106:5653–5658, 2002.
- [93] T. A. Witten, Jr. and L. M. Sander. Diffusion-limited aggregation, a kinetic critical phenomenon. *Phys. Rev. Lett.*, 47:1400–1403, 1981.
- [94] H. S. Hele-Shaw. The flow of water. *Nature*, 58:33–36, 1898.
- [95] Guy Yosef and Eran Rabani. Self-assembly of nanoparticles into rings: A lattice-gas model. *J. Phys. Chem. B*, 110:20965–20972, 2006.
- [96] Emmanuelle Pauliac-Vaujour and Philip Moriarty. In preparation. 2007.
- [97] N. Metropolis. The beginning of the Monte Carlo method. *Los Alamos Science*, 15:125–130, 1987.
- [98] Nicholas Metropolis and S. Ulam. The Monte Carlo method. *J. Amer. Stat. Assoc.*, 44:335–341, 1949.
- [99] Ernst Ising. Beitrag zur theorie des ferromagnetismus. *Zeits f. Physik*, 31:253–258, 1925.

- [100] Lars Onsager. Crystal statistics. I. a two-dimensional model with an order-disorder transition. *Phys. Rev.*, 65:117–149, 1944.
- [101] Nicholas Metropolis, Arianna W. Rosenbluth, Marshall N. Rosenbluth, Augusta H. Teller, and Edward Teller. Equation of state calculations by fast computing machines. *J. Chem. Phys.*, 21:1087–1092, 1953.
- [102] Eran Rabani (private communication), 2004.
- [103] G. Binnig, C. F. Quate, and Ch. Gerber. Atomic force microscope. *Phys. Rev. Lett.*, 56:930–933, 1986.
- [104] J. A. Dagata. Device fabrication by scanned probe oxidation. *Science*, 8:1625–1626, 1995.
- [105] Ph. Avouris, R. Martel, T. Hertel, and R. Sandstrom. AFM-tip-induced and current-induced local oxidation of silicon and metals. *Appl. Phys. A*, 66:S659–S667, 1998.
- [106] Phaedon Avouris, Tobias Hertel, and Richard Martel. Atomic force microscope tip-induced local oxidation of silicon: kinetics, mechanism, and nanofabrication. *Appl. Phys. Lett.*, 71:285–287, 1997.
- [107] Didier Stiévenard and Bernard Legrand. Silicon surface nano-oxidation using scanning probe microscopy. *Prog. Surf. Sci.*, 81:112–140, 2006.
- [108] Paul C. Jukes, Sasha Y. Heriot, James S. Sharp, and Richard A. L. Jones. Time-resolved light scattering studies of phase separation in thin film semiconducting polymer blends during spin-coating. *Macromol.*, 38:2030–2032, 2005.

- [109] F. Frehill, K. H. G. Schulte, C. P. Martin, L. Wang, S. Patel, J. A. Purton, J. G. Vos, and P. Moriarty. Iron wheels on silicon: Wetting behavior and electronic structure of adsorbed organostannoxane clusters. *Langmuir*, 20:6421–6429, 2004.
- [110] Christopher P. Martin, Matthew O. Blunt, and Philip Moriarty. Nanoparticle networks on silicon: Self-organized or disorganized? *Nano Lett.*, 4:2389–2392, 2003.
- [111] Susmit Kumar and Stewart K. Kurtz. Properties of a two-dimensional poisson-voronoi tessellation: A monte-carlo study. *Mater. Charact.*, 31:55–68, 1993.
- [112] K. Michielsen and H. De Raedt. Integral-geometry morphological image analysis. *Phys. Rep.*, 347:461–538, 2001.
- [113] W. Pratt. *Digital Image Processing*. John Wiley and Sons, second edition, 1991.
- [114] V. Chandrasekhar, S. Nagendran, S. Bansal, M. A. Kozec, and D. R. Powell. An iron wheel on a tin drum: A novel assembly of a hexaferrocene unit on a tinoxxygen cluster. *Angew. Chem., Int. Ed.*, 39:1833–1835, 2000.
- [115] Martin Brinkmann, Sabine Graff, and Fabio Biscarini. Mechanism of nonrandom pattern formation of polar-conjugated molecules in a partial wetting regime. *Phys. Rev. B*, 66:165430, 2002.
- [116] Christopher P. Martin, Matthew O. Blunt, Emmanuelle Pauliac-Vaujour, Ioan Vancea, Uwe Thiele, and Philip Moriarty. Controlling pattern for-

- mation in nanoparticle assemblies via directed solvent dewetting. *Phys. Rev. Lett.*, 99:116103, 2007.
- [117] Claudia G. Sztrum, Oded Hod, and Eran Rabani. Self-assembly of nanoparticles in three-dimensions: Formation of stalagmites. *J. Phys. Chem. B*, 109:6741–6747, 2005.
- [118] P. G. de Gennes. Wetting statics and dynamics. *Rev. Mod. Phys.*, 57:827–863, 1985.
- [119] U. Thiele. Open questions and promising new fields in dewetting. *Eur. Phys. J. E*, 12:409–416, 2003.
- [120] A. J. Parker, P. A. Childs, R. E. Palmer, and M. Brust. Interaction of passivated clusters in solution with micro-patterned surfaces: guided flow versus defect pinning. *Nanotechnology*, 12:6–10, 2001.
- [121] G. W. C. Kaye and T. H. Laby. *Tables of Physical and Chemical Constants*. Longman, Harlow, sixteenth edition, 1995.
- [122] R. Seemann, S. Herminghaus, and K. Jacobs. Dewetting patterns and molecular forces: A reconciliation. *Phys. Rev. Lett.*, 86:5534–5537, 2001.
- [123] José Bico, Uwe Thiele, and David Quéré. Wetting of textured surfaces. *Colloids and Surfaces A: Physicochem. Eng. Aspects*, 206:41–46, 2002.
- [124] Rahul Konnur, Kajari Kargupta, and Ashutosh Sharma. Instability and morphology of thin liquid films on chemically heterogeneous substrates. *Phys. Rev. Lett.*, 84:931–934, 2000.

- [125] Lutz Brusch, Heiko Kühne, Uwe Thiele, and Markus Bär. Dewetting of thin films on heterogeneous substrates: Pinning versus coarsening. *Phys. Rev. E*, 66:011602, 2002.
- [126] Kajari Kargupta and Ashutosh Sharma. Mesopatterning of thin liquid films by templating on chemically patterned complex substrates. *Langmuir*, 19:5153–5163, 2003.
- [127] Uwe Thiele and Ioan Vancea. Unpublished.
- [128] Peter Siepmann, Christopher P. Martin, Ioan Vancea, Philip Moriarty, and Natalio Krasnogor. A genetic algorithm approach to probing the evolution of self-organised nanostructured systems. *Nano Lett.*, 7:1985–1990, 2007.
- [129] James A. Glazier and Denis Weaire. The kinetics of cellular patterns. *J. Phys.: Condens. Matter*, 4:1867–1894, 1991.
- [130] H. Furukawa. A dynamic scaling assumption for phase separation. *Adv. Phys.*, 34:703–750, 1985.
- [131] M. Zinke-Allmang. Phase separation on solid surfaces: nucleation, coarsening and coalescence kinetics. *Thin Sol. Films*, 346:1–68, 1999.
- [132] V. V. Slyozov I. M. Lifshitz. The kinetics of precipitation from supersaturated solid solutions. *J. Phys. Chem. Solids*, 19:35–50, 1961.
- [133] M. von Smoluchowski. Drei Vorträge über Diffusion, Brownsche Bewegung und Koagulation von Kolloidteilchen. *Physik. Z.*, 17:557–585, 1916.

- [134] Alan Lo and Rex T. Skodje. Kinetic and Monte Carlo models of thin film coarsening: Cross over from diffusion-coalescence to Ostwald growth modes. *J. Chem. Phys.*, 112:1966–1974, 2000.
- [135] David A. Huse. Corrections to late-stage behavior in spinodal decomposition: Lifshitz-Slyozov scaling and Monte Carlo simulations. *Phys. Rev. B*, 34:7845–7850, 1986.
- [136] C. Wagner. Theorie der Alterung von Niederschlägen durch Umlösen (Ostwald-Reifung). *Z. Elektrochem.*, 65:581–591, 1961.
- [137] Massimo Conti, Baruch Meerson, Avner Peleg, , and Pavel V. Sasorov. Phase ordering with a global conservation law: Ostwald ripening and coalescence. *Phys. Rev. E*, 65:046117, 2002.
- [138] H.-J. Ernst, F. Fabre, and J. Lapujoulade. Observation of dynamical scaling in “spinodal decomposition” in two dimensions. *Phys. Rev. Lett.*, 69:458–461, 1992.
- [139] Matthew O. Blunt, Milovan Šuvakov, Fabio Pulizzi, Christopher P. Martin, Emmanuelle Pauliac-Vaujour, Andrew Stannard, Andrew W. Rushforth, Bosiljka Tadić, , and Philip Moriarty. Charge transport in cellular nanoparticle networks: Meandering through nanoscale mazes. *Nano Lett.*, 7:855–860, 2007.

List of Figures

1.1	The (somewhat erroneous) public perception of nanotechnology and its potential. By Coneyl Jay, winner of the 2002 “Visions of Science Award” from <i>The Daily Telegraph</i>	3
1.2	The beginnings of nanoscience and naotechnology: (a) a field ion microscope image (FIM) of a rhenium surface, showing individual atoms [9], and (b) 35 xenon atoms precisely manipulated with a scanning tunnelling microscope (STM) tip to spell out “IBM” [10].	5
1.3	The two base pairs of DNA, showing dashed lines where the molecules “recognise” each other by hydrogen bonding (left), and a section of assembled DNA (right).	7
1.4	Two examples of self-organisation, showing (a) viscous oil in a Petri dish heated from below displaying Bénard convection (from Cross & Hohenberg [19]), and (b) the pattern on the hide of a Rothschild’s giraffe in Kenya (courtesy of E. Pauliac-Vaujour).	9

1.5	A liquid drop on a solid surface, showing how the contact angle, θ_{slg} , arises from the balance of the interfacial energies (or surface tensions) between the solid and liquid (γ_{sl}), solid and gas (γ_{sg}), and the liquid and gas (γ_{lg}).	11
1.6	The schematic structure of a thiol-passivated gold nanoparticle.	13
2.1	Natural examples of cellular structures, showing (a) part of the columnar basalt structure known as the “Giant’s Causeway” in Antrim, Northern Ireland, with an accurate sketch of another region of the same (inset, from [28]), (b) cellular patterns of cracking in dry mud, (c) soap foam– a familiar manifestation of a three-dimensional cellular structure, and (d) a section from the “Millennium Simulation”, a supercomputer model of the formation of large-scale structure in the Universe, which is remarkably foam-like, and has long filaments of matter separated by large voids [29].	18
2.2	Two different morphologies (known as “Turing patterns”) in a simulated reaction-diffusion system, showing (a) spots, and (b) labyrinthine stripes.	23

2.3	An explanation of spinodal decomposition, showing (a) how the shape of the free energy curve can lead to demixing, and (b) a schematic phase diagram for such a mixture of two polymers. The coexistence curve separates the region where the mixture exists as a stable single phase. Between the spinodal line and the coexistence curve, the free energy can be lowered by separating into two phases. Below the spinodal line, the mixture is unstable with respect to infinitesimal fluctuations in composition, and will spontaneously separate.	24
2.4	The physics of dewetting, showing (a) three schematic interface potentials, and optical micrographs of the three modes of dewetting: (b) homogeneous thermal nucleation in the metastable regime, (c) spinodal dewetting in an unstable or metastable film, and (d) heterogeneous nucleation, also in an unstable or metastable film (from [40]).	27
2.5	Optical micrographs showing three stages of defect-nucleated (heterogeneous) dewetting in an 80 nm thick polystyrene film on hydrophobic silicon (from [46]) showing (a) nucleation of holes, followed by (b) their growth and coalescence into a cellular structure, and (c) droplets formed by the break-up of the cell walls due to the Rayleigh instability.	29

2.6	Transmission electron microscope (TEM) images of nanoparticle superlattices, showing (a) a monolayer of citrate-stabilised gold nanoparticles prepared on a carbon-coated copper grid (a “TEM grid”) by electrophoresis [65], (b) an aggregate of DNA-linked gold nanoparticles [66], and (c) an ordered bimodal array of 4.5 ± 0.8 and 7.8 ± 0.9 nm gold particles [67].	33
2.7	Gold nanocrystal monolayer from [74], showing (a) a TEM image of a region of the array with inset detail of array dimensions and a 2D Fourier transform of the same, and (b) an optical micrograph of a highly ordered particle monolayer on the surface of the solvent before drying. The extent of the monolayer can be visualised by the defect present in the lower right hand corner, and the cracking visible near the centre.	35
2.8	Atomic force microscope (AFM) images of CdSe particle structures on highly-oriented pyrolytic graphite (HOPG) with increasing surface coverage (from [85]), showing (a) a $5\mu\text{m}$ image of isolated clusters of particles formed during spin-casting from hexane solution, (b) a $5\mu\text{m}$ image of a broken labyrinthine structure formed during spin-casting from chloroform, and (c) a $10\mu\text{m}$ image of a cellular structure also formed during spin-casting from chloroform. Graphite terraces are visible in (c).	36
2.9	The formation of (a) polygonal networks and (b) rings from drop-deposited nanoparticle solutions by surface-tension driven convection (c).	37

2.10	Three dimensional projections of the three main morphologies observed in far from equilibrium nanoparticle arrays, showing (a) isolated island clusters of particles, (b) a “worm like” morphology, with isolated twisting ribbons of particles, (c) a labyrinth of particles, and (d) a cellular network.	39
2.11	AFM images of nanoparticle assemblies displaying multiple length-scale cellular networks (taken by M. O. Blunt), showing (a) two distinct sizes of cellular structure at a thickness of one particle layer, (b) an image similar to (a) except with the formation of a third network structure atop the boundaries of the larger network, and (c) an image similar to (a) except with the formation of smaller holes inside some cells of the small network.	40
2.12	Two patterns that are sometimes observed in nanoparticle systems: (a) fractal aggregates, reminiscent of diffusion limited aggregation [93], and (b) “viscous fingering” holes [94].	41
3.1	The equilibrium state of the Ising model (spin +1 is blue, -1 is white) calculated by a Metropolis algorithm at different temperatures showing the system (a) well above the critical temperature, with no overall magnetisation, (b) exactly at the critical temperature, with slowly fluctuating domains of each spin, and (c) below the critical temperature where one spin direction fills the whole lattice.	49

3.2	Schematic flow diagram illustrating how the Rabani model simulation proceeds.	54
3.3	Panel (a) shows a pictorial representation of the Rabani model simulation, showing liquid solvent in white, solvent vapour in black, and nanoparticles in orange. The particle in the bottom right is able to move up or down, but not to the left where the substrate is not completely wet. Panel (b) shows an illustration of the four-phase checkerboard pattern that is used in the examination of the solvent (see section 3.2.3).	55
3.4	Three frames from a 1000x1000 simulation in the thermal nucleation regime without the inclusion of next-nearest neighbour interactions. The vapour bubbles are clearly square even after only 101 MC steps (a). The square bias has continued up to 201 MC steps (b), and after 301 MC steps even the collision of two vapour bubbles still leaves reasonably linear sides (c).	56
3.5	Some sample morphologies obtained from simulations, showing (a) a 1008x1008 lattice with $k_B T = \epsilon_l/2$, $\epsilon_n = 2\epsilon_l$, $\epsilon_{nl} = 1.5\epsilon_l$, $\mu = -2.25\epsilon_l$, MR=30, and a coverage of 30% after 69 MC steps, (b) a 4008x4008 lattice with $k_B T = \epsilon_l/4$, MR=30, coverage 20% after 1003 MC steps, (c) a 3000x3000 lattice with $k_B T = \epsilon_l/2$, MR=50, coverage 35%, after 399 MC steps, and (d) a 1008x1008 lattice with $k_B T = \epsilon_l/4$, MR=10, coverage 20% after 1003 MC steps.	58
3.6	A scanning electron micrograph of an AFM cantilever, showing the tip in the bottom right.	60

3.7	The basic operation of an atomic force microscope (AFM) in contact mode.	61
3.8	A schematic of the lithographic AFM oxidation process.	64
4.1	(a) A typical Atomic Force Microscope (AFM) image of a cellular network obtained from spin-casting Au nanoclusters in toluene onto a Si substrate [89], and (b) the same network reduced to a Voronoi tessellation.	70
4.2	Decomposition of the pixels of a two-dimensional binary pattern (left) into squares, edges and vertices (right). For this example: number of squares $n_s = 8$, number of edges $n_e = 24$ and number of vertices $n_v = 16$ [112].	74
4.3	The decoration of germs (light grey) with grains (dark grey) that are discrete approximations to circles (left) and squares (right) [112].	75

4.4 (a) Tapping mode atomic force microscope (AFM) image ($8\mu\text{m}\times 8\mu\text{m}$) of a thin stannoxane film spin-cast from toluene onto a native-oxide-terminated Si(111) substrate. The film has a cellular morphology with a mean thickness of approximately 4nm. The dewetting holes in the film expose the underlying SiO_2/Si substrate. (b) A radial average of a two-dimensional Fourier transform of the image shown in (a), with the 2DFFT shown in the inset. Note the presence of a peak at a wavevector of $25\mu\text{m}^{-1}$, suggesting the presence of an inter-cell correlation length of the order $2\pi/25\mu\text{m}$ (i.e. 250nm). Note that the somewhat poor statistics associated with the radially averaged Fourier transform which arises from the relatively small scan area (and thus small number of cells) associated with this image. [109]. 77

4.5	<p>(a-c) Minkowski functionals (covered area, boundary length, and Euler characteristic respectively) for a Poisson distribution of points and a point set based on the coordinates of the dewetting cell centres for the image shown in Fig. 4.4 (solid lines and filled circles/solid lines, respectively). In each case, the functionals are plotted as a function of x, the normalized grain size. The inset to (a) depicts the difference between germs (the black pixels) and grains (grey pixels) centred on the germs. Note the strong deviation of each of the Minkowski functionals for the stannoxane-derived point system from the functionals for a Poisson-distributed set of points. (d-f) Difference between the stannoxane- and Poisson-derived result for each 2D Minkowski functional [109].</p>	78
4.6	<p>Simulated images from the homogeneous thermal nucleation regime, with $k_B T = \epsilon_l/4$, $\epsilon_n = 2\epsilon_l$, $\epsilon_{nl} = 1.5\epsilon_l$, $\mu = -2.25\epsilon_l$, MR=30, and a nanoparticle coverage of 20%, showing the early stages of pattern formation in a 4008x4008 pixel system after (a) 99 MC steps, with a distribution of nucleation sites that is clearly uncorrelated, (b) 199 MC steps, illustrating coalescence of neighbouring nucleation sites, and (c) 899 MC steps, the stable end result, which is best described as a cellular network. Pane (d) shows a radially averaged two-dimensional Fourier transform of (c), with a clear peak resulting from the ring visible in the inset.</p>	82

4.7 Statistical analysis showing (a) a Voronoi tessellation of figure 4.6c highlighting the cellular structure, and (b) a graph indicating the probability of a cell having a given number of sides in the tessellation. Panel (c) shows another simulation image, this time 3000x3000, $k_B T = \epsilon_l/3$, MR=50, and a coverage of 35%, and panel (d) is the image from Fig. 4.4a, shown alongside panel (c) for ease of comparison. The qualitative similarity between these two images is striking. 83

4.8 Minkowski functional grain growth analysis for the organos-tannoxane dewetting pattern (open circles) and the simulated nanoparticle image of Fig. 4.7c (triangles). Panels (a-c) show the plots of area, perimeter, and Euler characteristic respectively, with the expected behaviour for a Poisson distribution shown by the solid line. Panels (d-f) show the deviation from the Poisson lines in each case. It is clear that not only do both patterns have a strong deviation from the Poisson distribution, but they also follow each other quite closely. 84

5.1 A typical specular trace from the optospinometer, showing the distinctive oscillations resulting from constructive and destructive interference between light reflected from the substrate and light reflected from the toluene surface. 88

5.2 The thickness trace obtained from Fig. 5.1 (filled diamonds), with a sixth-order polynomial fit (solid line). 88

5.3 (a) An AFM image of a two-level cellular structure formed by spin-casting a solution of gold nanoparticles in toluene onto a silicon substrate, and (b) a radially-averaged two-dimensional fast Fourier transform of (a), with the original “binned” data shown as filled circles. The solid line is the same data after smoothing by a 10-point “LOWESS” method, which clarifies the bimodal nature of the distribution. 90

5.4 A representative broad phase diagram showing the structures that are produced at different temperatures and coverages after 1000 MC steps in a 1024×1024 solvent cell system with the parameters $\epsilon_l = 2$, $\epsilon_n = 2\epsilon_l$, $\epsilon_{nl} = 1.5\epsilon_l$, $\mu = -2.25\epsilon_l$, and MR=20. 92

5.5 A more detailed version of a small region of the phase diagram in Fig. 5.4 (but after 2000 MC steps), showing the range of temperatures and coverages over which the majority of common structures are produced. One edge of the useful parameter space is defined by parameter ranges where no evaporation occurs in a reasonable time scale (i.e. at low temperatures). 93

5.6 (a) An AFM image of a two-level cellular structure formed by spin-casting a solution of gold nanoparticles in toluene onto a silicon substrate (M. O. Blunt), (b) a simulated structure formed by linking the chemical potential (μ) to the solvent density (in the form $\mu(v) = \mu_0 + (0.1\mu_0 \times v^{0.7})$, where v is the fraction of solvent that has become vapour, and μ_0 is the value of μ at the beginning of the simulation), (c) an AFM image of gold nanoparticles spun onto silicon from solution in chloroform (M. O. Blunt), and (d) a simulated image with a much stronger coupling between μ and solvent coverage (in the form $\mu(v) = \mu_0 + (0.5\mu_0 \times v^{0.7})$) 95

5.7 (a) The AFM image from Fig. 5.6a with a Voronoi tessellation superimposed, (b) a plot of the frequency distributions of cells with a given number of sides for the tessellation in (a), having a variance of 1.3 ± 0.1 , and an entropy of 1.50 ± 0.06 , (c) a simulation image with a coupling between μ and solvent coverage with a superimposed Voronoi tessellation, and (d) a plot of the frequency distributions of cells with a given number of sides for the tessellation in (c), having a variance of 1.3 ± 0.1 , and an entropy of 1.48 ± 0.06 96

5.8 Square-grain Minkowski functional comparison of the structures in Fig. 5.6 (a) and (b), showing the experimental data as crosses, simulated data as open circles, and for the purposes of comparison, data from a single-length-scale network is shown as plus symbols, and the solid line represents the theoretical result for a purely random distribution. 97

5.9 Simulation results with dynamic μ , continued in Fig. 5.10. . . . 99

5.10 Continued from Fig. 5.9, the range of images produced when $\mu(v) = \mu_0 + (0.1\mu_0 \times v^A)$, where v is the fraction of solvent that has become vapour, and μ_0 is the value of μ at the beginning of the simulation. The last panel shows plots of these functional forms of $\mu(v)$. All images are 2048 lattice sites square, with all parameters (excluding μ) identical to those used to produce Fig. 3.5b. 100

5.11 Simulation results with dynamic μ , continued in Fig. 5.12. . . . 101

5.12 Continued from Fig. 5.11, the range of images produced when the gradient in μ is much steeper, such that $\mu(v) = \mu_0 + (0.5\mu_0 \times v^A)$, where v is the fraction of solvent that has become vapour, and μ_0 is the value of μ at the beginning of the simulation. Again, all images are 2048 lattice sites square, with all parameters (excluding μ) identical to those used to produce Fig. 3.5b. 102

5.13 (a) An AFM image of gold nanoparticles spun from solution in toluene onto a hydrogen-passivated silicon substrate with an AFM-patterned $4\mu\text{m} \times 4\mu\text{m}$ square of oxide in the centre (M. O. Blunt), and (b) the result of a simulation with $|\mu|$ 6% lower on the oxide area. 104

5.14 (a) An AFM image showing the effect of $1\mu\text{m}$ diameter rings of oxide on nanoparticle pattern formation (M. O. Blunt), and (b) a simulation in which sections of solvent and particles have been removed (indicated in white) to approximate the effect of dewetting from the oxide regions before the realm of the simulation. 108

5.15 (a) A three-dimensional rendering of an AFM image of raised oxide areas on a hydrogen-passivated silicon surface (C. P. Martin), and (b) the same areas covered with trapped nanoparticles after slow (close to equilibrium) evaporation of a gold nanoparticle solution (E. Pauliac-Vaujour). 110

5.16 The effect of the mobility ratio (MR) on the development of fingers in a simulated cellular structure. In each case the interaction parameters are the same as in Figs. 5.4 and 5.5, with $kT=0.50$, and a particle coverage of 20%. 112

6.1 Coerced coarsening evolution of an interconnected nanoparticle assembly (M. O. Blunt, from [2]). All images are $1\mu\text{m} \times 1\mu\text{m}$. Images are taken from evenly spaced points throughout the experimental run, (a) 1st scan, (b) 15th scan, (c) 30th scan, and (d) 45th scan. The fractional area coverage of nanoparticles remains constant at approximately 0.55ML throughout the experimental run. 117

6.2 Scaling exponent after 200,000 MC steps of an isolated island system as a function of ϵ_n . Beyond the value of $\epsilon_n = 4\epsilon_l$, the particles become increasingly immobile, and the system will either take a very long time to begin stable scaling or simply remain completely immobile. 119

6.3 Three frames showing scaling of worm-like features after rapid evaporation in a 1008×1008 system with $k_B T = \epsilon_l/2$, $\text{MR}=30$, and a coverage of 30%, after (a) 39 MC steps, where the majority of the solvent has already evaporated leaving only a thin wetting layer around the domains, (b) after 299 MC steps showing a visibly increased length scale, and (c) after 999 MC steps where the length scale has clearly increased further. 120

6.4 Numerical analysis of the scaling regime showing (a) the evolution of the peak in the 2D FFT, and (b) the evolution of the Minkowski length scale $L = A_{total}/U$ of the pattern. Both reveal an approach to an exponent of size $\frac{1}{4}$ 121

6.5 Two plots indicating morphological stability of a simulated labyrinthine system in the scaling regime. The right hand graph shows an even clustering around zero after 400 MC steps indicating the structure is stable. 122

6.6 The island size distributions expected for the two main modes of Ostwald ripening (blue curves) and the distribution of island sizes in our mechanically-driven coarsening experiments (filled black circles). The solid red line is a fit to these data using the approximate form proposed by Conti et al. [137], which takes account of binary coalescence events (M. O. Blunt & P. Moriarty, from [2]). 124

6.7 Pseudocode representing the GA evolution method (P. Siepmann). 126

6.8 Evolved patterns using Minkowski measure RMSE fitness function, with experimental AFM target images in the left column, and the resulting simulated output from the GA in the right column (from [128]). 127

6.9 Population dynamics of the genetic algorithm (from [128]). Each experimental image was used as a target in ten independent runs of the GA. Panels (a)-(d) show the average population fitness as a function of time (“generations”) of each run as well as the average evolution (dark line). The table shows, for each experimental target, details of the fitness achieved by the winning individual in each of the ten runs. 128